How do uncertainties in cloud microphysical parameterizations influence the cloud structure in an extratropical cyclone?

Master's Thesis in
Meteorology and Climate Physics
by

Vanessa K. M. Schneider

28.05.2025

INSTITUTE OF METEOROLOGY AND CLIMATE RESEARCH
KARLSRUHE INSTITUTE OF TECHNOLOGY (KIT)

Advisor:	Dr. Annika Oertel
Co-Advisor:	Prof. Dr. Corinna Hoose
Supervisor:	Miriam Simm

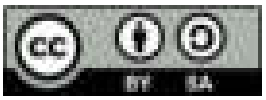

Abstract

Warm conveyor belts (WCBs) are responsible for most of the precipitation in the extratropical storm track region and also influence the large-scale midlatitude dynamics. Moreover, they serve as a major factor in shaping the cloud radiative effects across midlatitude regions. However, accurate model representation of WCBs is limited, for example, due to uncertainties in cloud microphysical parameterizations. This can lead to downstream error growth in numerical weather prediction and limited predictability. That is why this thesis investigates the influence of five uncertain model parameters on the cloud structure of a WCB case that occurred in the North Atlantic during the North Atlantic Waveguide and Downstream Impact Experiment (NAWDEX) campaign. For that, uncertain cloud microphysical processes, as well as environmental conditions relevant for WCB ascent, are systematically perturbed and a perturbed parameter ensemble (PPE) is built using the ICOsahedral Nonhydrostatic (ICON) modeling framework. Specifically, the uncertain model parameters are cloud condensation nucleus (CCN) concentration, ice nucleating particle (INP) concentration, capacitance (CAP) of ice and snow, sea surface temperature (SST), and maximum supersaturation with respect to liquid (SAT). The PPE simulations are evaluated by combining Eulerian and Lagrangian perspectives of the WCB cloud band. For further quantification of the relative importance of the perturbed parameters for the WCB cloud structure, variance decomposition is performed based on the output of random forest regression (RFR) surrogate models that are built for various target variables, such as mass and number concentrations of different hydrometeors. The results indicate that the liquid phase of the vertically extended WCB cloud is predominantly influenced by CCN concentrations, while the ice phase is primarily affected by CAP perturbations. More specifically, increased CCN concentrations systematically increase cloud water mass and number concentrations through enhanced CCN activation and coincident smaller mean cloud droplet radii. This goes along with a decrease in rain mass and number concentration due to a reduced conversion of cloud water to rain. Reducing CAP of ice and snow substantially increases graupel mass concentrations due to a larger depositional growth rate of graupel. Furthermore, graupel number concentrations increase through higher riming rates caused by higher ice and snow number concentrations. Additionally, lower CAP values reduce the net longwave radiation at the top of the atmosphere because the cloud top is shifted to lower temperatures. Although INPs markedly influence heterogeneous freezing rates, only a small overall impact is found on ice and snow number concentrations, which are more strongly influenced by homogeneous freezing dominated by CAP. Furthermore, SAT perturbations do not show major influences, and SSTs appear to slightly influence the net shortwave radiation at the top of the atmosphere. Variance decomposition further highlights the contributions of CCNs and CAP to the variance in mass and number concentrations of cloud water, rain, ice, snow, and graupel, as well as their effects on the radiation balance at the top of the atmosphere. The findings of this thesis underscore the importance of accurately representing cloud microphysical processes, in particular CCN concentrations and CAP, in numerical weather prediction models to improve precipitation forecasts as well as the characteristics of the large-scale WCB cloud band.

Zusammenfassung

Warm conveyor belts (WCBs) sind für den Großteil des Niederschlags in der außertropischen Sturmregion verantwortlich und beeinflussen die großskalige Dynamik der mittleren Breiten. Darüber hinaus stellen sie einen entscheidenden Faktor für die Ausprägung der Strahlungseffekte von Wolken in den mittleren Breiten dar. Allerdings ist die akkurate Darstellung von WCBs in Modellen beispielweise durch Unsicherheiten in den Parametrisierungen der Wolkenmikrophysik begrenzt. Das kann in der numerischen Wettervorhersage zu einer Fehlerfortpflanzung führen und die Vorhersagbarkeit einschränken. In dieser Thesis wird daher der Einfluss von fünf unsicherheitsbehafteten Modellparametern auf die Wolkenstruktur eines WCBs, der im Nordatlantik während der North Atlantic Waveguide and Downstream Impact Experiment (NAWDEX) Kampagne auftrat, untersucht. Dafür werden wolkenmikrophysikalische Prozesse, sowie Umweltbedingungen, die von Unsicherheiten behaftet und für den WCB-Aufstieg relevant sind, systematisch variiert und ein Ensemble von gestörten Parametern (PPE) mithilfe des ICOsahedral Nonhydrostatic (ICON) Modellsystems erstellt. Die betrachteten unsicheren Modellparameter sind die Konzentration von Wolkenkondensationskernen (CCNs), die Konzentration von Eiskeimen (INPs), die Kapazität (CAP) von Eis und Schnee, die Meeresoberflächentemperatur (SST) und die maximale Übersättigung in Bezug auf Flüssigwasser (SAT). Die PPE-Simulationen werden durch eine Kombination aus Eulerscher und Lagrangescher Betrachtungweise des WCB-Wolkenbandes ausgewertet. Zur weiteren Quantifizierung der relativen Bedeutung der gestörten Parameter für die WCB-Wolkenstruktur wird eine Varianzzerlegung durchgeführt. Diese basiert auf Random Forest Regressionsmodellen (RFR-Modelle), die zur Vorhersage verschiedener Zielgrößen, wie Massen- und Anzahlkonzentrationen unterschiedlicher Hydrometeore, verwendet werden. Die Ergebnisse zeigen, dass die Flüssigphase der vertikal ausgedehnten WCB-Wolke hauptsächlich durch die CCN-Konzentrationen beeinflusst wird, während die Eisphase in erster Linie von CAP-Störungen geprägt ist. Konkret führen erhöhte CCN-Konzentrationen systematisch zu höheren Massen- und Anzahlkonzentrationen von Wolkenwasser, bedingt durch verstärkte CCN-Aktivierung und kleinere mittlere Wolkentropfenradien. Dies geht einher mit einer Abnahme der Regenmassen- und -anzahlkonzentrationen, da weniger Wolkenwasser zu Regen umgewandelt wird. Eine Reduktion der CAP von Eis und Schnee erhöht die Graupelmassenkonzentration erheblich, da dadurch die Depositionswachstumsrate von Graupel zunimmt. Zudem steigen die Graupelanzahlkonzentrationen aufgrund höherer Raten der Anlagerung unterkühlter Wassertröpfchen an Eiskristallen, welche auf höhere Anzahlkonzentrationen von Eis und Schnee zurückzuführen sind. Niedrigere CAP-Werte verringern darüber hinaus die langwellige Nettostrahlung am oberen Rand der Atmosphäre, da die Wolkenobergrenze zu kälteren Höhenlagen verschoben wird. Obwohl INPs die heterogene Eisnukleation deutlich beeinflussen, zeigt sich insgesamt nur ein geringer Effekt auf die Anzahlkonzentrationen von Eis und Schnee. Dies liegt daran, dass diese stärker durch die homogene Eisbildung beeinflusst werden, welche wiederum hauptsächlich von CAP-Störungen dominiert wird. SAT-Störungen haben keinen signifikanten Einfluss, während für SST-Störungen ein geringer Einfluss auf die kurzwellige Nettostrahlung am oberen Rand der Atmosphäre zu beobachten ist. Die Varianzzerlegung verdeutlicht darüber hinaus die Beiträge von CCNs und CAP zur Varianz in den Massen- und Anzahlkonzentrationen von

Wolkenwasser, Regen, Eis, Schnee und Graupel, sowie deren Einfluss auf die Strahlungsbilanz am oberen Rand der Atmosphäre. Die Ergebnisse dieser Arbeit heben die Bedeutung einer präzisen Repräsentation wolkenmikrophysikalischer Prozesse, insbesondere der CCN-Konzentrationen und der Kapazität, in numerischen Wettervorhersagemodellen hervor, um sowohl Niederschlagsvorhersagen als auch die Darstellung des großskaligen WCB-Wolkenbands zu verbessern.

Preface

ChatGPT (https://www.chatgpt.com) was used for translations, spelling improvements, and stylistic improvements of figures. Spell and grammar checks were performed with Writeful (https://www.writefull.com/) and Grammarly (https://grammarly.com/).

The perturbed parameter ensemble data were produced in the subproject B8 of the Transregional Collaborative Research Center SFB/TRR 165 “Waves to Weather” (https://www.wavestoweather.de) and are presented in Oertel et al. (2025b). The warm conveyor belt trajectory data are publicly available in RADAR4KIT (https://dx.doi.org/10.35097/ecgs4f56mp3ymjmt; Oertel et al., 2025a).

Contents

1 Introduction

Warm conveyor belts (WCBs) influence the daily weather in mid-latitudes and are responsible for most of the total and extreme precipitation in that region (Pfahl et al., 2014). In fact, WCBs give rise to more than 70 % of the extreme precipitation events in the southeastern United States, Japan, eastern China, and parts of South America according to Pfahl et al. (2014). A WCB is a coherent moist airstream that ascends from the warm sector of an extratropical cyclone (ETC) while forming a long cloud shield (Eckhardt et al., 2004; Madonna et al., 2014). In addition, WCBs influence the radiation balance in the extratropics with their cloud band (Joos, 2019) and alter upper-tropospheric potential vorticity (PV) anomalies by latent heat release within the WCB, which impacts large-scale dynamics (Joos and Wernli, 2012; Madonna et al., 2014; Christ et al., 2025).

Recent studies have focused on PV modification and associated effects such as the amplification of downstream ridges (Grams et al., 2011), the intensification of the cyclone itself (Binder et al., 2016), or the microphysical processes in the cloud (Oertel et al., 2023). Moreover, several studies have investigated the impact of sea surface temperature (SST; Christ et al., 2025) and initial moisture (Schäfler and Harnisch, 2015; Berman and Torn, 2022) in the lower-tropospheric inflow region of WCBs on the WCB ascent and found implications for the large-scale atmospheric flow, i.e., potential downstream ridge amplification. Furthermore, Mazoyer et al. (2021) have studied the impact of two different microphysics schemes on a WCB and downstream ridge building, whereas Mazoyer et al. (2023) have investigated the influences of two different parameterizations of mixed phase cloud processes. The former study shows that upper-level dynamics strongly depend on the representation of ice-related processes, while the latter highlights the impact of mixed-phase cloud processes on upper-level dynamics. Both point out the need for a better understanding of cloud microphysical processes to improve the forecasts of upper-tropospheric dynamics. In addition, precipitation efficiency related to WCB activity is highly sensitive to cloud condensation nucleus (CCN) concentrations (Oertel et al., 2025b). Although CCNs are crucial for initial cloud formation and studies have also demonstrated their relevance to modeling convective systems and associated precipitation, their numbers are still poorly constrained by observations, and the precipitation response is case dependent (Schneider et al., 2019; Barthlott et al., 2022). Because of these uncertainties in CCN concentrations, correct precipitation forecasting poses a challenge.

To this day, it is still unclear how cloud microphysical parameterizations affect the cloud structure of WCBs in detail, which is relevant for precipitation and cloud radiative effects (CREs). In order to gain a better understanding of this and contribute to model improvement in the future, the following research questions are investigated:

1. How do varying CCN concentrations influence the WCB cloud structure?

2. To which cloud microphysical processes can the observed changes be attributed?

3. How does the influence of CCN perturbations compare to other cloud microphysical parameters and environmental perturbations?

4. How is the radiation balance at the top of the atmosphere affected by these perturbations?

To this end, sensitivity experiments are conducted in which, in addition to CCNs, four additional model parameters are systematically perturbed. For this, a so-called perturbed parameter ensemble (PPE) of a WCB case study is built using the ICOsahedral Nonhydrostatic (ICON) model.

The thesis is structured as follows: First, an overview of meteorological background information on cloud microphysical processes (Section 2.1) and WCBs (Section 2.2) is given. Second, the ICON model (Section 3.1) and PPE simulations (Section 3.2) are introduced, followed by a description of the applied Eulerian and Lagrangian diagnostics (Section 3.3), as well as the surrogate models (Section 3.4) and variance decomposition (Section 3.5) used to further quantify the relative importance of the perturbed parameters. After that, the case study is presented in Chapter 4. Next, the qualitative parameter impacts (Chapter 5) and quantification of uncertainty contributions (Chapter 6) are shown. Lastly, a discussion (Chapter 7) and a conclusion (Chapter 8) of the results are provided.

2 Meteorological Background

This Chapter introduces the meteorological background knowledge relevant to analyzing the WCB cloud structure. This includes cloud microphysics (Section 2.1) and WCBs (Section 2.2). For more details on cloud microphysics, see Lamb and Verlinde (2011) Chapters 11 and 12.

2.1 Cloud Microphysical Processes

Clouds consist of liquid and solid particles, the so-called hydrometeors, namely liquid droplets, ice crystals, aggregates, and rimed particles. In cloud models, these hydrometeors need to be artificially categorized to represent them, which will be discussed in more detail later. Cloud microphysical processes describe how these individual hydrometeors form, grow, change between the gas, liquid, and solid phases, and dissipate. These processes are active at nanometer and micrometer scales. Furthermore, the processes are divided into those that occur in warm clouds, mixed-phase regions of clouds, and those that take place solely in cold clouds. Warm clouds only contain water in the liquid phase and have temperatures above 0 °C. In contrast, cold clouds are termed “cold” as their temperatures are below 0 °C. However, between 0 °C and −38 °C, clouds can contain supercooled liquid water that coexists with the ice phase. This region is called the "mixed-phase" region.

Figure 2.1 of Lamb and Verlinde (2011) shows the phase diagram of water that illustrates in which phase water occurs depending on its temperature T and partial pressure e. The solid lines are the phase boundaries that indicate at which temperatures and partial pressures of water vapor two water phases coexist in equilibrium. At the triple point (273.16 K, 6.117 hPa), all three phases coexist in equilibrium. The dashed line of metastable liquid is relevant for mixed-phase clouds, as it indicates the conditions under which supercooled liquid water can occur. Furthermore, the Clausius-Clapeyron equation

$$\frac{de_\mathrm{s}}{dT} = \frac{l_\mathrm{v} e_\mathrm{s}}{R^* T^2} \tag{2.1}$$

represents an essential concept in cloud physics, and describes the saturation water vapor pressure e_s at which liquid water and water vapor coexist in equilibrium. In other words, e_s indicates saturation with respect to liquid. It depends on the temperature T, latent heat of vaporization l_v, and universal gas constant R^*. If $e > e_\mathrm{s}$, supersaturation w.r.t. liquid is present, which is also expressed by the saturation ratio

$$S = \frac{e}{e_\mathrm{s}} \tag{2.2}$$

being greater than 1. Analogously, a saturation ratio w.r.t. to ice can be defined as $S_\mathrm{i} = \frac{e}{e_\mathrm{i}}$ with e_i being the partial pressure at which water vapor and ice are in equilibrium, i.e., the saturation water

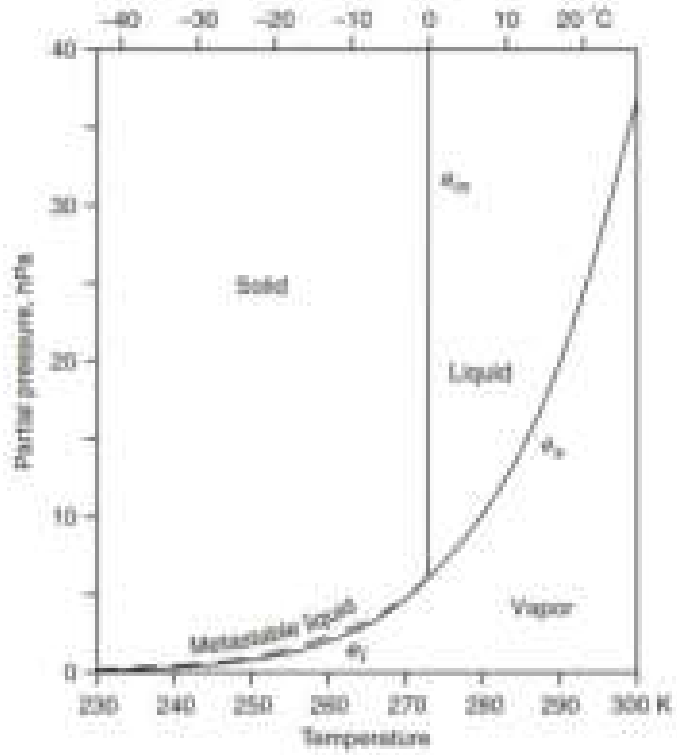

Figure 2.1: Phase diagram of water (modified from Lamb and Verlinde, 2011). Solid lines denote the lines of equilibrium where two phases coexist in equilibrium: e_s is the saturation vapor pressure w.r.t. liquid and e_i w.r.t. ice. At the melting curve e_m, liquid water and ice are in equilibrium. All three phases coexist at the triple point (273.16 K, 6.117 hPa). The dashed line (Metastable liquid) is the extension of e_s and represents the conditions for supercooled liquid water.

vapor pressure w.r.t. ice. e_i can also be calculated with the Clausius-Clapeyron equation (2.1) when l_v is replaced by the latent heat of sublimation l_s. Moreover, $e_s > e_i$ applies, which is important for mixed-phase cloud processes and will be discussed later.

2.1.1 Warm Clouds

In general, the processes of warm clouds also occur in the mixed-phase regions of cold clouds, however, frozen hydrometeors do not influence them.

CCN Activation For the initial formation of a liquid cloud droplet in the atmosphere, a so-called cloud condensation nucleus is needed for water vapor to condense onto it. Generally, not all aerosol particles act as CCNs. The most efficient ones are hygroscopic, which means they absorb water and can dissolve completely in water, such as sea salt. A CCN is required to be already solved in water. For cloud droplet formation, enough water vapor has to condense onto this liquid solution droplet for it to reach its critical radius r_c. Once this critical radius is reached, the CCN is activated, which means the droplet begins to grow to the size of a cloud droplet. If the critical radius is not reached, the droplet is classified as a haze particle. The Köhler equation

$$S = \left(1 + \frac{A}{r_\mathrm{d}}\right)\left(1 - \frac{B}{r_\mathrm{d}^3}\right) \approx 1 + \frac{A}{r_\mathrm{d}} - \frac{B}{r_\mathrm{d}^3} \tag{2.3}$$

describes this process in detail, and includes two important factors, the so-called Kelvin $1 + A/r_\mathrm{d}$ and Raoult term $1 - B/r_\mathrm{d}^3$. In Eq. 2.3, S (Eq. 2.2) is the saturation ratio in equilibrium at the surface of the growing droplet with the water vapor pressure of the droplet $e = e_\mathrm{d}(r_\mathrm{d})$ and the droplet radius r_d. The Kelvin term $(1 + A/r_\mathrm{d})$ considers the effect that the curvature $\frac{1}{r_\mathrm{d}}$ of the liquid droplet has on e_d:

$$A = \frac{2M_\mathrm{w}\sigma_\mathrm{w}}{R^* T \rho_\mathrm{w}}, \tag{2.4}$$

where M_w denotes the molar mass of water, σ_w the surface tension of water and ρ_w the density of water. For smaller r_d, a higher e_d is needed to maintain a dynamic equilibrium, otherwise the droplet would evaporate. The effect the solute has on e_d is described by the Raoult term $(1 - B/r_\mathrm{d}^3)$ with

$$B = \frac{3M_\mathrm{w} i n_\mathrm{s}}{4\pi\rho_\mathrm{w}}, \tag{2.5}$$

where i is the Van't Hoff factor, which takes the dissociation of the solute into account, and n_s the number of moles of the solute. A lower e_d is needed to maintain the equilibrium, as the solute impedes evaporation of the droplet. Besides, both A and B are weakly temperature-dependent due to their dependence on the density of water.

Figure 2.2 outlines the so-called Köhler curve described by the Köhler equation (2.3). It illustrates the need for a sufficiently high supersaturation ($S > 1$) so that the maximum of the curve, which is the critical supersaturation S_c, is reached and the droplet radius subsequently exceeds the critical radius r_c to become a cloud droplet. When $r_\mathrm{d} < r_\mathrm{c}$ applies, a haze droplet is present instead.

Condensational Growth After CCNs are activated and cloud droplets are formed, they can grow by condensation of water vapor onto them, when supersaturation w.r.t. liquid is given at the droplets' surfaces, i.e. $e_\mathrm{d} > e_\mathrm{s}$. For this, a cloud droplet is required to be in an environment with sufficient water vapor, so that a diffusional flux of water vapor to the droplet surface can be established. The condensational growth of a cloud droplet is described by the time derivative of its mass

$$\frac{dm_\mathrm{d}}{dt} = 4\pi r_\mathrm{d} \rho_\mathrm{w} G s, \tag{2.6}$$

with G as the effective diffusivity and $s = S - 1$ as the supersaturation w.r.t. liquid. Furthermore, the temporal evolution of the droplet radius is proportional to its reciprocal r_d^{-1}, or, in other words, $r_\mathrm{d}(t) \sim \sqrt{t}$, causing the smallest droplets to grow the fastest and condensational growth to slow down over time. For cloud droplets to be categorized as raindrops, they need to have a diameter of $\geq 100\,\mu$m and a larger associated fall velocity. To grow sufficiently in size, additional processes

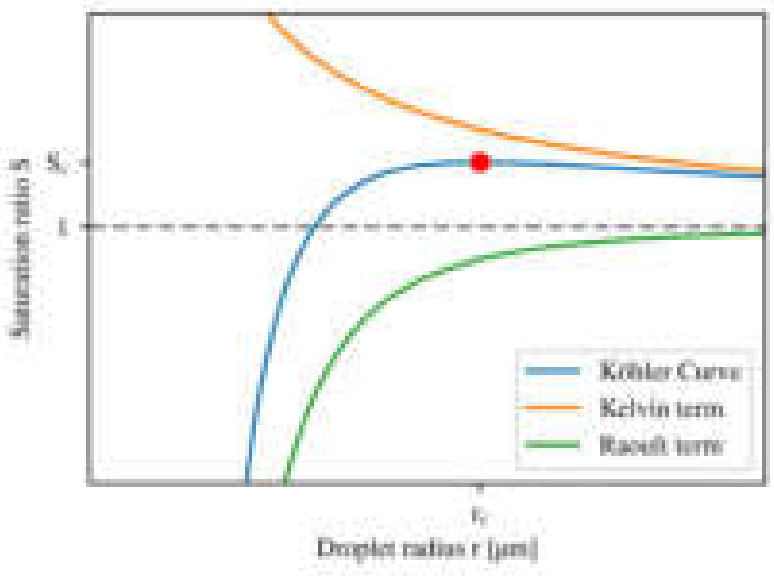

Figure 2.2: Example of a Köhler curve (blue) and its Kelvin (orange) and Raoult (green) term. The red circle indicates the maximum of this Köhler curve, i.e., the critical supersaturation S_c with the corresponding critical radius r_c. For the calculations, the following values are assumed: molar mass of water $M_w = 18.015\,\mathrm{g\,mol^{-1}}$, surface tension of water $\sigma_w = 0.0769\,\mathrm{N\,m^{-1}}$, universal gas constant $R^* = 8.314\,\mathrm{J\,(mol\,K)^{-1}}$, temperature $T = 253\,\mathrm{K}$, density of water $\rho_w = 997\,\mathrm{kg\,m^{-3}}$, Van't Hoff factor $i = 2$ and number of moles of solute $n_s = 1.7 \times 10^{-15}\,\mathrm{mol}$.

are required, as condensational growth alone does not suffice. Those processes are collision and coalescence.

Continuous Collection For cloud droplets to grow significantly in size, they need to first collide with each other and then remain attached afterward, i.e., coalesce, to form raindrops. This subsequently decreases the liquid water droplet number concentration. However, the water mass concentration remains the same, since when two droplets collide and coalesce, the mass of one droplet increases by the mass of the other, whereas the other droplet is extinguished. Collisions of droplets can occur due to differences in their fall velocities, which result from variations in their sizes. It is assumed that a larger drop continuously "collects" smaller droplets by collision and subsequent coalescence as it falls. This process is called continuous collection. Note that cloud droplets can also grow via stochastic collection, where collisions are caused by turbulent movement instead of the difference in fall velocities.

Yet, not every collision may lead to coalescence. Larger drops can become unstable and shatter by collision, increasing the drop number concentration. In addition, smaller droplets might bounce off larger ones because the latter can deform and create air cushions between the drops. In this case, the number concentration remains unchanged. Besides, very small droplets have low inertia and tend to follow the air flow around larger drops. As a result, they are harder to collect, which is why the collision efficiency decreases for smaller droplets. In general, raindrop sizes are often not reached in warm clouds, and thus, warm clouds are only able to produce light precipitation, if any.

2.1.2 Cold Clouds

The following provides a brief theoretical introduction to the microphysical processes of cold clouds (see Lamb and Verlinde, 2011, Chapter 12). Note that processes involving liquid water droplets occur only in mixed-phase regions of cold clouds.

Primary Ice Formation Primary ice formation depicts the initial formation of ice crystals. Thus, the ice mass and number concentration of a cloud increase. Primary ice formation occurs by either homogeneous or heterogeneous ice nucleation (Fig. 2.3). According to Vali et al. (2015), ice nucleation is a process by which liquid water or water vapor is transformed into thermodynamically stable ice for the first time. When ice nucleation occurs homogeneously, only the initial water phase (liquid or gas) is involved in the phase transition. However, homogeneous ice nucleation occurs only for liquid water because water vapor would need a very high supersaturation to directly form ice, which is not observed in the atmosphere (Vali et al., 2015). At temperatures below $-38\,^{\circ}\mathrm{C}$, homogeneous freezing of supercooled cloud droplets and homogeneous freezing of supercooled solution droplets take place (Hoose and Möhler, 2012). As illustrated in Figure 2.3, several different pathways for primary ice formation exist, which all occur under specific temperature T and ice saturation ratio S_i conditions. Both homogeneous freezing of supercooled cloud droplets and homogeneous freezing of supercooled solution droplets require a high $S_\mathrm{i} > 1.3$, and homogeneous freezing of cloud droplets also requires saturation w.r.t. liquid (solid line).

In contrast, heterogeneous ice nucleation involves the initial water phase and the surface of an external agent (Vali et al., 2015). This external agent is an aerosol particle, which is called ice nucleating particle (INP) since it supports ice nucleation. Similar to CCNs, not all aerosols can act as INPs. Efficient INPs are, for example, mineral dust, biological particles, such as bacteria or fungal spores, or soot (Hoose and Möhler, 2012). Heterogeneous ice nucleation includes deposition nucleation, immersion freezing, and contact freezing (Vali et al., 2015). All of these heterogeneous nucleation processes generally occur at higher temperatures compared to homogeneous ice nucleation and require less supersaturation w.r.t. ice, as shown in Fig. 2.3. Deposition nucleation refers to the direct formation of ice on an INP from supersaturated water vapor without going through the liquid phase. Immersion freezing is the freezing of a supercooled liquid cloud or solution droplet that has an INP immersed in itself. Contact freezing occurs when an INP touches the surface of a supercooled liquid cloud droplet and triggers freezing.

Depositional Growth Depositional growth describes the deposition of water vapor onto frozen hydrometeor particles, resulting in the growth of mass and size. Conceptually, it is similar to the condensational growth (2.6) of cloud droplets. The time derivative of the particle mass m_p is given by

$$\frac{dm_\mathrm{p}}{dt} = 4\pi C \rho_\mathrm{i} G'_\mathrm{i} s_\mathrm{i}, \tag{2.7}$$

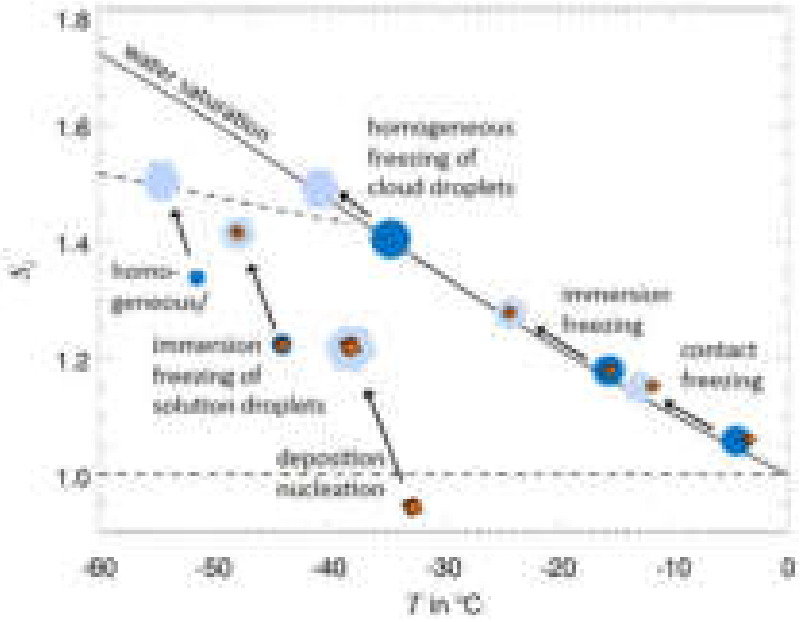

Figure 2.3: Overview of homogeneous and heterogeneous ice nucleation modes (modified from Hoose and Möhler, 2012). The solid line indicates the ice saturation ratio S_i depending on temperature T at liquid water saturation. Ice nucleating particles (INPs) are represented as orange cubes, liquid droplets as dark blue circles, and ice as light blue hexagons.

with the ice density ρ_i, the growth parameter of ice G'_i, the supersaturation w.r.t. ice s_i, and the capacitance C. The latter takes into account the shape and size of different frozen hydrometeors and influences the depositional growth rate. A lower capacitance results in slower depositional growth.

Aggregation The process of larger ice crystals collecting smaller ones is named aggregation. It increases the mass while decreasing the number concentration of ice. Snow is formed by aggregation or depositional growth of ice.

Wegener-Bergeron-Findeisen Process In general, the saturation vapor pressure w.r.t. ice e_i is lower than the one w.r.t. liquid e_s (Fig. 2.1), leading to three scenarios in mixed-phase clouds: (i) If supercooled liquid water droplets and ice particles are in an environment with a partial water vapor pressure of $e_s > e_i > e$, then both evaporate as the environment is subsaturated w.r.t. liquid and w.r.t. ice. (ii) If $e_s > e > e_i$ applies, the supercooled liquid water droplets evaporate because the environment is subsaturated w.r.t. liquid. Simultaneously, because of the environmental supersaturation w.r.t. ice, the water vapor deposits onto nearby ice particles. Thus, ice particles grow at the expense of liquid droplets. This is the so-called Wegener-Bergeron-Findeisen (WBF) process. (iii) If $e > e_s > e_i$ is the case, then both liquid droplets and ice particles grow through condensation and deposition, respectively, as the environment is supersaturated w.r.t. liquid and w.r.t. ice.

Riming In mixed-phase clouds, riming is the process of supercooled liquid water colliding with frozen hydrometeors and freezing onto them. This increases the ice mass concentration, whereas the ice number concentration is not affected. A heavily rimed ice crystal is called graupel when it is so obscured that the initial ice crystal is no longer recognizable. Graupel that exceeds a diameter of 5 mm is termed hail.

Secondary Ice Production The observed number concentrations of ice particles are larger than the number concentrations of INPs due to secondary ice production (SIP). SIP is the formation of new ice particles from pre-existing ice. Therefore, it increases the ice number concentration, while the ice mass concentration remains unchanged. According to Korolev and Leisner (2020), there are six different SIP mechanisms: splintering during riming, the so-called Hallett-Mossop process or rime-splintering, shattering during freezing of large supercooled drops, activation of INPs in transient supersaturation around freezing drops, and fragmentation caused by ice-ice collisions, thermal shock, or fragmentation of sublimating ice. All mechanisms require certain sizes of the hydrometeors involved and temperatures. For example, rime-splintering occurs between $-8\,^{\circ}\mathrm{C}$ and $-3\,^{\circ}\mathrm{C}$, the graupel particles have to be $\geq 0.5\,\mathrm{mm}$ in diameter and the accreted cloud droplets $\geq 25\,\mu\mathrm{m}$ in diameter.

2.1.3 Numerical Weather Prediction Models

To predict the formation and occurrence of clouds, particularly on larger scales, numerical weather prediction (NWP) models are used. NWP models are computer models that simulate the atmospheric state to predict future weather based on an initial state derived from meteorological observations and equations. The latter includes fundamental physical principles, such as the conservation of momentum, which is described by the Navier-Stokes equation, the conservation of mass represented by the continuity equation, the conservation of energy described by the thermodynamic energy equation, and the ideal gas law. Except for the ideal gas law, these equations form a set of coupled nonlinear partial differential equations that cannot be solved analytically. Therefore, numerical methods are applied to approximate, discretize, and solve them (Durran, 2010; Warner, 2010).

The discretization of the equations requires a grid on which the equations are solved at each grid point. Thus, only processes that occur on the scale of the grid can be resolved. However, so-called subgrid-scale processes exist and can influence grid-scale processes. That is why unresolved subgrid-scale processes, such as diabatic heating from radiative transfer or cloud microphysics, are parameterized in NWP models. With parameterizations, subgrid-scale processes are represented using prognostic variables resolved by the model. To account for the influence of subgrid-scale processes on the grid-scale processes, parameterizations feed back into the prognostic variables through, e.g., latent heating during phase changes of water. According to Straka (2009), the parameterizations of precipitation and cloud microphysical processes are not only relevant for NWP models on the scale of individual clouds, but also on mesoscales, synoptic, global, and climate scales.

Because the cloud microphysical processes described in Sections 2.1.1 and 2.1.2 cannot explicitly be represented due to differences in scale, several approaches have been developed to parameterize them. The two most commonly used types of cloud microphysical parameterizations are bin schemes and bulk schemes (Warner, 2010; Straka, 2009), but there are also newer methods, such as Lagrangian particle-based schemes (Morrison et al., 2020). Bin schemes work with hydrometeor particle size distribution (PSD) functions f that depend on the radius of the particles, and are divided into intervals or bins. Distribution functions can also depend on the mass of the particles instead of the radius. Bin schemes are computationally expensive because they predict the hydrometeor concentrations of every hydrometeor type for each bin. That is why in operational NWP, the computationally less expensive bulk schemes are used. Bulk schemes do not use complete PSDs but instead work with statistical moments of the PSD functions f to predict the number or mass concentrations of hydrometeors. According to Khain et al. (2015), the k-th statistical moment of the PSD f is given by

$$M^{(k)} = \int_0^\infty m^k f(m) dm, \tag{2.8}$$

with particle mass m and integer k. For the PSD f of each hydrometeor type, prescribed functions are used, most commonly exponential or gamma functions (Khain et al., 2015). The zeroth moment ($k = 0$) of f corresponds to the hydrometeor number concentration and the first moment ($k = 1$) to the hydrometeor mass concentration. Furthermore, bulk schemes are specified according to the number of moments used. A one-moment or single-moment scheme predicts only one moment, typically the mass concentration. In contrast, two-moment or double-moment schemes predict the mass and number concentration. Note that the prescribed functions pose a challenge for accurate weather forecasting, as they contain uncertain parameters and are themselves uncertain (Khain et al., 2015), especially when not well-understood processes like SIP are involved (Field et al., 2017).

The modified version (Oertel et al., 2023) of the scheme by Hande et al. (2016) is used to illustrate CCN activation in the following. The number concentration of activated cloud droplets $M_c^0 \equiv N_c$ depends on the grid-scale vertical velocity w and the pressure p and is described by

$$N_c(w,p) = N_a(p) \cdot \left(1 + e^{-B(p)\cdot \ln(w) - C(p)}\right)^{-1}, \tag{2.9}$$

with the aerosol number concentration

$$N_a(p) = \begin{cases} (250+7)\,\mathrm{cm}^{-3}, & \text{if } p \geq 800\,\mathrm{hPa} \\ \left(250 \cdot e^{\frac{p-800\,\mathrm{hPa}}{150\,\mathrm{hPa}}} + 7 \cdot e^{\frac{p-800\,\mathrm{hPa}}{400\,\mathrm{hPa}}}\right)\mathrm{cm}^{-3}, & \text{else,} \end{cases} \tag{2.10}$$

that is assumed to be constant in the boundary layer for $p \geq 800\,\text{hPa}$ and to decrease above. For the accumulation mode, a scale height of 150 hPa is assumed, and for the coarse mode, a scale height of 400 hPa. The pressure-dependent coefficients are

$$
\begin{aligned}
B(p) &= b_1 \cdot e^{-b_2 \cdot p + b_3}, \\
C(p) &= c_1 \cdot e^{-c_2 \cdot p + c_3}, \\
b_1 &= 3.46281429 \times 10^{0}, \quad b_2 = 1.74926665 \times 10^{-4}, \quad b_3 = -2.85967514 \times 10^{-1}, \\
c_1 &= 2.72664755 \times 10^{0}, \quad c_2 = 1.12852352 \times 10^{-3}, \quad c_3 = 1.50069026 \times 10^{0}.
\end{aligned}
$$

2.2 Warm Conveyor Belt

Aside from being responsible for most of the precipitation in the mid-latitudes (Pfahl et al., 2014), WCBs transport pollution from the lower to the upper troposphere (Stohl, 2001; Joos et al., 2017). A WCB is a slantwise ascending moist airstream associated with an ETC (Madonna et al., 2014). It is located in the ETC's warm sector ahead of the surface cold front. In particular, WCBs are characterized by Lagrangian air parcels that ascend poleward, begin in the boundary layer, and rise to the upper troposphere, while surmounting at least 600 hPa within two days (Wernli and Davies, 1997; Madonna et al., 2014). Furthermore, WCBs occur more frequently in winter than in summer, have a more pronounced seasonal cycle in the Northern Hemisphere and usually begin to ascend over the oceans between 20° and 47 °N, as well as within 17°-42 °S (Madonna et al., 2014). Other features are the formation of an elongated cloud band (Madonna et al., 2014; Eckhardt et al., 2004), alteration of the extratropical cloud radiative forcing or CRE (Joos, 2019), and potential modification of the large-scale atmospheric circulation (Joos and Wernli, 2012; Madonna et al., 2014). The latter is related to the modification of PV through diabatic heating within the WCB, leading to a negative PV anomaly in the upper and a positive PV anomaly in the lower troposphere (Madonna et al., 2014; Joos and Wernli, 2012). According to Binder et al. (2016), the WCB's positive low-level PV anomaly can lead to ETC intensification and Grams et al. (2011) state, that the negative upper-level PV anomaly can enhance upper-level ridges downstream of ETCs.

2.2.1 Cloud Microphysical Processes

Acents of WCBs are closely linked to a variety of cloud microphysical processes, which are described in Section 2.1.1 and 2.1.2 in detail. During the ascent, warm-, mixed-, and ice-phase processes occur as WCB air parcels experience a large temperature range. According to Madonna et al. (2014), the WCB initially takes up water vapor in the boundary layer, which then decreases during the ascent due to an increase in liquid water mass concentration caused by condensational growth of cloud droplets in the warm phase. As air parcels rise to higher altitudes, ice starts to form by freezing liquid cloud water in the mixed-phase, leading to an increase in ice water content (IWC) while decreasing liquid water content (LWC). Simultaneously, depositional growth of ice in the mixed- and ice phase causes the water vapor to decline further. All of these microphysical processes

are important because they contribute to diabatic heating, which influences the PV and subsequently large-scale dynamics (Joos and Wernli, 2012; Madonna et al., 2014). Especially condensation of water vapor and depositional growth of snow are highly relevant, since each process is responsible for approximately 10 K of the total latent heating, which makes them the largest contributors to the total latent heating (Joos and Wernli, 2012). In addition, Joos and Wernli (2012) stress that the WCB not only gives rise to a region of pronounced heating due to cloud formation, but is also responsible for strong cooling beneath it due to the evaporation of rain and sublimation or melting of snow. Furthermore, other studies found that fast WCB ascents occur with stronger latent heating (Oertel et al., 2021; Mazoyer et al., 2021).

Because microphysical processes determine the cloud structure and therefore have an impact on the radiation balance and because they also play a crucial role in precipitation formation and diabatic heating, a detailed description of microphysical processes in models is essential. However, there are still uncertainties in the representation of cloud microphysics. For example, uncertainties in diabatic heating arise from uncertainties in vapor deposition (Forbes and Clark, 2003; Mazoyer et al., 2021, 2023) which influence ice, snow, and graupel mass concentrations. In particular, the values of the normalized capacitance are not well constrained (Westbrook and Heymsfield, 2011). Besides, Oertel et al. (2020, 2021) highlight the importance of convection embedded in WCBs for precipitation formation, which has the potential to cause particularly strong surface precipitation. In addition, the WCB precipitation efficiency is highly sensitive to CCN concentrations (Oertel et al., 2025b).

2.2.2 Cloud Condensation Nucleus Impacts

The impact of aerosol particle number concentrations on WCBs, i.e., varying CCN concentrations, is not sufficiently studied. Joos et al. (2017) found in their climatological model study on WCB precipitation in the North Pacific that polluted WCB trajectories show a slight delay and reduction in precipitation formation compared to clean trajectories. However, all WCBs contain both clean and polluted trajectories at the beginning of their ascent. Typically, more clean trajectories are present, which strongly diminish the aerosol influence from the polluted ones.

Recent studies (Barthlott et al., 2022; Schneider et al., 2019) investigated the impact of aerosols on convective clouds for different weather regimes. Both studies performed sensitivity simulations with varying CCN concentrations over Germany, including parts of neighboring countries. Barthlott et al. (2022) found that with an increase in CCN concentrations, the total cloud water mass concentration increases systematically, however, the total rain water mass concentration decreases. Additionally, their results showed that higher CCN concentrations lead to a shift of the cloud droplet size distribution's maximum to smaller values, as well as a decrease of the effective radius and an increase of the cloud optical depth. Schneider et al. (2019) also concluded that especially the CCN concentrations heavily influence the cloud and precipitation structures. Nevertheless, they found the CCN concentrations' impact to be dependent on environmental conditions and contributions of cold- and warm-rain processes, resulting in either a decrease or an increase in precipitation. In fact, Schneider et al. (2019) showed that for weaker updrafts, warm-phase processes dominate,

leading to a precipitation reduction with increasing CCN concentrations. In contrast, cold-phase processes dominate in stronger updrafts, causing precipitation to increase with higher CCN amounts. However, the results of both studies are not directly applicable to WCBs since they are heavily influenced by synoptic conditions and their vertical velocities are considerably lower compared to convective systems (Oertel et al., 2023).

2.2.3 Cloud Radiative Effects

WCBs affect extratropical cloud radiative effects (Joos, 2019). CRE is defined as the net radiation at the top of atmosphere (TOA) with clouds minus the net radiation at TOA without clouds. It can be distinguished between shortwave cloud radiative effect (SWCRE) and longwave cloud radiative effect (LWCRE). A positive CRE means that clouds have a warming effect, whereas a negative CRE indicates a cooling effect. Generally, on a global average, clouds cool the Earth with their negative SWCRE and warm it with their positive LWCRE.

Joos (2019) states that the net CRE is highly variable along the WCB ascent in the winter hemisphere because the inflow region exhibits a negative net CRE due to prevailing SWCRE. In contrast, LWCRE dominates in the outflow region, which is attributed to the absence of incoming solar radiation caused by the WCB's poleward movement. Another finding of Joos (2019) is a pronounced negative net CRE in the summer hemisphere because of available solar radiation and high cloud albedo.

Furthermore, McCoy et al. (2018) show with observations and idealized simulations that an increase in cloud droplet number concentration leads to a higher cloud liquid water path in WCBs and alters the cloud albedo that affects CRE.

3 Methodology

This Chapter gives an introduction to the applied methods, starting with the ICON model (Section 3.1), which is used to conduct perturbed parameter ensemble (PPE) simulations (Section 3.2) with five uncertain input parameters. Those simulations are then analyzed with the Eulerian and Lagrangian diagnostics (Section 3.3). In addition, a variance decomposition (Section 3.5) is performed to quantify the individual influences of the five perturbed parameters on the WCB cloud structure. For this sensitivity analysis, a huge number of simulations with different parameter combinations is needed to cover the combined parameter space. As it would be computationally expensive and not feasible to run such simulations with a full NWP model, surrogate models (Section 3.4) are needed.

3.1 ICOsahedral Nonhydrostatic Model

The PPE simulations are performed with the ICON model (version 2.6.2.2; Zängl et al., 2015) for a WCB that was observed over the North Atlantic in October 2016 during the NAWDEX campaign (intensive observation period 7; Schäfler et al., 2018). For this, the simulations by Oertel et al. (2025b) are used, comprising a global simulation with approximately 13 km effective grid spacing (R03B07 grid) and 120 s time steps, and two high-resolution nests with approximately 6.5 km (R03B08 grid) and 3.3 km (R03B09 grid) effective grid spacing. Their respective time steps are 60 and 30 s. The refined nests are coupled by two-way nesting, i.e., the global domain provides lateral boundary conditions for the first high-resolution nest, whereas the high-resolution nest nudges the prognostic fields of the global domain towards their solution. Analogously, the first high-resolution nest provides lateral boundary conditions for the second high-resolution nest, which in turn gives information back to the former. The simulations are initialized from the European Centre for Medium-Range Weather Forecasts analysis at 18 UTC 3 October 2016 and run freely for the next 72 hours.

To represent cloud microphysical processes, the two-moment microphysics scheme of Seifert and Beheng (2006) is applied with six hydrometeor types: cloud, rain, ice, snow, graupel, and hail. The two-moment scheme predicts the mass concentrations (cloud water q_c, rain q_r, ice q_i, snow q_s, graupel q_g, and hail q_h) of the different hydrometeors and their respective number concentrations, denoted by n_k. Other processes such as CCN activation, heterogeneous and homogeneous ice nucleation, depositional growth of ice phase hydrometeors, and saturation adjustment are represented following Oertel et al. (2023).

Table 3.1: Uncertain parameters of the PPE with their respective ranges, units and affected processes (Oertel et al., 2025b).

Parameter	Min	Max	Unit	Affected process
CCN	0.4	20	scaling factor	cloud droplet activation
INP	0.01	20	scaling factor	ice nucleation
CAP	0.2	1	scaling factor	depositional growth of ice and snow
SST	−2	2	K	latent and sensible heat fluxes over ocean surface
SAT	0	0.1	scaling factor	condensation from saturation adjustment scheme

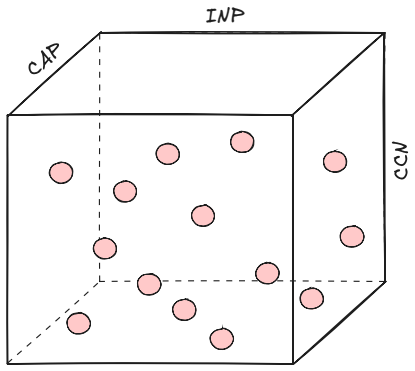

Figure 3.1: Example of a PPE with combined perturbations. The cube represents a three-dimensional phase space. It is spanned by the ranges of CAP, INP, and CCN perturbations. Each red circle depicts an PPE member with its respective parameter values. Figure created with Excalidraw (`https://excalidraw.com`, last accessed: 01.12.2024).

3.2 Perturbed Parameter Ensemble Simulations

For the sensitivity analysis, the approach of Oertel et al. (2025b) is followed by utilizing their ICON model simulations of the PPE of 70 members with $N_p = 5$ uncertain model parameters. In the PPE, each member contains combined perturbations of these uncertain parameters, which are CCN and INP concentrations, capacitance (CAP), SST, and maximum supersaturation with respect to liquid (SAT). They are chosen because they influence the WCB ascent and corresponding cloud formation (Oertel et al., 2025b). Table 3.1 shows the ranges of parameters as well as the processes affected by the perturbations. Using Latin hypercube sampling (Morris and Mitchell, 1995), ideal parameter perturbation combinations are determined to optimally cover the five-dimensional phase space spanned by the parameter ranges (Oertel et al., 2025b). To better understand the concept of combined perturbations, Figure 3.1 illustrates, as an example, a three-dimensional phase space as a cube. It is spanned by the ranges of CAP, INP, and CCN perturbations. Each red circle depicts a PPE member with its respective parameter perturbations. In addition, a unperturbed reference simulation (REF) is performed with scaling factors of $f_{CCN} = 1$, $f_{INP} = 1$, $f_{CAP} = 1$, $f_{SAT} = 0$ and constant offset $f_{SST} = 0$ (Oertel et al., 2025b). More information on all perturbed parameters and their minimum and maximum values is provided in the following. The selection of the parameter ranges follows Oertel et al. (2025b).

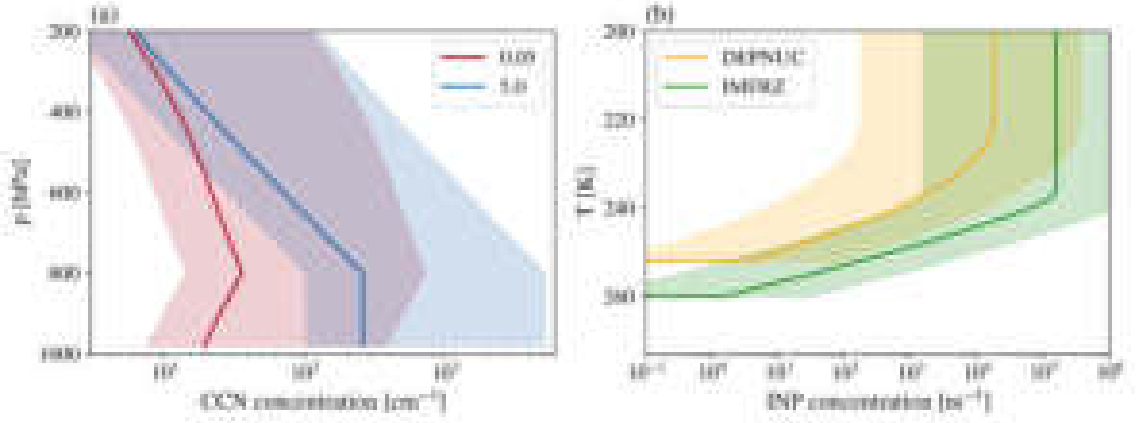

Figure 3.2: **(a)** Vertical profiles of parameterized cloud condensation nucleus (CCN) concentrations of the unperturbed reference simulation (REF) for different vertical velocities (colors, in ms^{-1}) together with CCN concentration ranges obtained by perturbations with the scaling factor f_{CCN} (shading). **(b)** Vertical profiles of parameterized ice nucleating particle (INP) concentrations of REF for a super saturation w.r.t. ice of 1.1 for immersion freezing (IMFRZ; green) and deposition nucleation (DEPNUC; orange) together with INP concentration ranges obtained by perturbations with the scaling factor f_{INP} (shading).

CCN CCN concentrations influence the amount of activated cloud droplets. In the ICON model, CCN activation is prescribed as a vertical profile, thus, it represents an uncertain parameter. Besides, cloud droplet activation has an impact on cloud microphysical process rates (Barthlott et al., 2022; Wellmann et al., 2018). The modified version (Oertel et al., 2023) of the scheme by Hande et al. (2016) is used to account for cloud droplet activation, which is scaled by the grid-scale vertical velocity and air pressure. Furthermore, a height-dependent CCN profile that is time-independent is assumed. The number of activated cloud droplets per time step is perturbed by a scaling factor f_{CCN} ranging between 0.4 and 20, leading to CCN concentrations between $100\,cm^{-3}$ and $5000\,cm^{-3}$. Figure 3.2a shows vertical profiles of the parameterized CCN concentrations of REF for two vertical velocities calculated with equation (2.10). Smallest and largest CCN concentrations made possible by perturbations with f_{CCN} are also shown as shading.

INP INP concentrations modify the ice number concentration produced by heterogeneous ice nucleation, and they are also prescribed in the ICON model, which is why they introduce parametric uncertainty as well. They are represented by the temperature-dependent functions of Hande et al. (2015). The rates of freezing of raindrops (Bigg, 1953), immersion freezing of cloud droplets, and deposition nucleation of cloud ice Hande et al. (2015) all depend on INP concentrations and are thus perturbed by a logarithmic scaling factor f_{INP} ranging from 0.01 to 20. Figure 3.2b shows vertical profiles of the parameterized INP concentrations of REF for immersion freezing and deposition nucleation. The shading indicates the range of the smallest and largest INP concentrations enabled by perturbations with the scaling factor f_{INP}.

CAP Generally, the CAP is a scaling parameter for the vapor deposition onto frozen hydrometeors while taking their habits and surfaces into account. Perturbing it, therefore, alters the depositional growth rate of frozen hydrometeors. For the sensitivity experiments, CAP of ice and snow is varied

simultaneously with the same scaling factor f_{CAP} between 0.2 and 1, leading to normalized CAP values between 0.1 and 0.5. CAP of graupel and hail remain unchanged, i.e., they match their respective radius, as they are assumed to be approaching the shape of a sphere.

SST The sea surface temperature refers to uncertainty in thermodynamic boundary conditions as modifying SST impacts the temperature and specific humidity of the WCB inflow in the lower troposphere (Christ et al., 2025). A constant offset f_{SST} between $-2\,\mathrm{K}$ and $2\,\mathrm{K}$ is introduced to perturb SST.

SAT To establish a thermodynamic equilibrium between cloud droplets and water vapor, either by evaporation or condensation of cloud droplets, a saturation adjustment scheme is implemented in the ICON model. It is called twice, namely once before and after the explicit microphysical processes. No supersaturation w.r.t liquid is possible if cloud droplets are present, since the scheme assumes that a thermodynamic equilibrium is instantly reached, as it directly removes any sub- or supersaturation. The saturation adjustment is perturbed by extending the possible maximum of the saturation ratio to values above 1. This is done by using a scaling factor f_{SAT}, ranging between 0 and 0.1, for the temperature- and pressure-dependent critical saturation specific humidity.

3.3 Eulerian and Lagrangian Diagnostics

Two perspectives are applied to analyze the impact of parameter perturbations on the WCB's cloud structure, as illustrated in Oertel et al. (2023). The first is the Eulerian approach, focusing on a fixed space relative to the cyclone's cold front where air parcels move through, and the second is the Lagrangian approach, which follows WCB air parcel trajectories.

3.3.1 Eulerian Perspective

In the Eulerian perspective, the focus lies on the cloud structure relative to the cyclone's cold front. Following the approach of Oertel et al. (2023), multiple west-east-oriented vertical cross-sections are placed through the WCB ascent region for several time steps. For every cross-section, new coordinates are defined relative to the cold front, i.e., 0° rel. lon. marks the western edge of the WCB ascent region ahead of the cold front. Subsequently, vertical cross-section composites are created by averaging over all cross-sections of October 4 and 5 when the WCB ascent is strongest. These cross-sections are calculated for the hydrometeor mass concentrations, number concentrations, as well as diabatic heating rates for all PPE members. An example of the composite cloud structure is shown in Fig. 4.2b.

To compare the cloud structure between different PPE members, the composites are averaged over the cyclone's warm sector (0°-8° rel. lon.) to produce comparable vertical profiles. The PPE members are divided into three subsets sorted by a perturbed parameter, e.g., CCN concentration.

The first subset contains the 23 PPE members which have the lowest perturbed parameter values or scaling, the second subset the 24 PPE members with moderate perturbed parameter values and the third subset, also consisting of 23 PPE members, includes the highest perturbed parameter values. With that, it is possible to discern a potential systematic impact of this perturbed parameter on the vertical profiles of the variables of interest. This approach is repeated for the remaining four perturbed parameters. Table A.1 shows the means of all parameter perturbations per subset in the Appendix. In Section 3.5, a more sophisticated diagnostic is introduced, i.e., the so-called variance decomposition, to better quantify the individual impacts of the perturbed parameters.

3.3.2 Lagrangian Perspective

In contrast, the Lagrangian perspective allows for a different kind of analysis. The same routine as in Oertel et al. (2023) is applied to calculate the online trajectories, which have an ascent rate of at least 600 hPa within 48 h. Moreover, the beginning of the fastest 600 hPa ascent along each trajectory marks the start of the WCB ascent. Each PPE member possesses several tens of thousands of trajectories, ranging from 28311 to 53802 WCB trajectories per simulation. To compare the PPE members with each other, an average trajectory is calculated for all hydrometeor mass concentrations and diabatic heating rates for each PPE member. With that, the averaged temporal evolution of the variables of the PPE members can be compared. However, the ascent speed of the individual trajectories in each simulation varies substantially and ranges, for example, from 2 to 48 hours to ascent 600 hPa. Hence, in addition, the trajectories are also divided into 2 K temperature bins along the ascent (Oertel et al., 2025b) to better analyze cloud microphysical processes which are strongly temperature-dependent, such as immersion freezing. Following the analysis approach of the Eulerian perspective, the trajectories are sorted by perturbed parameter, and variance decomposition is performed as well.

3.4 Surrogate Models

To generate sufficient data for the variance decomposition of different variables, surrogate models are used to approximate the values of these target variables, based on any combination of the perturbed parameters, instead of explicitly calculating them with the ICON model. In the following, the tests of different models are presented, and RFR models are introduced.

3.4.1 Model Tests

Multiple linear regression (MLR), Gaussian process emulation (GPE; Rasmussen, 2004) and random forest regression (Breiman, 2001) are tested as surrogate models for the mean vertically integrated hydrometeor mass concentrations $q_{\mathrm{x,t}}$ of the six hydrometeor types using their respective Scikit-learn python library (Pedregosa et al., 2011). For MLR and GPE, the default Scikit-learn models are used, and for the RFR, models are tested with $N_{\mathrm{tree}} = 250$ decision trees and all 5

Table 3.2: Mean absolute error (MAE; in kg m^{-2}), mean squared error (MSE), root mean squared error (RMSE; in kg m^{-2}) and R^2 score of multiple linear regression (MLR), random forest regression (RFR) and Gaussian process emulation (GPE) models for the mean vertically integrated hydrometeor mass concentrations of cloud water ($q_{c,t}$), rain ($q_{r,t}$), ice ($q_{i,t}$), snow ($q_{s,t}$), graupel ($q_{g,t}$) and hail ($q_{h,t}$).

Metric	Model	$q_{c,t}$	$q_{r,t}$	$q_{i,t}$	$q_{s,t}$	$q_{g,t}$	$q_{h,t}$
MAE	MLR	2.14×10^{-2}	5.30×10^{-3}	3.29×10^{-3}	9.66×10^{-3}	5.50×10^{-3}	3.58×10^{-4}
MAE	RFR	4.81×10^{-2}	4.20×10^{-3}	2.01×10^{-3}	1.05×10^{-2}	4.49×10^{-3}	2.76×10^{-4}
MAE	GPE	2.19×10^{-2}	4.00×10^{-3}	4.53×10^{-3}	8.25×10^{-3}	1.59×10^{-2}	1.97×10^{-4}
MSE	MLR	9.56×10^{-4}	5.03×10^{-5}	1.49×10^{-5}	1.46×10^{-4}	4.66×10^{-5}	2.13×10^{-7}
MSE	RFR	3.44×10^{-3}	2.87×10^{-5}	6.65×10^{-6}	1.47×10^{-4}	4.32×10^{-5}	1.55×10^{-7}
MSE	GPE	8.85×10^{-4}	2.50×10^{-5}	2.93×10^{-5}	1.04×10^{-4}	4.25×10^{-4}	1.24×10^{-7}
RMSE	MLR	3.09×10^{-2}	7.10×10^{-3}	3.86×10^{-3}	1.21×10^{-2}	6.83×10^{-3}	4.62×10^{-4}
RMSE	RFR	5.86×10^{-2}	5.36×10^{-3}	2.58×10^{-3}	1.21×10^{-2}	6.58×10^{-3}	3.94×10^{-4}
RMSE	GPE	2.98×10^{-2}	5.00×10^{-3}	5.41×10^{-3}	1.02×10^{-2}	2.06×10^{-2}	3.52×10^{-4}
R^2	MLR	0.967	0.748	0.570	0.632	0.941	0.933
R^2	RFR	0.883	0.857	0.808	0.629	0.945	0.951
R^2	GPE	0.970	0.875	0.157	0.738	0.462	0.961

perturbed parameters are considered per internal node. More details on RFR follow later. The mean $q_{x,t}$ is calculated by averaging over $0^\circ - 8^\circ$ rel. lon., whereas the models are trained with 50 of the 70 PPE members and validated with the remaining 20. The parameter perturbations of the training dataset are selected by using the Latin hypercube sampling to optimally fill the five-dimensional parameter space. For the validation dataset, the parameter perturbations are also selected with Latin hypercube sampling to fill the gaps in the training dataset optimally. Thus, the splitting of the 70 PPE members into training and validation sets is not random. To assess the performance of the models, scatter diagrams of the ICON model runs and model predictions (Fig. 3.3) are presented, as well as their respective mean absolute error (MAE), mean squared error (MSE), root mean squared error (RMSE) and coefficient of determination R^2 (Table 3.2). Equations (A.1)-(A.4) in Appendix A.1 are used to calculate these metrics. In general, the different model types perform quite similarly for the respective $q_{x,t}$ considering the scatter diagrams (Fig. 3.3). However, RFR performs overall best in terms of R^2 values, particularly for predicting the mean vertically integrated ice mass concentration $q_{i,t}$. That is why RFR is the method of choice for this thesis.

3.4.2 Random Forest Regression

As RFR is selected to build surrogate models, the underlying principle is explained in the following in more detail. RFR is a machine learning algorithm that "grows" N decision trees based on random subsamples of the training dataset. In this case, the training dataset contains 50 combinations of the five perturbed parameters, the so-called features, and their respective ICON model output of a target

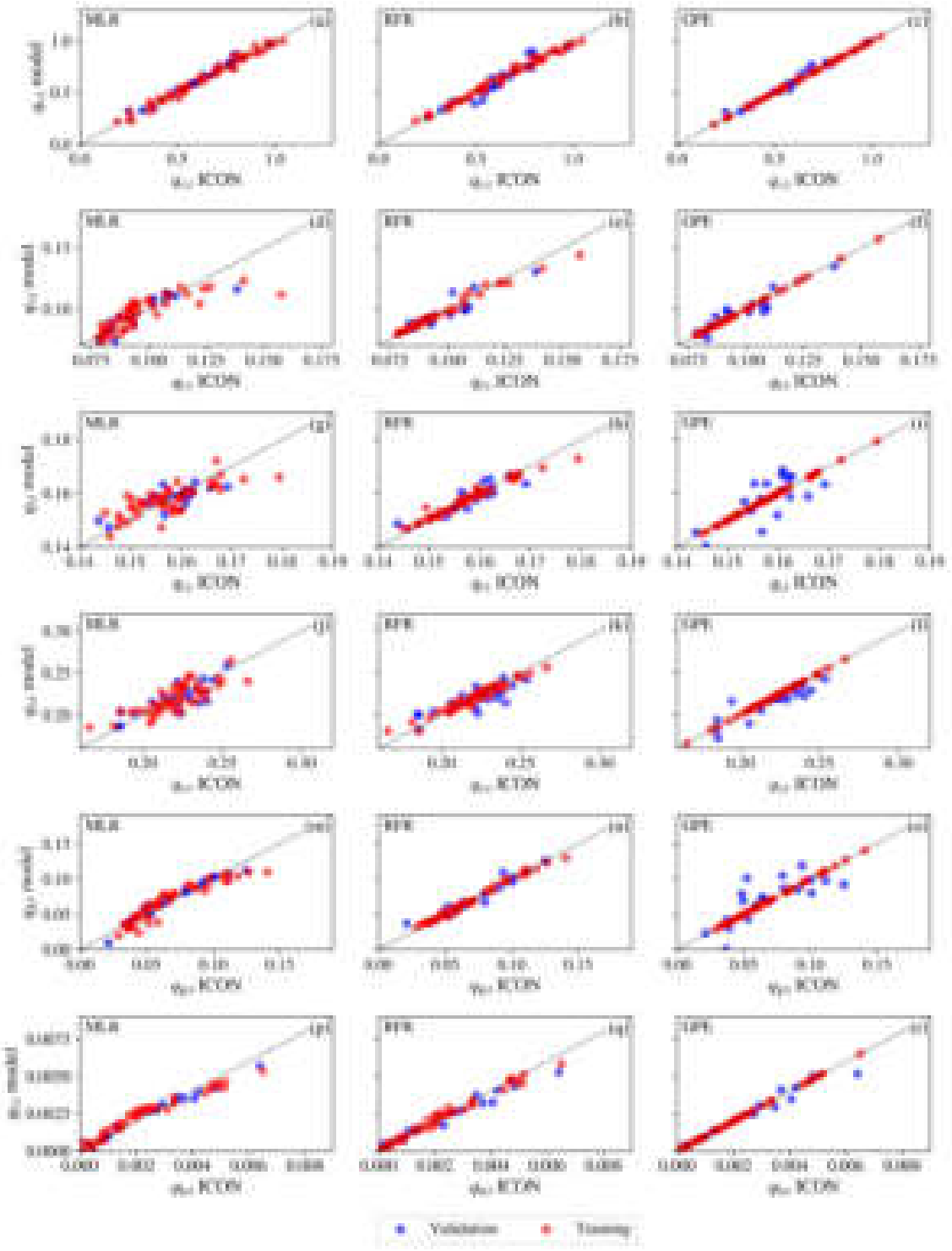

Figure 3.3: Scatter diagrams of multiple linear regression (MLR), random forest regression (RFR), and Gaussian process emulation (GPE) model performance of mean vertically integrated mass concentrations for **(a)-(c)** cloud water ($q_{c,t}$, in $kg\,m^{-2}$), **(d)-(f)** rain ($q_{r,t}$), **(g)-(i)** ice ($q_{i,t}$), **(j)-(l)** snow ($q_{s,t}$), **(m)-(o)** graupel ($q_{g,t}$), and **(p)-(r)** hail ($q_{h,t}$). For all panels, validation PPE members are colored blue and training PPE members red. Mean vertically integrated hydrometeor mass concentrations of the ICON model runs are shown on the x-axis, and the mean vertically integrated hydrometeor mass concentrations of the respective model are on the y-axis. Errors of the validation dataset are listed in Table 3.2.

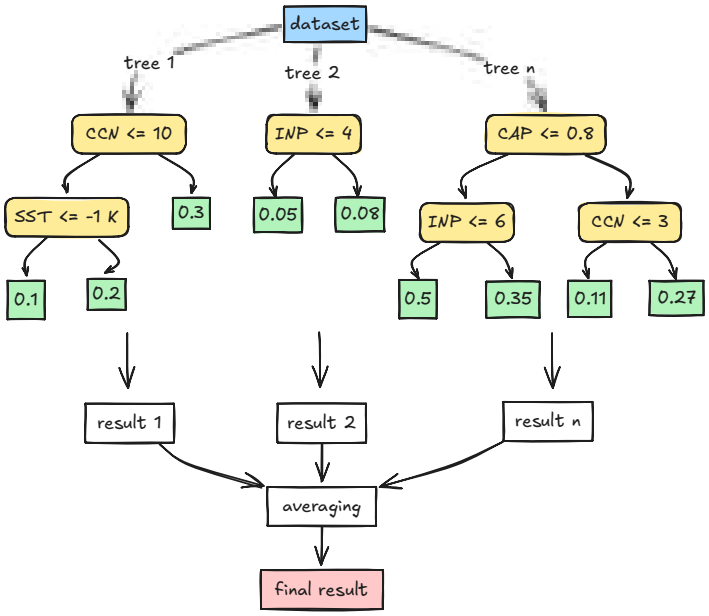

Figure 3.4: Example of random forest regression decision trees with arbitrary values and tree complexities. The internal nodes are colored yellow, whereas the leaf nodes are green. The final result in red represents the prediction of the model for one parameter combination. Diagram created with Excalidraw (`https://excalidraw.com`, last accessed: 01.12.2024).

variable, e.g., hydrometeor mass concentration, number concentration, or diabatic heating rate. Figure 3.4 visualizes the concept of decision trees with arbitrary values. A decision tree consists of logical rules, the so-called internal nodes (yellow), and results, the so-called leaf nodes (green). When growing a tree with a random subsample, a perturbed parameter is randomly chosen for every internal node to split the subsample according to a threshold value of this perturbed parameter. In Scikit-Learn, the default is that the tree is fully grown when every leaf node contains only one value.

After the N trees are grown, the RFR model is trained and can be validated with the validation dataset consisting of 20 perturbed parameter combinations. For this, the RFR model predicts the target variable by averaging the results of all decision trees. In Figure 3.4, the prediction for one parameter combination is depicted in red as the final result. To evaluate the model's performance, the predictions are compared with the output of the ICON model runs in scatter diagrams. In addition, RMSE and R^2 scores are calculated.

The RFR model performance can be improved by altering the hyperparameters of the model. Hyperparameters are parameters that are prescribed, and the algorithm does not learn them independently. Examples of hyperparameters are the number of decision trees N_{tree}, the number of features considered per internal node N_{feat}, and the minimum number of samples needed to split an internal node N_{s}. To determine the best hyperparameter combination for every model, hyperparameter tuning is performed using the Grid Search algorithm. This means that for every chosen hyperparameter, values are preselected, and every possible combination of hyperparameters is tested for each model. Subsequently, the combination yielding the smallest RMSE on the validation dataset is chosen for the respective model. The hyperparameter values tested are listed in Table 3.3. The range of

Table 3.3: Hyperparameter values used to determine the best combination via Grid Search. Tested are the number of decision trees N_{tree}, the minimum number of samples needed to split an internal node N_{s}, and the number of features considered per internal node N_{feat}.

N_{tree}	N_{feat}	N_{s}
100	1	2
150	2	3
200	3	4
250	4	5
500	5	

Table 3.4: Grid Search of the best hyperparameter combinations for the RFR models of the mean vertically integrated hydrometeor mass concentrations of cloud water ($q_{\text{c,t}}$), rain ($q_{\text{r,t}}$), ice ($q_{\text{i,t}}$), snow ($q_{\text{s,t}}$), graupel ($q_{\text{g,t}}$), and hail ($q_{\text{h,t}}$). The hyperparameters are the number of decision trees N_{tree}, the minimum number of samples needed to split an internal node N_{s}, and the number of features considered per internal node N_{feat}. Model performance is indicated by the root mean squared error (RMSE; in kg m^{-2}) and R^2 score.

$q_{\text{x,t}}$	N_{tree}	N_{s}	N_{feat}	RMSE	R^2
$q_{\text{c,t}}$	200	2	4	5.28×10^{-2}	0.905
$q_{\text{r,t}}$	150	3	4	5.03×10^{-3}	0.874
$q_{\text{i,t}}$	500	2	4	2.44×10^{-3}	0.828
$q_{\text{s,t}}$	500	3	5	1.18×10^{-2}	0.650
$q_{\text{g,t}}$	150	2	4	6.34×10^{-3}	0.949
$q_{\text{h,t}}$	100	2	5	3.80×10^{-4}	0.955

the number of trees is rather small because the sample size of the training and validation datasets is quite limited, so too many trees would lead to overfitting. Naturally, the number of features considered per internal node is limited by the total number of perturbed parameters. Since the datasets are small, N_{s} should not be too large, as too many samples needed to split an internal node would lead to imprecise predictions. The hyperparameter values of the RFR $q_{\text{x,t}}$ models after the Grid Search was performed are listed in Table 3.4 together with their RMSE and R^2 score.

3.5 Variance Decomposition

For quantifying the individual impacts of the N_{p} perturbed parameters on the cloud structure, variance decomposition is performed for several variables. According to Oakley and O'Hagan (2004), the total variance V of a target variable with N_{p} independent input parameters is decomposable into

$$V = \sum_{i=1}^{N_{\text{p}}} V_i + \sum_{i<j} V_{ij} + \ldots + V_{1,\ldots,p} \tag{3.1}$$

with the individual contributions V_i of the N_p perturbed parameters, contributions of two interacting parameters V_{ij} and the contribution of all parameters interacting with each other $V_{1,\ldots,p}$. The Fourier amplitude sensitivity test (FAST; Saltelli et al., 1999) is applied to do the decomposition, using the SALib Python library (Iwanaga et al., 2022; Herman and Usher, 2017). FAST offers a global sensitivity analysis which needs a large sample size of $\mathcal{O}(10^4)$. The generation of such a sample is explained in Section 3.4.2. Subsequently, the so-called first-order sensitivity index, or main effect,

$$S_i = \frac{V_i}{V} \tag{3.2}$$

is calculated. It describes the contribution of the perturbed parameter i to the target variable's variance, and therefore indicates by how much percent this variance could be reduced if the parameter i had no uncertainty (Wellmann et al., 2018).

4 Case Study

The WCB considered in this thesis is associated with a cyclone in the North Atlantic occurring at the beginning of October 2016 during the North Atlantic Waveguide and Downstream Impact Experiment (NAWDEX) campaign (intensive observation period (IOP) 7; Schäfler et al. (2018)). According to Oertel et al. (2023), on October 2, 2016 a weak sea level pressure depression initially forms east of 60 °W at around 45 °N in a strong baroclinic zone (Oertel et al., 2023). The resulting surface cyclone occurs in conjunction with a local positive low-level PV anomaly, which travels along this baroclinic zone over the North Atlantic and features traits of a diabatic Rossby wave (Boettcher and Wernli, 2013). On the following day, the cyclone intensifies further, interacts with the nearing upper-level trough, and exhibits a distinguishable cold and warm front (Oertel et al., 2023). Besides, an extensive cloud band is established, which is linked to the northward WCB ascent, and the cyclone moves poleward in front of the upper-level trough.

From October 4th to October 5th, the WCB ascent is strongest, and a vast, large-scale cloud band is formed. That is why this period is the focus of this thesis. To investigate the evolution of the WCB, three time steps are chosen, namely 12 and 18 UTC on October 4th and 0 UTC on October 5th. Figure 4.1 depicts the temperature field in 850 hPa (a-c) and the total water path (TWP, d-f) of the unperturbed reference simulation (REF) for those time steps. On 4 October at 12 UTC, the center of the cyclone is located at 32 °W, 52 °N and the poleward WCB ascent mainly takes place in the warm sector of the cyclone, in front of the surface cold front and upper-level trough (red contour), between 40 °N-50 °N and 30 °W-40 °W (Fig. 4.1a). However, the WCB ascent also occurs in proximity to the center of the cyclone (Oertel et al., 2023). Figure 4.1d shows the total water path (TWP) of the widespread cloud shield, which forms due to rising air parcels. It starts south of the cold front, covers the warm sector, and curls cyclonically around the center of the cyclone but does not encircle it entirely.

In the next six hours, the center of the cyclone and upper-level ridge move northward (Fig. 4.1b). Besides, the amount of cloud band parts with high TWP decreases and the cloud band moves northward and eastward (Fig. 4.1e). Another six hours later, the system has traveled even closer to the pole (Fig. 4.1c,f). Furthermore, the northern cloud component stretches further west and curls around the center of the cyclone, whereas the cloud band becomes thinner in general.

To gain an understanding of the vertical WCB cloud structure, two vertical cross-sections of the total hydrometeor mass concentration q_t are placed through the WCB ascent region ahead of the cold front (Fig. 4.2). Both panels include contours of the five different hydrometeor classes (cloud water, rain, ice, snow, and graupel, which also contains hail), isentropes, and isotherms of REF. For Fig. 4.2a, the latitude of 49 °N is chosen for the 4th of October at 12 UTC as an example of an

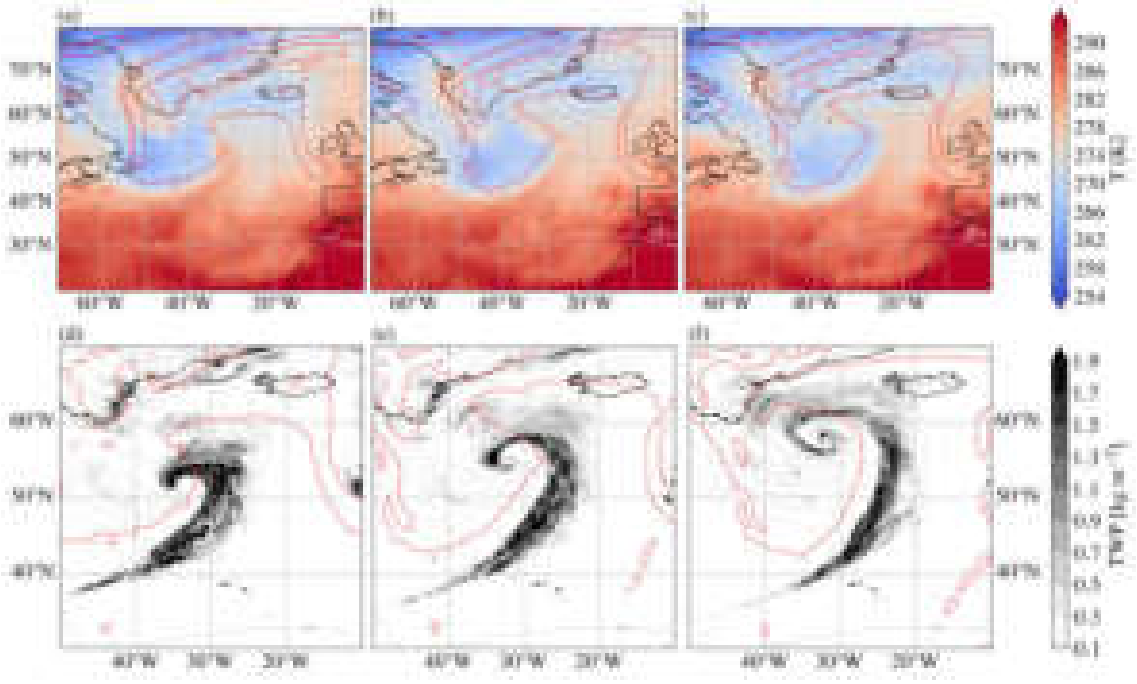

Figure 4.1: **(a)-(c)** Temperature at 850 hPa (T, in K; shading) and **(d)-(f)** total water path (TWP, in $\mathrm{kg\,m^{-2}}$; shading) for **(a), (d)** 12 UTC on October 4th, **(b), (e)** 18 UTC on October 4th, and **(c), (f)** 0 UTC on October 5th. In all panels, grey contours correspond to mean sea level pressure in 5 hPa intervals and red contours to 2 PVU line at 300 hPa. All panels show the unperturbed reference simulation (REF) data.

instantaneous cross-section. In contrast, cross-section composites averaged over the 4th and 5th of October are illustrated in Fig. 4.2b. One difference is that the isentropes and isotherms of the composites are smoother than the ones of the instantaneous cross-section, because of the averaging over cross-sections of several latitudes and time steps. Especially, the cold front in Fig. 4.2a is more sharply pronounced by the step-like form of the 273 K isotherm at 34 °W.

Overall, the height at which the various hydrometeor types can be found is similar. In both panels, raindrops reach from the ground up to 3 km and cloud droplets are present mainly between 1 km and 6 km. Graupel appears mainly between 2 km and 4 km, but the upper limit can be higher as seen in Fig. 4.2a. Snow spreads between 2 km and 8 km in the composites and is shifted 1 km upward in the instantaneous view. The lower boundary of ice is also 1 km lower in the composites at 3 km, and the upper boundary is above 10 km. In Fig. 4.2a, ice can still be found at 12 km altitude.

Furthermore, the individual horizontal hydrometeor distributions differ considerably between the two panels. Although the contours in Fig. 4.2b suggest that each hydrometeor class occurs coherently as one cluster, except for the small additional cloud and raindrop clusters, Fig. 4.2a demonstrates the opposite. In this depiction, there is not a single hydrometeor type with only one cluster. Raindrops are divided into two large areas between 32 °W and 27 °W and a narrow vertical band at 26 °W composed of several smaller clusters. Cloud droplets tend to form short, slim clusters higher up instead of a huge cluster spreading over several longitudes. Moreover, graupel is separated into three narrow groups located at 32 °W, 30.5 °W, and 26 °W. The snow distribution is characterized by four large parts and one minuscule part. Ice exhibits the biggest coherent cluster,

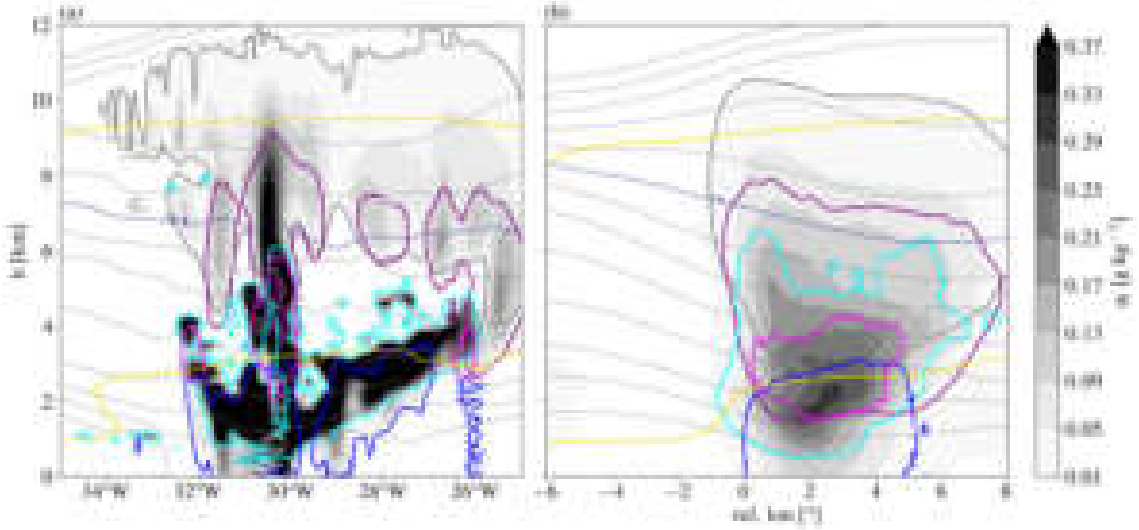

Figure 4.2: Total hydrometeor mass concentration (q_t, shading) with cloud water (q_c, cyan contours at 0.02 g/kg), rain (q_r, blue contours at 0.02 g/kg), snow (q_s, purple contours at 0.01 g/kg), ice (q_i, grey contours at 0.01 g/kg), and graupel (q_g, magenta contours at 0.02 g/kg) mass concentration; 273 and 233 K isotherms (gold); 320 K isentrope (blue), and potential temperature (5 K intervals, grey lines) for **(a)** vertical cross-section through the WCB at 49 °N at 12 UTC on October 4, 2016; and **(b)** vertical cross-section composites through the WCB ascent region in front of the cold front averaged over the 4th and 5th of October 2016. Both panels show the unperturbed reference simulation (REF) data.

with only a few additional tiny ones. Besides, between 30 °W-26 °W and 4 km-6 km, there are few to none hydrometeors of any kind. Lastly, it should be pointed out that the low-level total hydrometeor mass concentration of the instantaneous cross-section is significantly higher due to the amount of cloud droplets. Additionally, the high q_t values are spread more widely.

5 Qualitative Parameter Impacts

In this Chapter, the results of the WCB simulations are presented. First, the unperturbed reference simulation is compared to the PPE simulations (Section 5.1). Second, more detailed analyses of the individual parameter perturbations are shown, starting with the impacts of CCNs (Section 5.2), followed by the impacts of INPs (Section 5.3), CAP (Section 5.4), and SST together with SAT (Section 5.5).

5.1 Unperturbed versus Perturbed Simulations

First, a brief description of the REF cloud structure in the Eulerian perspective is provided before comparing it with the PPE simulations. Figure 5.1 shows vertical profiles of different mean hydrometeor mass concentrations (first column) and mean number concentrations (second column) in the Eulerian perspective, as well as mean hydrometeor mass concentrations (third column) in the Lagrangian perspective. The REF is marked in red and the PPE members are colored grey. The warm phase of the REF cloud, where temperatures higher than the 273 K melting level occur, is located below 3 km in the Eulerian perspective. Within this phase, the maximum rain mass concentration is observed at 1 km (Fig. 5.1e) and the maximum cloud water mass concentration at 2 km (Fig. 5.1b). Furthermore, the mixed-phase region, which spans temperatures between 273 K and 235 K, extends approximately from 3 km to 9 km. Small amounts of rain mass concentration q_r and cloud water mass concentration q_c occur there as well. High graupel mass concentrations q_g are predominantly found in lower parts of the mixed-phase region near the melting level (Fig. 5.1n), whereas snow occurs throughout the whole mixed-phase region and the snow mass concentration q_s peaks directly above the peak of the graupel mass concentration (compare Fig. 5.1k, 5.1n). Lastly, ice mass concentrations q_i reach from the melting level up to 12 km but mainly occur around 7 km in the upper parts of the mixed-phase region (Fig. 5.1h).

When model parameter perturbations are introduced, two main impacts on the cloud structure are observed. First, a substantial variability is caused as the PPE members spread the hydrometeor mass and number concentrations. Second, the maxima of some hydrometeor mass concentrations are vertically displaced. In addition to that, despite the considerable spread, no PPE member appears to be unphysical. In the following, these impacts will be examined in more detail.

Except for two PPE members, the maximum of q_c increases and is shifted upward compared to REF in the Eulerian perspective (Fig. 5.1b). To be precise, the maximum of $0.07\,\mathrm{g\,kg^{-1}}$ in REF moves from 2 km in the warm phase to almost 4 km in the mixed phase in PPE and is up to five times

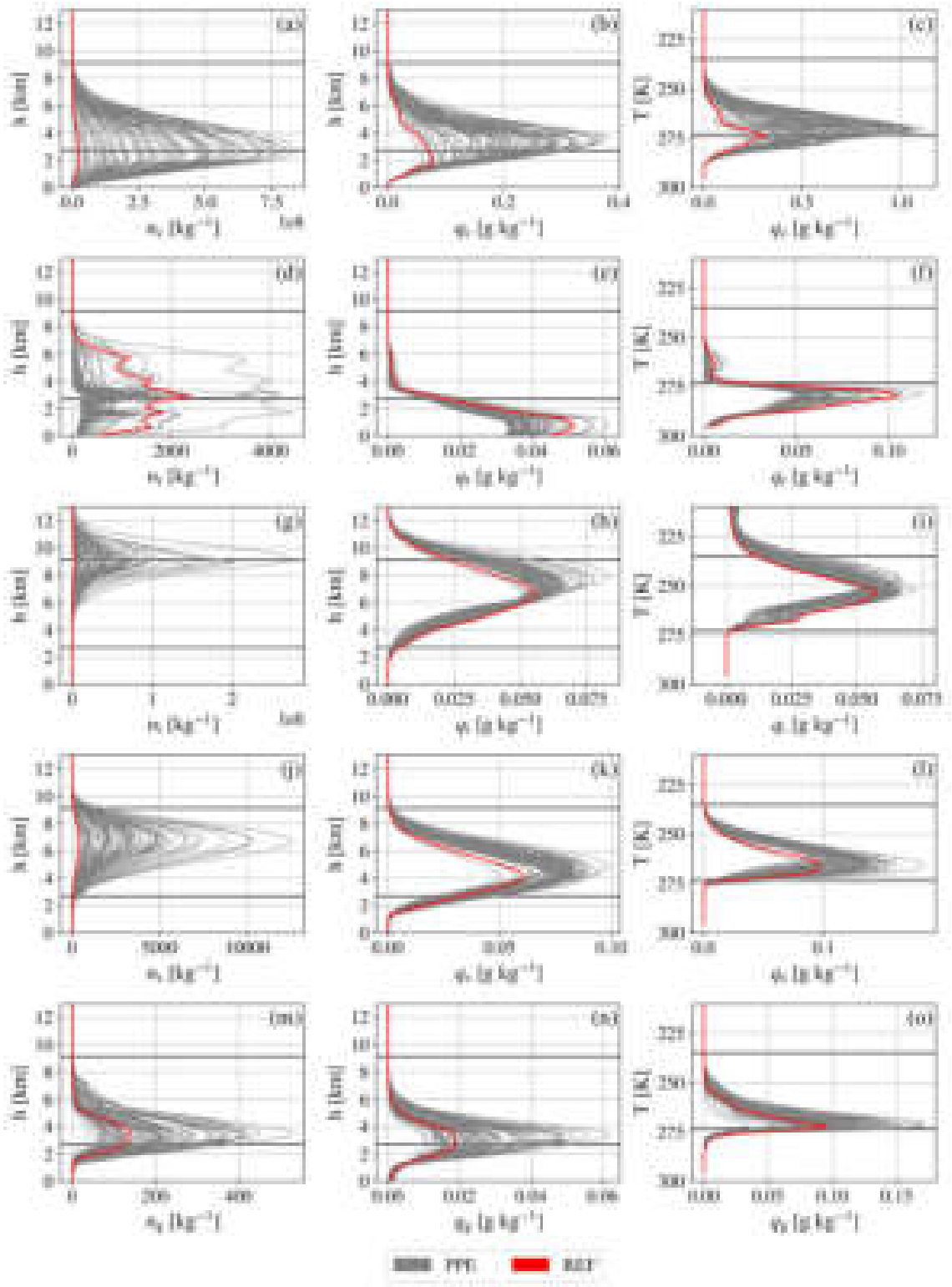

Figure 5.1: WCB cloud characteristics from Eulerian and Lagrangian perspectives. First column shows vertical profiles of mean number concentrations averaged over the WCB cloud band (i.e., $0-8°$ rel. lon in the respective vertical cross-section composite) for **(a)** cloud water (n_c, in kg^{-1}), **(d)** rain (n_r), **(g)** ice (n_i), **(j)** snow (n_s), and **(m)** graupel (n_g). Individual PPE members are shown in grey, the unperturbed reference simulation (REF) is shown in red. Second column as first column but for mean hydrometeor mass concentrations (q_x, in $g\,kg^{-1}$). The third column shows mean hydrometeor mass concentrations along the online WCB trajectories. Hydrometeor mass concentrations are averaged over 2 K bins along the ascent for all WCB trajectories of each PPE member (grey) and REF (red), respectively. Altitudes of the melting level at 273 K and the homogeneous ice nucleation level at 235 K of REF are marked as black horizontal lines.

larger, alsmost reaching $0.4\,\mathrm{g\,kg^{-1}}$. As expected, the increase in cloud water mass concentration is also reflected in the front relative cross-section composites of the vertically integrated cloud water mass concentration $q_{\mathrm{c,t}}$ (Fig. 5.2b) because q_{c} increases at all levels. In contrast to q_{c}, q_{r} has the fourth-largest maximum in REF with approximately $0.05\,\mathrm{g\,kg^{-1}}$ and the maximum appears to occur in all PPE members at 1 km (Fig. 5.1e). Correspondingly, the vertically integrated rain mass concentration $q_{\mathrm{r,t}}$ decreases in most PPE members (Fig. 5.2d). The maximum q_{i} of REF amounts to almost $0.06\,\mathrm{g\,kg^{-1}}$ and is located slightly below 7 km, which is lower than almost every PPE member (Fig. 5.1h). Besides, the maximum value of q_{i} is increased in the majority of the PPE members, reaching up to $0.08\,\mathrm{g\,kg^{-1}}$. It should also be noted that in the PPE, q_{i} is displaced upward in its entirety. Figure 5.2f shows, however, that the vertically integrated ice mass concentration $q_{\mathrm{i,t}}$ of REF is in the middle of the PPE members in the warm sector close to the front. Further east of the front, $q_{\mathrm{i,t}}$ is for most PPE members higher than in REF. Similarly to q_{i}, the maximum q_{s} increases in all but two PPE members compared to REF and an upward shift is observed as well (Fig. 5.1k). In REF, the maximum q_{s} is $0.06\,\mathrm{g\,kg^{-1}}$ at 4 km and can exceed $0.08\,\mathrm{g\,kg^{-1}}$ for some PPE members. The vertically integrated snow mass concentration $q_{\mathrm{s,t}}$ increases mostly as well in the PPE (Fig. 5.2h). Since the observed hail mass concentrations are rather small and hail is defined as graupel that exceeds a diameter of 5 mm, hail is from now on included in the graupel mass concentration q_{g}. The same applies to the respective number concentration n_{g}. Figure 5.1n shows that the q_{g} maximum of $0.02\,\mathrm{g\,kg^{-1}}$ in REF is in the lower third of the PPE maxima and is located at 3 km. Consequently, the vertically integrated graupel mass concentration q_{g} also increases for most of the PPE members (Fig. 5.2j).

Looking at the hydrometeor number concentrations reveals a similar trend. The cloud droplet number concentration n_{c} increases immensely due to parameter perturbations (Fig. 5.1a), just like the vertically integrated cloud droplet number concentration $n_{\mathrm{c,t}}$ (Fig. 5.2a). The maximum n_{c} can be over 16 times larger than REF, depending on the PPE member, and peaks around the melting level. Only a few members reach values of $8\times10^{8}\,\mathrm{kg^{-1}}$ for n_{c}, and most remain below $4\times10^{8}\,\mathrm{kg^{-1}}$. The raindrop number concentration n_{r}, on the other hand, is in REF overall rather large compared to PPE members, except for one PPE member which is approximately twice as large as REF and is probably an outlier (Fig. 5.1d). Most of the PPE members tend to peak below 2 km and around 3 km above the melting level. REF has a maximum n_{r} of roughly $2000\,\mathrm{kg^{-1}}$ around 3 km. In Fig. 5.2c, the vertically integrated rain number concentration $n_{\mathrm{r,t}}$ exhibits the PPE outlier and a decrease for the majority of the PPE members, as well. On the contrary, number concentrations of ice n_{i} and snow n_{s} can be up to a few orders of magnitude higher, when the parameters are perturbed, than in REF (Fig. 5.1g,j). The same applies to the vertically integrated number concentrations $n_{\mathrm{i,t}}$ and $n_{\mathrm{s,t}}$ (Fig. 5.2e,g). n_{i} peaks at 9 km and does not exceed $1\times10^{6}\,\mathrm{kg^{-1}}$ for most members, whereas n_{s} peaks near 7 km and is typically smaller than $6000\,\mathrm{kg^{-1}}$. Lastly, n_{g} appears to have the same structure as q_{g}, meaning that REF lies in the lower third of the PPE spread, having a n_{g} maximum of approximately $130\,\mathrm{kg^{-1}}$ (Fig. 5.1m). In REF, the vertically integrated graupel number concentration $n_{\mathrm{g,t}}$is in the middle of the PPE members (Fig. 5.2i).

For the Lagrangian perspective, the trajectory data are binned in temperature bins (T-bins; Section 3.3.2). This allows for a comprehensive process-based perspective. In this comparison between

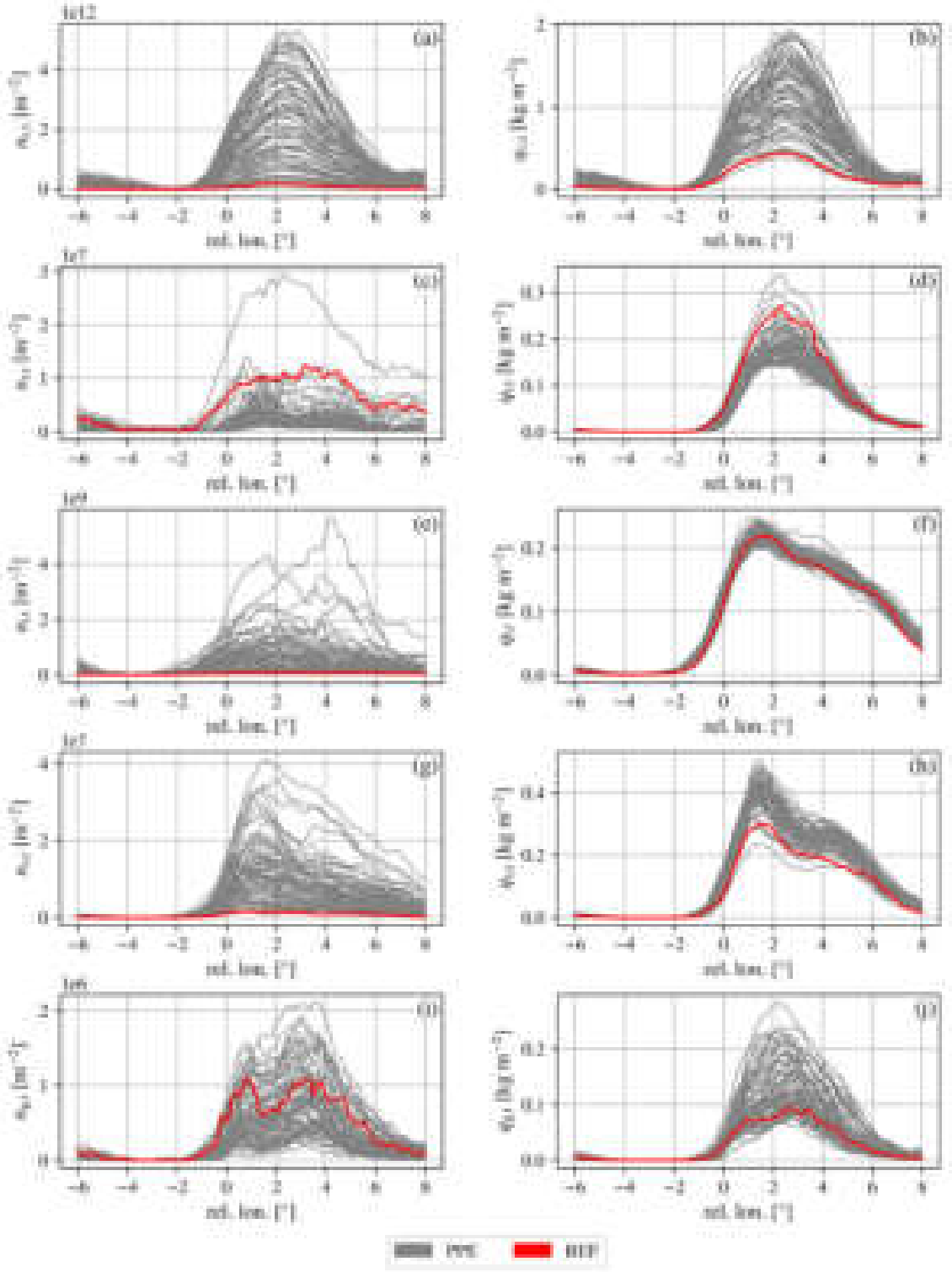

Figure 5.2: Front relative cross-section composites of vertically integrated number concentrations (first column) for **(a)** cloud water ($n_{c,t}$, in m^{-2}), **(c)** rain ($n_{r,t}$), **(e)** ice ($n_{i,t}$), **(g)** snow ($n_{s,t}$), and **(i)** graupel ($n_{g,t}$) and vertically integrated hydrometeor mass concentrations ($q_{x,t}$, in $g\,kg^{-1}$; **(b), (d), (f), (h), (j)**) for the unperturbed reference simulation (REF; red) and all PPE members (grey).

REF and PPE, the Lagrangian perspective is only applied to the hydrometeor mass concentrations (Fig. 5.1 third column), since hydrometeor number concentrations are not available in REF and rain and graupel number concentrations are also not available in the PPE. Qualitatively, the hydrometeor mass concentrations agree in the Eulerian and Lagrangian perspectives when comparing REF and PPE. The maximum mean cloud water mass concentration of $0.3\,\mathrm{g\,kg^{-1}}$ is located at the melting level in REF (Fig. 5.1c). It increases and shifts up to 4 K to lower temperatures in most PPE members. For some PPE members, the maximum of q_c exceeds $1\,\mathrm{g\,kg^{-1}}$. Cloud water is observed between 290 K and 240 K. On the other hand, q_r has a maximum of approximately $0.1\,\mathrm{g\,kg^{-1}}$ below the melting level at 280 K in REF (Fig. 5.1f). In the PPE, the maximum q_r decreases to $0.05\,\mathrm{g\,kg^{-1}}$ but stays in the same temperature range. For temperatures lower than 273 K, q_r strongly decreases as raindrops begin to freeze. The maximum mean ice mass concentration is located below 250 K for all simulation runs and amounts to approximately $0.06\,\mathrm{g\,kg^{-1}}$ (Fig. 5.1i). As expected, q_i occurs mainly at temperatures lower than 273 K and reaches up to 220 K. Below 260 K, q_i is largest in REF compared to the other PPE members and smallest above 250 K. Thus, the q_i maximum is shifted to lower temperature in most of the PPE members, which is consistent with the Eulerian perspective. Furthermore, snow is observed mainly between 273 K and 235 K (Fig. 5.1l). REF has a maximum q_s of almost $0.1\,\mathrm{g\,kg^{-1}}$ at around 265 K. The PPE exhibits an increase in q_s, with some members exceeding $0.15\,\mathrm{g\,kg^{-1}}$. Like q_c, the graupel mass concentration peaks at the melting level (Fig. 5.1o). It occurs mainly in the mixed-phase region, where q_c and q_s coincide, and the highest amounts are found in a temperature range of 275 K to 260 K. In the warm phase, q_g quickly decreases with increasing temperature as graupel melts. The REF has a maximum q_g of almost $0.1\,\mathrm{g\,kg^{-1}}$, whereas the PPE maxima spread around this value with a tendency to higher values.

In the following, the main findings presented in this Section are summarized. In summary, the parameter perturbations lead to considerable variability in hydrometeor mass and number concentrations. More specifically, the mass and number concentration of cloud water, ice, snow, and graupel increase mainly due to the perturbations, whereas the rain mass and number concentration generally decrease. These asymmetric effects probably originate from the asymmetric perturbations compared to REF. The same also applies to the vertically integrated hydrometeor mass concentrations and number concentrations.

5.2 Cloud Condensation Nucleus Impacts

To analyze the impact of varying CCN concentrations, cloud water mass and number concentrations are examined first. By increasing the CCN concentration, q_c and n_c increase both in the Eulerian (Fig. 5.3a,b) and Lagrangian perspective (Fig. 5.3d,e) consistently at all height and temperature levels. Therefore, $q_\mathrm{c,t}$ and $n_\mathrm{c,t}$ are strongly influenced throughout the warm sector (Fig. 5.3g,h) and increase as well. Besides, the differences between the three subsets are relatively large. The increases in q_c and n_c result from the fact that the different CCN concentrations are considered by systematically perturbing the number of activated cloud droplets, which is reflected in the diabatic heating rate of cloud droplet activation QCNUC (Fig. 5.3c,f). As expected, when more cloud droplets are activated, their number concentration increases as a result. Subsequently, the average

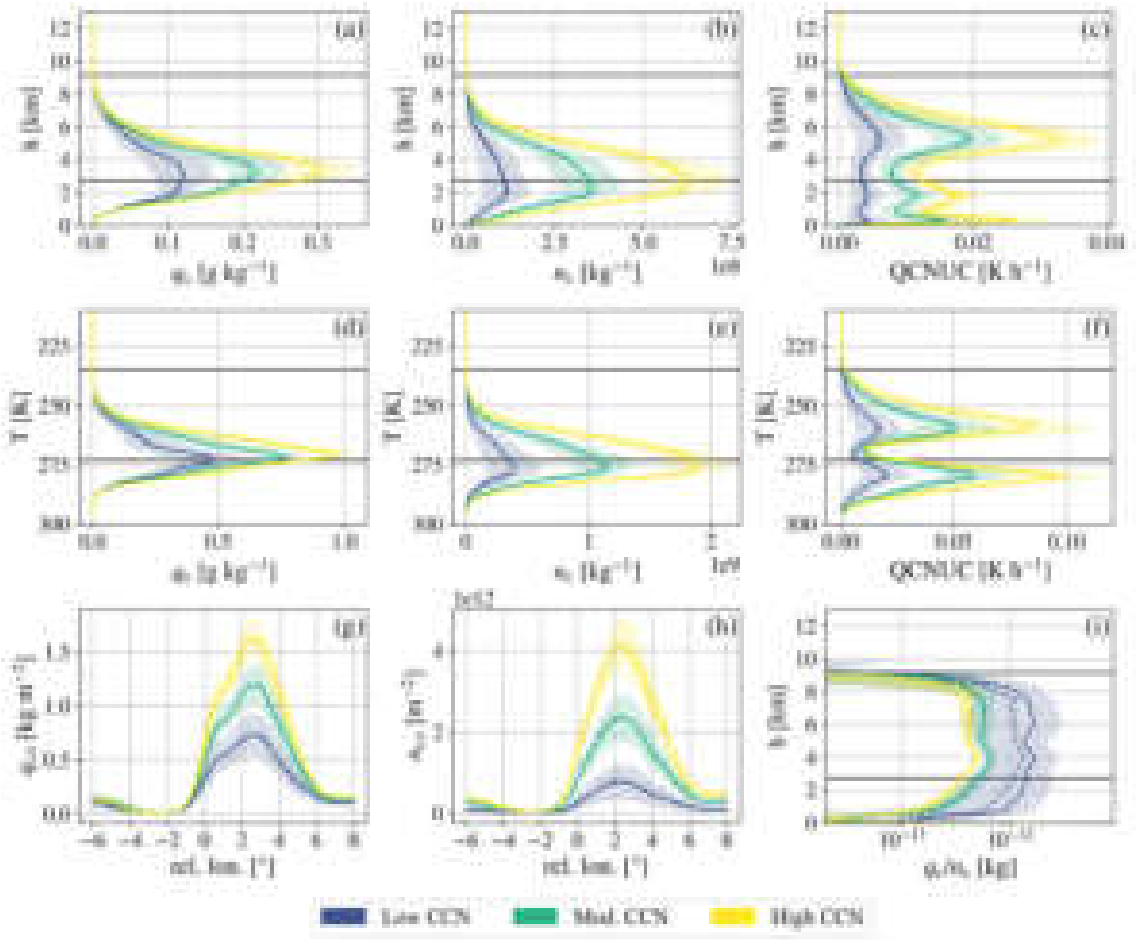

Figure 5.3: Influence of cloud condensation nucleus (CCN) perturbations on WCB cloud characteristics from Eulerian and Lagrangian perspectives. Shown are the median (dashed), average (solid), and standard deviation (shading) for three distinct subsets of the PPE, which are stratified in low (blue), moderate (green), and high (yellow) CCN perturbations (Table A.1). **(a), (b), (c),(i)** Vertical profiles are averaged over the WCB cloud (i.e., $0-8°$ rel. lon. in the respective vertical cross-section composite) for **(a)** cloud water mass concentration (q_c, in $\mathrm{g\,kg^{-1}}$), **(b)** cloud droplet number concentration (n_c, in $\mathrm{kg^{-1}}$), **(c)** diabatic heating rate of cloud droplet activation (QCNUC, in $\mathrm{K\,h^{-1}}$), and **(i)** mean cloud droplet mass (q_c/n_c, in kg). **(d-f)** as **(a-c)** but averaged in temperature bins along ascending WCB trajectories. The altitudes of the melting level at 273 K and the homogeneous ice nucleation level at 235 K of the unperturbed reference simulation REF are marked as black horizontal lines. **(g)** Vertically integrated cloud water mass concentration ($q_{c,t}$, in $\mathrm{kg\,m^{-2}}$) and **(h)** vertically integrated cloud droplet number concentration ($n_{c,t}$, in $\mathrm{m^{-2}}$) along the WCB cloud.

cloud droplet mass q_c/n_c decreases (Fig. 5.3i) as the droplets compete for water vapor. However, q_c increases (Fig. 5.3a,e), even though the average droplet is smaller and lighter. More specifically, the conversion of q_c to q_r is reduced by the smaller mean cloud droplet mass, which appears to outweigh the higher n_c causing a lower collision efficiency, as, e.g., shown in Barthlott et al. (2022) for a convective cloud. Because the conversion of q_c to q_r is reduced, q_c increases.

This is directly related to a reduction in q_r for higher CCN concentrations in the warm phase in both perspectives (Fig. 5.4a,c), which affects $q_{r,t}$ in the same way (Fig. 5.4d). Furthermore, n_r is generally lower for higher CCN concentrations in the Eulerian perspective (Fig. 5.4b). Yet, a clear, systematic relation is not observable, since the highest CCN concentrations do not yield

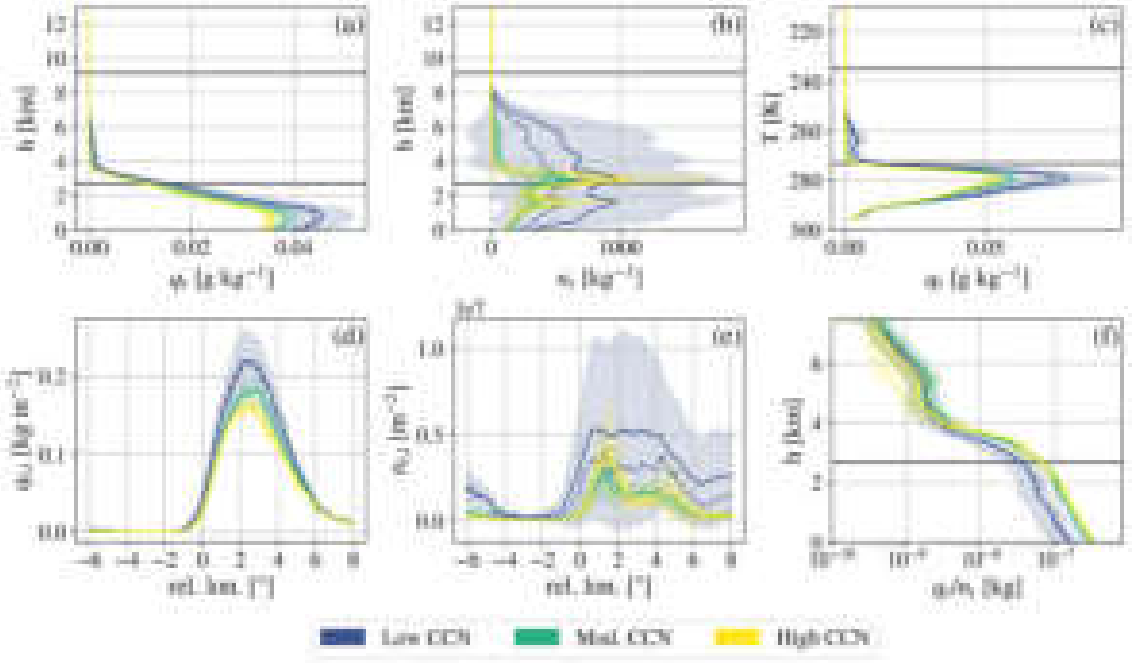

Figure 5.4: As Fig. 5.3 but for **(a)**, **(c)** rain mass concentration (q_r, in $g\,kg^{-1}$), **(b)** raindrop number concentration (n_r, in kg^{-1}), **(d)** vertically integrated rain mass concentration ($q_{r,t}$, in $kg\,m^{-2}$), **(e)** vertically integrated raindrop number concentration ($n_{r,t}$, in m^{-2}), and **(f)** mean raindrop mass (q_r/n_r, in kg)

the lowest n_r. In addition, the mean n_r of the subset with the lowest CCN concentrations differs strongly from its median, indicating the influence of the outlier seen in Fig. 5.2d. This is also reflected in $n_{r,t}$ (Fig. 5.4e). In contrast to q_c/n_c, the mean raindrop mass q_r/n_r is not as much and as systematically influenced by CCN perturbations above 4 km (Fig. 5.4f). Moderate CCN concentrations appear to yield the largest q_r/n_r, whereas the highest CCN concentrations produce the lowest q_r/n_r. Below 4 km, q_r/n_r is larger for higher CCN concentrations. This could be because with fewer raindrops, there is less competition for additional droplets, allowing individual raindrops to grow larger through collision-coalescence processes.

The increase in CCN concentration also affects q_s (Fig. 5.5a,d) and $q_{s,t}$ (Fig. 5.5g). In both perspectives, the maxima of the subsets with moderate and high CCN concentrations increase and are almost identical. Their increase is related to the higher depositional growth rate of snow QSDEP (Fig. 5.5b,e), which may be an indication of a stronger WBF process. As more water vapor deposits on snow, more cloud droplets potentially need to evaporate to provide this water vapor and remove subsaturation w.r.t. liquid. This increased evaporation of cloud water is indicated by the stronger negative heating rate of the second saturation adjustment (SATAD2) for higher CCN concentrations between 4 km and 5.5 km and between 265 K and 250 K (Fig. 5.5c,d). More evaporation can occur because higher CCN concentrations lead to more cloud water.

Furthermore, the mass and number concentrations of graupel are reduced for higher CCN concentrations. For q_g this occurs between 2 km and 5 km (Fig. 5.6a) and between 263 K and 273 K (Fig. 5.6c), whereas n_g is reduced between 2 km and 5 km (Fig. 5.6b). However, this relation is not as systematic as it is with q_c and n_c, which is indicated by the overlap of the standard deviations

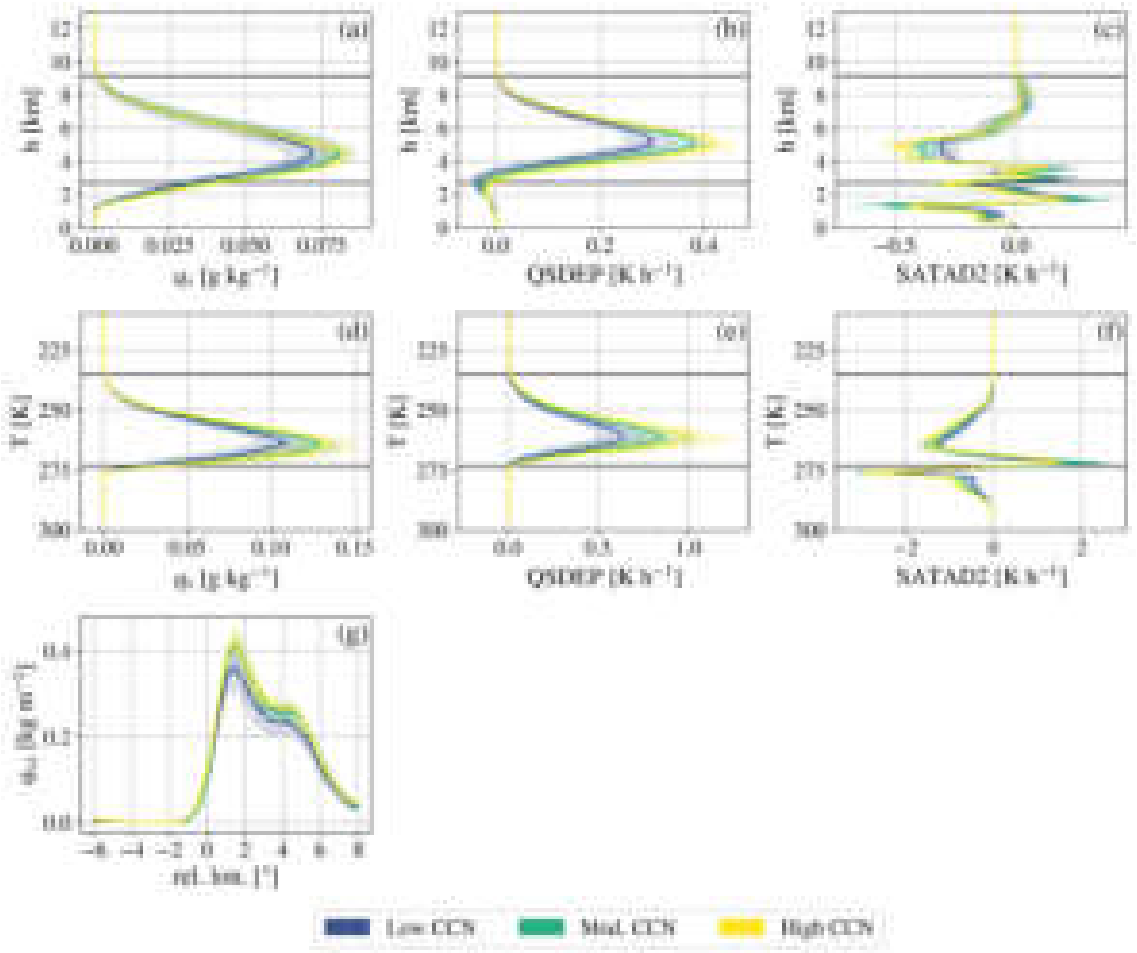

Figure 5.5: As Fig. 5.3 but for **(a)**, **(d)** snow mass concentration (q_s, in $g\,kg^{-1}$), **(b)**, **(e)** diabatic heating rate of depositional growth of snow (QSDEP, in $K\,h^{-1}$), **(c)**, **(f)** diabatic heating rate of the second saturation adjustment (SATAD2, in $K\,h^{-1}$), **(d)** vertically integrated raindrop number concentration ($n_{r,t}$, in m^{-2}), and **(g)** vertically integrated snow mass concentration ($q_{s,t}$, in $kg\,m^{-2}$).

(shading) of the subsets. Nevertheless, the overall decrease of q_g and n_g is reflected in $q_{g,t}$ and $n_{g,t}$ (Fig. 5.6d,e). It occurs due to a decrease in the riming process QXRIM between 1 km and 5 km (Fig. 5.6g) and between 260 K and 275 K (Fig. 5.6h). Figure 5.6h shows that for higher CCN concentrations, the maximum of QXRIM occurs at slightly lower temperatures. The riming efficiency, like the efficiency of any other collision process, depends on the number and size of the collision partners. In this case, the smaller mean cloud droplet size dominates the higher n_c leading to fewer collisions of cloud droplets with ice, snow, and graupel, resulting in the observed reduction in riming. That way, less graupel is formed, and the one that is formed is, in fact, slightly larger but cannot grow as much through additional collisions to increase q_g.

For ice and snow, no substantial sensitivities are observed to changes in CCN concentration. Yet, liquid fraction (Fig. 5.7a,b), vertically integrated total hydrometeor mass concentration $q_{t,t}$ (Fig. 5.7d), and vertically integrated total number concentration $n_{t,t}$ (Fig. 5.7e) are clearly influenced by varying CCN concentrations. The increases in the liquid fraction and $q_{t,t}$ in the lower mixed-phase region are caused by a strong increase in $q_{c,t}$ with increasing CCN concentration (Fig. 5.3g), whereas the liquid fraction is also increased to a lesser extent by the decrease in $q_{g,t}$ (Fig. 5.6d).

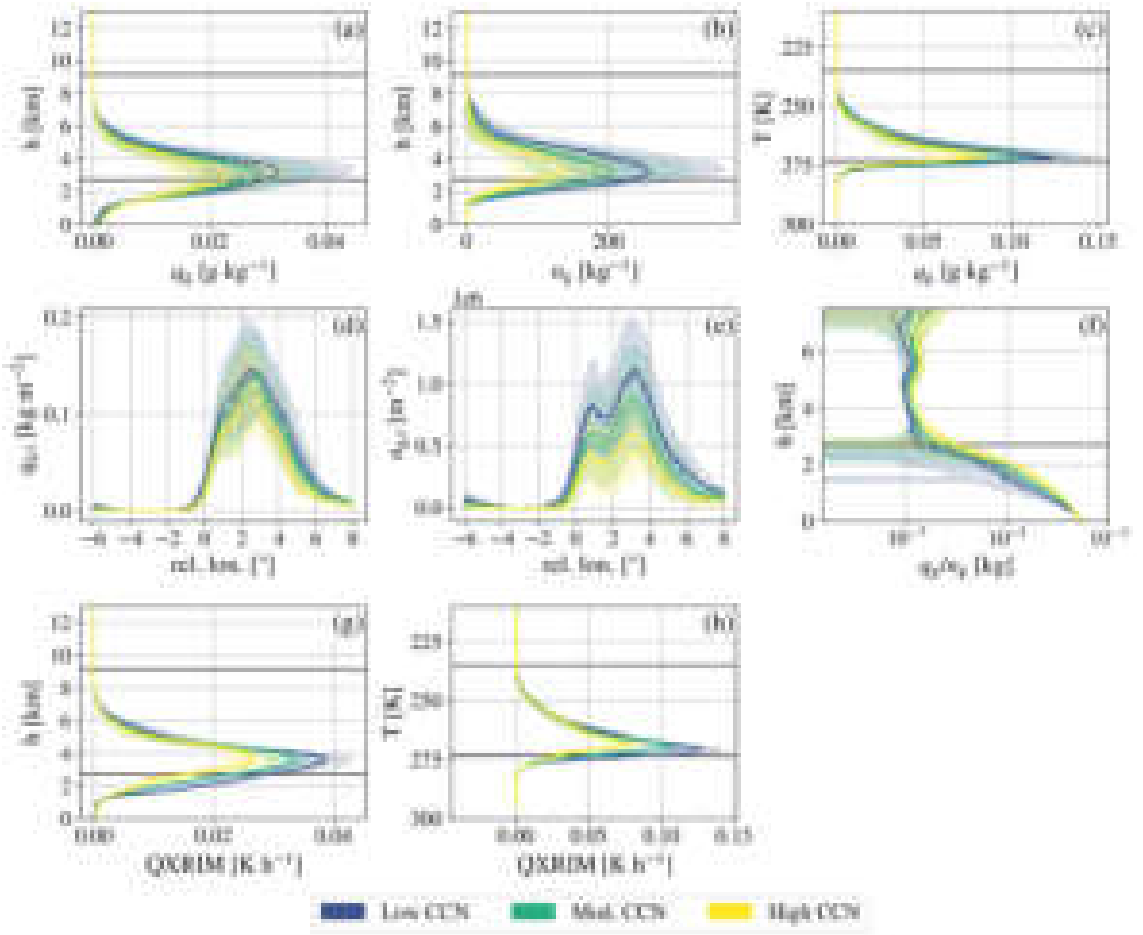

Figure 5.6: As Fig. 5.3 but for **(a)**, **(d)** graupel mass concentration (q_g, in $g\,kg^{-1}$), **(b)** graupel number concentration (n_g, in kg^{-1}), **(d)** vertically integrated graupel mass concentration ($q_{g,t}$, in $kg\,m^{-2}$), **(e)** vertically integrated graupel number concentration ($n_{g,t}$, in m^{-2}), **(f)** mean graupel mass (q_g/n_g, in kg), and **(g)**, **(h)** diabatic heating rate of riming (QXRIM, in $K\,h^{-1}$).

On the other hand, reduced $q_{g,t}$ negatively affects $q_{t,t}$, but this influence is so small since $q_{c,t}$ is one order of magnitude larger than $q_{g,t}$. In the same way, $n_{t,t}$ is predominantly influenced by $n_{c,t}$ (Fig. 5.3h) instead of $n_{g,t}$ (Fig. 5.6e). Thus, in general, increasing the CCN concentration increases the vertically integrated total hydrometeor number and mass concentration while adding more liquid water to the lower part of the mixed-phase region. In addition, the net shortwave radiation at TOA SW is reduced between 2° and 5° rel. lon. for moderate and high CCN concentrations (Fig. 5.7c). This may occur due to more reflection of incoming shortwave solar radiation caused by a higher cloud optical depth related to the increase in $n_{t,t}$.

To sum up, the main impacts of increased CCN concentrations on the WCB cloud structure are a strong increase in q_c and n_c at all levels, which is consistent in the Eulerian and Lagrangian perspectives, as well as an increase in $q_{c,t}$ and $n_{c,t}$ for all relative longitudes of the warm sector. Furthermore, a reduction in the mean cloud droplet size is observed, and in connection with that, a reduction in the maxima of q_r, $q_{r,t}$, q_g, $q_{g,t}$, $n_{g,t}$ and n_g. In contrast, the maximum of q_s and $q_{s,t}$ increases probably due to a stronger WBF process. Besides, the lower levels of the mixed-phase region contain more liquid water. Overall, the vertically integrated total hydrometeor mass and

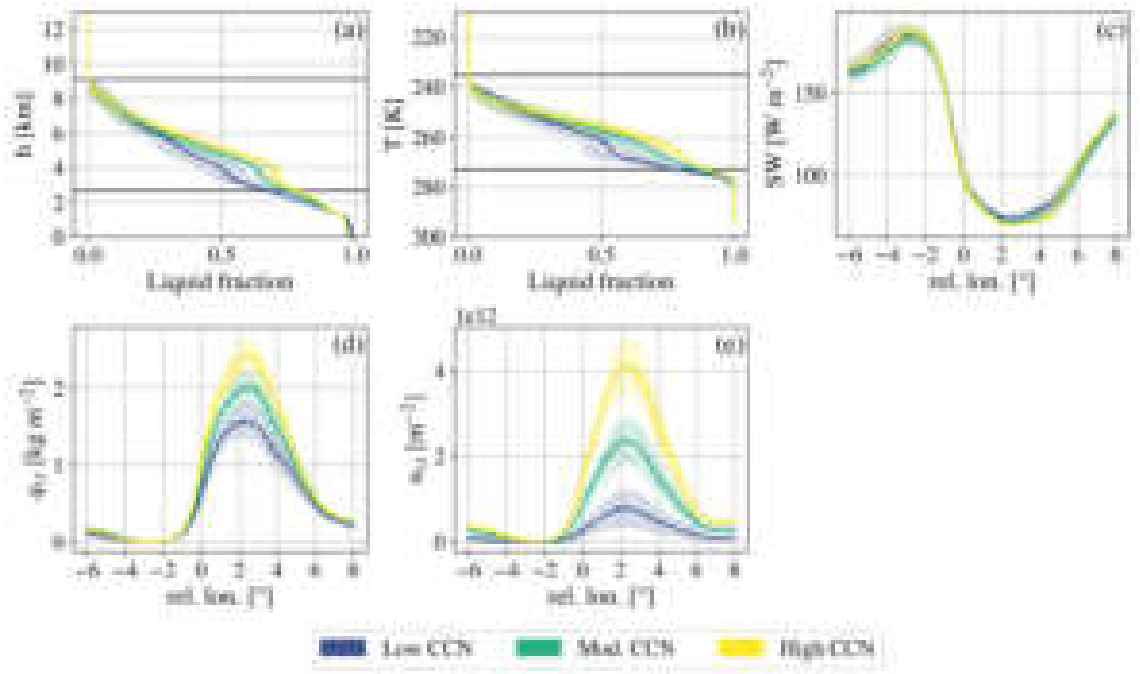

Figure 5.7: As Fig. 5.3 but for **(a)**, **(b)** liquid fraction, **(c)** net shortwave radiation at TOA (SW, in $\mathrm{W\,m^{-2}}$), **(d)** vertically integrated total hydrometeor mass concentration ($q_{\mathrm{t,t}}$, in $\mathrm{kg\,m^{-2}}$), and **(e)** vertically integrated total hydrometeor number concentration ($n_{\mathrm{t,t}}$, in $\mathrm{m^{-2}}$).

number concentration are increased in the warm sector, and the net shortwave radiation at TOA is reduced between 2° and 5° rel. lon.

5.3 Ice Nucleating Particle Impacts

The influence of INP perturbations on the WCB cloud structure is relatively small, especially compared to CCN perturbations. INP concentrations mainly affect the ice number concentration and, to a lesser extent, the ice mass concentration. For higher INP concentrations, the maximum of the median q_{i} increases slightly and its altitude shifts a few hundred meters downward (Fig. 5.8a). In the Lagrangian perspective, the subset maxima of the median q_{i} equal the subset maxima of the mean q_{i} (Fig. 5.8b). Besides, the maxima also increase consistently and occur at higher temperatures for high INP concentrations. However, the subset differences are small and $q_{\mathrm{i,t}}$ is only slightly reduced near the cold front for lower INP concentrations (Fig. 5.8c).

Contrary to expectations arising from CCN impacts, more INPs result in lower n_{i} at all levels and temperatures (Fig. 5.8d,e), as well as lower $n_{\mathrm{i,t}}$ throughout the warm sector (Fig. 5.8f). To investigate this further, the diabatic heating rates of freezing of rain QRFRZ, immersion freezing IMFRZ, and deposition nucleation DEPNUC are analyzed because these processes are directly perturbed by the scaling factor f_{INP} to account for different INP concentrations. The latter two are included in QIHOMHET as heterogeneous ice nucleation (Fig. 5.8g,h). Generally, IMFRZ can occur at temperatures below the threshold of 261 K (green line) and DEPNUC can be active between 220 K and 253 K (orange lines). As expected, larger INPs concentrations systematically increase

IMFRZ and DEPNUC. Figure 5.8h shows this particularly well in the Lagrangian perspective in the temperature range $240 - 261\,\mathrm{K}$. Homogeneous freezing of solution droplets is also part of QIHOMHET. It is parameterized as homogeneous ice nucleation of water vapor HOMNUC and sets in at temperatures lower than 235 K (black line), marking the beginning of a competition between DEPNUC and HOMNUC for water vapor. HOMNUC is lower for higher INP concentrations. This is probably due to the increase in DEPNUC at lower levels, which removes more water vapor, so that there is less water vapor available for HOMNUC at higher levels.

On the other hand, Fig. 5.8j shows that the maximum of the mean QRFRZ is larger for higher INP concentrations and occurs at higher temperatures, as expected. Besides, for lower INP concentrations, the entire vertical profile appears to be shifted to lower temperatures. This shift is also discernible in the Eulerian perspective (Fig. 5.8i). In addition, after the maximum mean QRFRZ is reached in the subset with the most INPs, QRFRZ becomes larger for lower INP concentrations. However, in both perspectives, the median of the subset with the highest INP concentrations is much smaller than the mean at all levels, suggesting the influence of outliers. Therefore, it is reasonable to assume that high INP concentrations do not have a large impact on QRFRZ. Instead, moderate INP concentrations appear to dominate QRFRZ for temperatures between 250 K and 260 K and low INP concentrations between 235 K and 250 K. This contributes to the high n_i for lower INP concentrations between 235 K and 250 K. Nevertheless, HOMNUC is several orders of magnitude larger than QRFRZ, IMFRZ, and DEPNUC, which leads HOMNUC to dominate ice nucleation. This, along with the fact that ice particles formed by HOMNUC have smaller mean sizes, causes n_i to be highest for low INP concentrations.

In summary, increasing the INP concentration directly influences ice nucleation through an increase in immersion freezing and deposition nucleation, which is visible in the Eulerian and Lagrangian perspectives. However, the ice number concentration increases with lower INP concentrations because deposition nucleation is reduced, which leads to a higher availability of water vapor for homogeneous ice nucleation of water vapor, which, in turn, forms on average smaller ice particles.

5.4 Capacitance Impacts

The perturbation of the capacitance has several consequences for the ice phase of the cloud band. When reducing CAP of ice and snow, the graupel mass concentration increases systematically at all levels in the Lagrangian and Eulerian perspective, and the maximum q_g is slightly shifted above the melting level (Fig. 5.9a,b). Therefore, $q_\mathrm{g,t}$ is systematically higher as well throughout the warm sector (Fig. 5.9c). These increases are due to an increase in the depositional growth rate of graupel QGDEP (Fig. 5.9d,g) as the depositional growth rate of ice QIDEP (Fig. 5.9c,h) and snow QSDEP (Fig. 5.9f,i) are lowered by the reduction of CAP. Through the reduction of CAP, the rate of depletion of water vapor is reduced, leading to higher availability of water vapor for the benefit of graupel growth. The increased riming rate may contribute to an increase in q_g as well (Fig. 5.10c,d). Note that the maxima of QGDEP, QIDEP, and QSDEP are also shifted upward when CAP of ice and snow is reduced. The consistent increase in QGDEP is much more

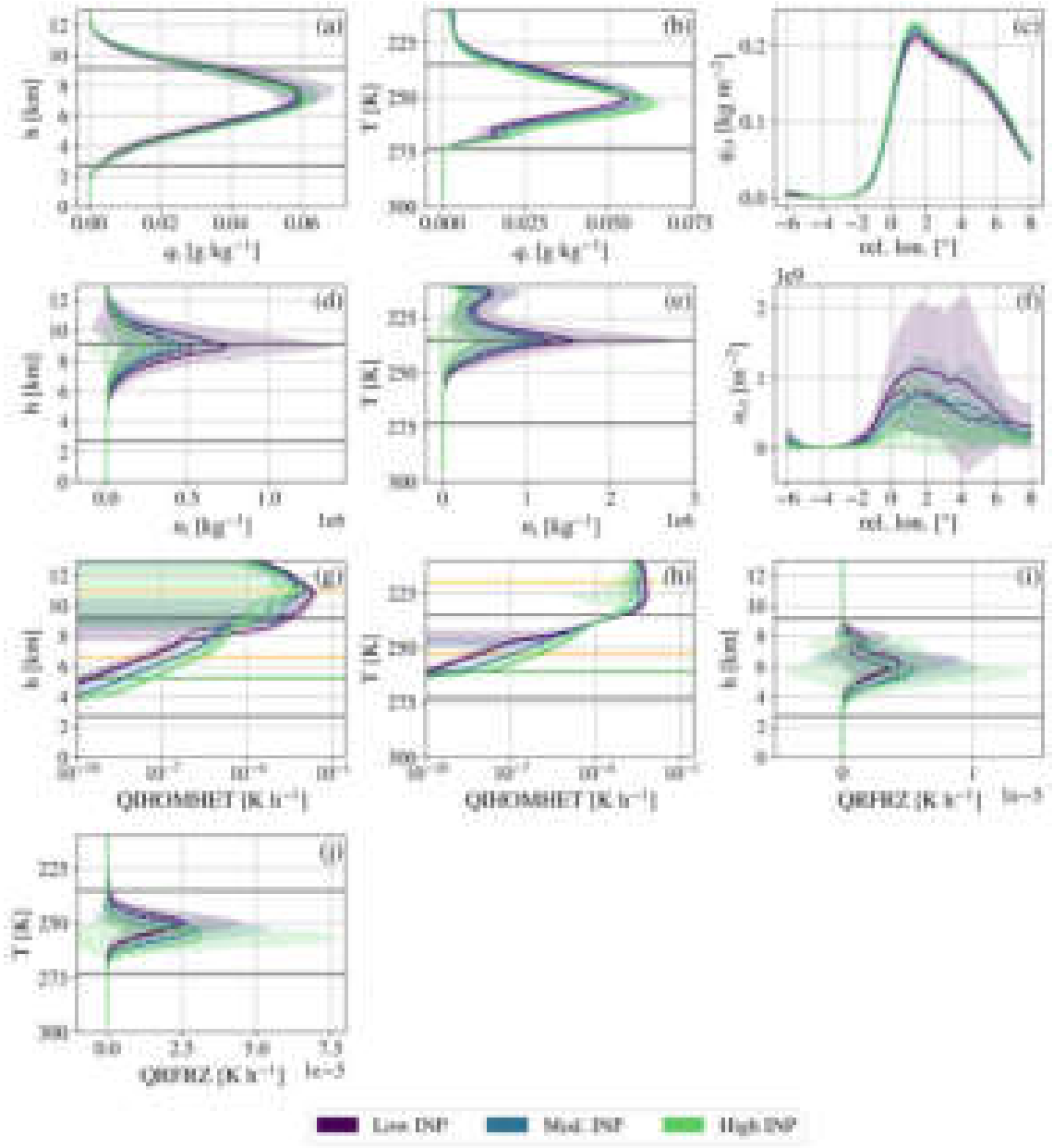

Figure 5.8: As Fig. 5.3 but for low (purple), moderate (blue), and high (green) ice nucleating particle (INP) perturbations. **(a)**, **(b)** Ice mass concentration (q_i, in $g\,kg^{-1}$), **(c)** vertically integrated ice mass concentration ($q_{i,t}$, in $kg\,m^{-2}$), **(d)**, **(e)** ice number concentraion (n_i, in $g\,kg^{-1}$), **(f)** vertically integrated ice number concentration ($n_{i,t}$, in m^{-2}), and **(g)**, **(h)** diabatic heating rate of homogeneous and heterogeneous ice nucleation (QIHOMHET, in $K\,h^{-1}$). For temperatures below 261 K immersion freezing (IMFRZ; green) occurs, deposition nucleation (DEPNUC; orange) occurs between 220 K and 253 K, and homogeneous ice nucleation of water vapor (HOMNUC) occurs below 235 K (upper black line). **(i)**, **(j)** Diabatic heating rate of freezing of rain (QRFRZ, in $K\,h^{-1}$).

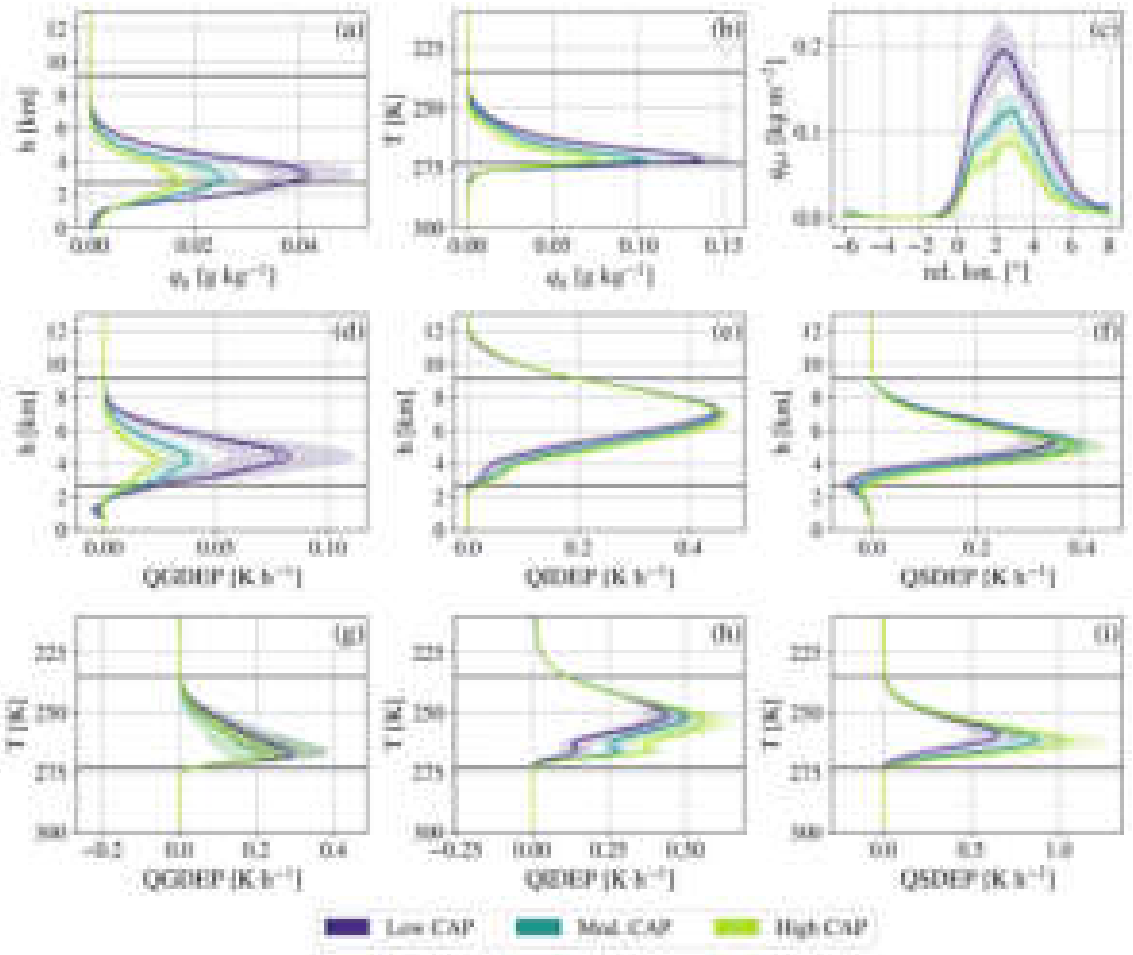

Figure 5.9: As Fig. 5.3 but for low (purple), moderate (blue), and high (green) capacitance (CAP) perturbations. **(a)**, **(b)** Graupel mass concentration (q_g, in $g\,kg^{-1}$), **(c)** vertically integrated graupel mass concentration ($q_{i,t}$, in $kg\,m^{-2}$), and diabatic heating rate of depositional growth of **(d)**, **(g)** graupel (QGDEP, in $K\,h^{-1}$), **(e)**, **(h)** ice (QIDEP, in $K\,h^{-1}$), and **(f)**, **(i)** snow (QSDEP, in $K\,h^{-1}$).

pronounced in the Eulerian perspective, whereas the decreases in QIDEP and QSDEP are more pronounced in the Lagrangian perspective. These differences can occur because the perspectives deal with differently post-processed data: the front relative composites are an average of multiple temporal snapshots of the WCB, which are also spatially averaged, whereas the trajectory data are averaged over all T-binned trajectories. This distinction becomes apparent when comparing QGDEP and QSDEP in the Eulerian perspective to their corresponding profiles in the Lagrangian perspective. In the Eulerian perspective, both QGDEP and QSDEP are negative at lower levels, which means that sublimation of graupel and snow occurs. This can be the case at the edges of the cloud, where graupel and snow can fall and sublimate at higher temperatures. However, this is not shown in the Lagrangian perspective as no sublimation occurs during ascent.

Furthermore, the number concentration of graupel also increases consistently at all levels and its maximum is slightly shifted upward with decreasing CAP of ice and snow (Fig. 5.10a), causing $n_{g,t}$ to increase as well (Fig. 5.10b). This can be attributed to a higher riming rate (Fig. 5.10c,d), which in turn is probably caused by the greater availability of ice and snow particles (Fig. 5.11d,e,j,k). In both perspectives, the consistently higher n_i and n_s may originate from increased HOMNUC (Fig.

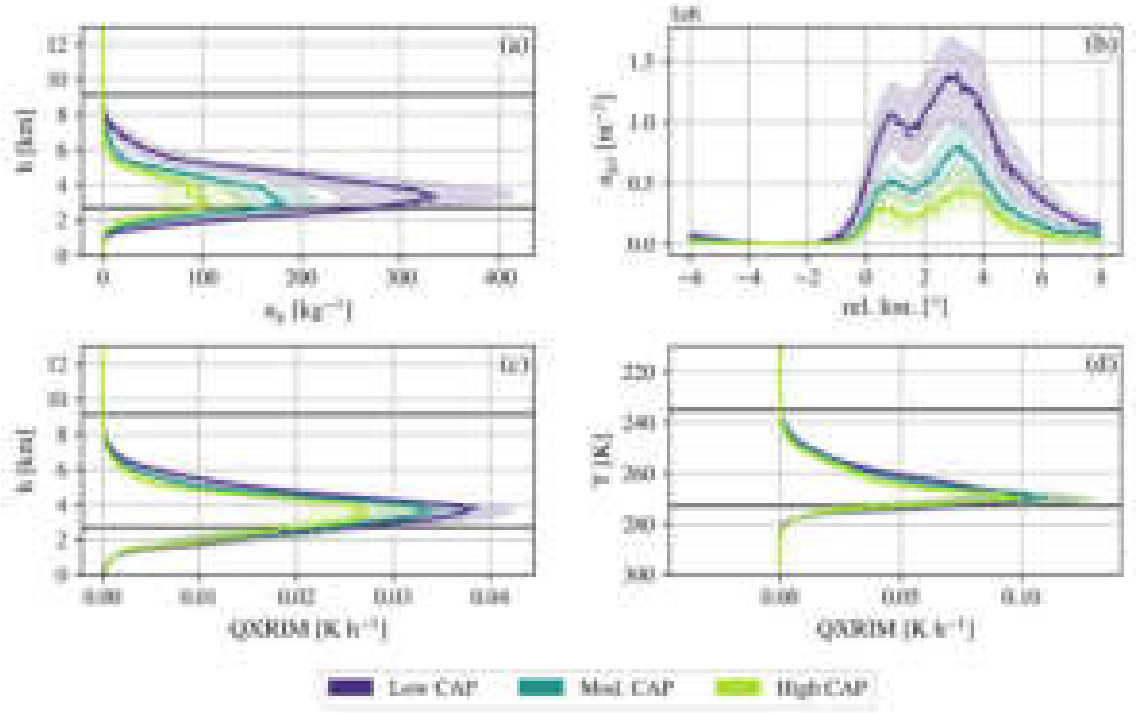

Figure 5.10: As Fig. 5.3 but for low (purple), moderate (blue), and high (green) capacitance (CAP) perturbations. **(a)** Graupel number concentration (n_g, in kg^{-1}), **(b)** vertically integrated graupel number concentration ($n_{g,t}$, in m^{-2}), and **(c)**, **(d)** diabatic heating rate of riming (QXRIM, in $K\,h^{-1}$).

5.12a,b) as more water vapor is available and transported upward when QIDEP and QSDEP are reduced. In addition, the increased homogeneous freezing of cloud droplets QCFRZ (Fig. 5.12c,d) also contributes to higher n_i and n_s, but it is 2-3 orders of magnitude smaller than HOMNUC. Its increase may be connected to a reduction in the WBF process as less QSDEP occurs when CAP is reduced. As a result, more cloud water is left to freeze instead of evaporating and depositing onto snow. Note that HOMNUC leads to smaller mean sizes of ice and snow compared to the other ice nucleation processes, and q_i/n_i and q_s/n_s are generally smaller for lower CAP (Fig. 5.13e,f). This would speak for a reduction in riming, however, the higher n_i and n_s prevail, resulting in an increase in QXRIM in the Eulerian perspective. In contrast, the Lagrangian perspective only shows an increase in QXRIM at temperatures lower than 270 K, and the differences between the subsets appear to be quite small.

Another notable result is the upward shift of the ice mass concentration (Fig. 5.11a,b) for lower CAP of ice and snow. This is unexpected since the lowered CAP reduces QIDEP between 3 km and 7 km or between 270 K and 250 K and above that, QIDEP is not shifted upward as it is no longer affected by CAP perturbations (Fig. 5.9e,h). It occurs, however, because more ice is produced by HOMNUC (Fig. 5.12a,b), which takes place at higher altitudes compared to other ice nucleation processes. In the Eulerian perspective, the maximum of q_i even increases, leading to a small increase in $q_{i,t}$ between 1° and 5° rel. lon. Only below 6 km can a small decrease of q_i be observed. This reduction is more pronounced in the Lagrangian perspectivefor $T > 250$ K. As stated above, n_i increases so much that the total ice mass has to increase as well, although the individual ice particles are smaller on average. Similarly to ice, the snow mass concentration is also shifted

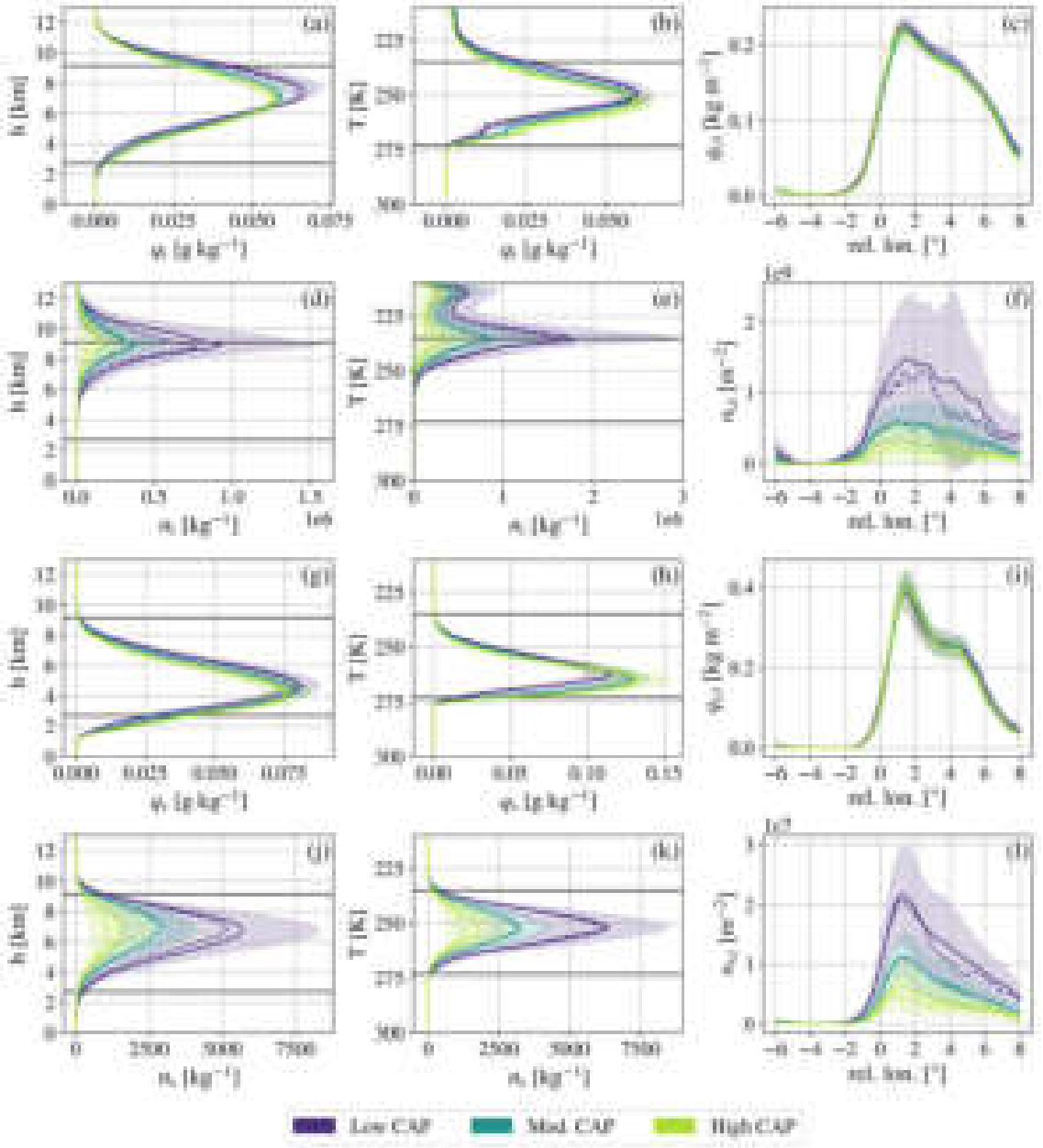

Figure 5.11: As Fig. 5.3 but for low (purple), moderate (blue), and high (green) capacitance (CAP) perturbations. **(a)**, **(b)** Ice mass concentration (q_i, in g kg^{-1}), **(c)** vertically integrated ice mass concentration ($q_{i,t}$, in kg m^{-2}), **(d)**, **(e)** ice number concentraion (n_i, in g kg^{-1}), **(f)** vertically integrated ice number concentration ($n_{i,t}$, in m^{-2}), and **(g-l)** as **(a-f)** but for snow.

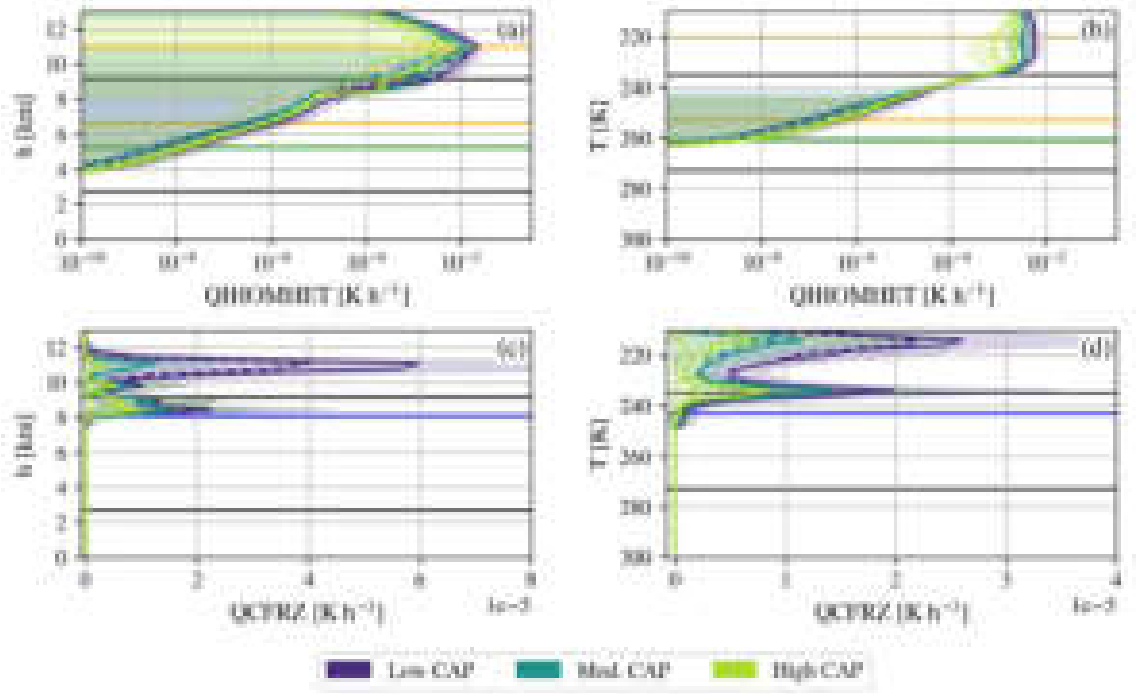

Figure 5.12: As Fig. 5.3 but for low (purple), moderate (blue), and high (green) capacitance (CAP) perturbations. **(a)**, **(b)** Diabatic heating rate of homogeneous and heterogeneous ice nucleation (QIHOMHET, in $\mathrm{K\,h^{-1}}$). For temperatures below 261 K immersion freezing (IMFRZ; green) occurs, deposition nucleation (DEPNUC; orange) occurs between 220 K and 253 K, and homogeneous ice nucleation of water vapor (HOMNUC) occurs below 235 K (upper black line). **(c)**, **(d)** Diabatic heating rate of freezing of cloud droplets (QCFRZ, in $\mathrm{K\,h^{-1}}$). Freezing of cloud droplets occurs for temperatures below 243 K (blue line).

upward, and the maximum q_s is minimally increased for low CAP in the Eulerian perspective (Fig. 5.11c). However, $q_\mathrm{s,t}$ seems to be unaffected (Fig. 5.11i). In the Lagrangian perspective, only a shift of q_s to lower temperatures is observed, and the maximum of q_s actually decreases a bit for lower CAP (Fig. 5.11h), which is expected based on the decrease in QSDEP (Fig. 5.9i). Again, similar to ice, the upward shift of q_s is related to the increase in n_s.

Due to the impacts of CAP on upper-tropospheric cloud characteristics, the radiation balance at TOA is influenced by CAP. Analysis of CAP perturbations reveals a reduction in absolute net longwave radiation at TOA LW in the warm sector for low CAP of ice and snow (Fig. 5.13a). This means that the outgoing longwave radiation (OLR) emitted to space is reduced. The reason for this is probably the increase in q_i near the cloud top (Fig. 5.11a,b) and the increase in $q_\mathrm{i,t}$ (Fig. 5.11c), which both contribute to an increase in the absorption of OLR emitted from below the cloud. Besides, more ice crystals occur at lower temperatures near the cloud top (Fig. 5.11d,e), leading to a reduction in longwave radiation emission, according to the Stefan-Boltzmann law, and subsequently a reduction in OLR. The net shortwave radiation at TOA SW, on the other hand, is minimally reduced for lower CAP between 0 and 1° rel. lon. (Fig. 5.13b). This may result from the higher reflectivity of the cloud due to its higher optical depth, which in turn is caused by higher $n_\mathrm{i,t}$, $n_\mathrm{s,t}$ (Fig. 5.11f,l). Shortwave heating rates RADSW (Fig. 5.13b) are slightly increased for low CAP in the vicinity of the n_i maximum. Moreover, longwave cooling rates RADLW (Fig. 5.13c) are increased in the same region due to more ice particles.

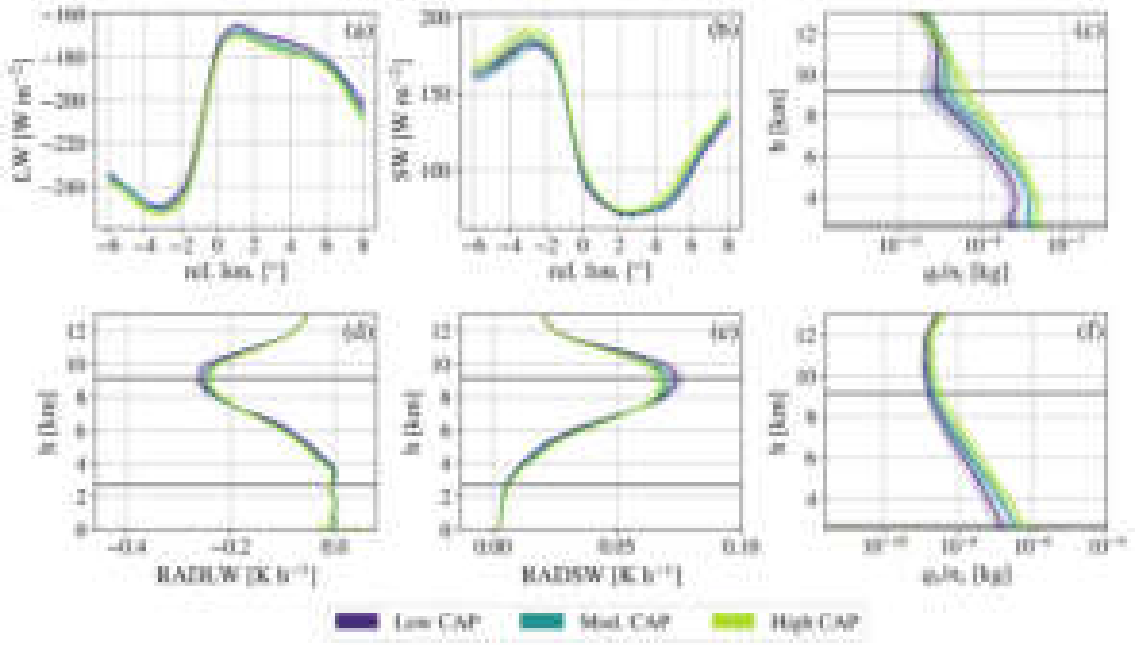

Figure 5.13: As Fig. 5.3 but for low (purple), moderate (blue), and high (green) capacitance (CAP) perturbations. **(a)** Net longwave radiation at TOA (LW, in $\mathrm{W\,m^{-2}}$), **(b)** net shortwave radiation at TOA (SW, in $\mathrm{W\,m^{-2}}$), **(c)** mean ice particle mass ($q_\mathrm{i}/n_\mathrm{i}$, in kg), **(d)** longwave cooling rate (RADLW, in $\mathrm{K\,h^{-1}}$), **(e)** shortwave heating rate (RADSW, in $\mathrm{K\,h^{-1}}$), and **(f)** mean snow particle mass ($q_\mathrm{s}/n_\mathrm{s}$, in kg).

To sum up, decreasing CAP of ice and snow leads to a systematically higher graupel mass and number concentration that is consistent at all levels in the Eulerian and Lagrangian perspectives. It is caused by the consistent increase in water vapor deposition onto graupel as a consequence of a reduction of QSDEP and QIDEP as well as an increase in riming. In addition, the number concentrations of ice and snow are higher for lower CAP due to an increase in homogeneous ice nucleation of water vapor and homogeneous freezing of cloud droplets. Lastly, the net longwave radiation at TOA is reduced when CAP decreases as the increased mass concentration of ice reduces OLR. However, the changes in the net longwave radiation at TOA are overall small.

5.5 Sea Surface Temperature and Maximum Supersaturation Impacts

Perturbations of the sea surface temperature and maximum supersaturation with respect to liquid exhibit no substantial systematic influence on the WCB cloud structure and are therefore not discussed in detail. While their overall impact is limited compared to other parameter perturbations, a slight reduction in net shortwave radiation at TOA is noticeable east of 4° rel. lon. for higher SSTs (Fig. 5.14a). This may result from an increase in cloud optical depth, driven by higher $n_\mathrm{i,t}$ and $n_\mathrm{s,t}$ values (Fig. 5.14c,d) and smaller mean sizes of ice particles (Fig. 5.14b). However, the overlap of the standard deviations (shading) of $n_\mathrm{i,t}$ and $n_\mathrm{s,t}$ indicates that there is no systematic impact of SST perturbations on $n_\mathrm{i,t}$ and $n_\mathrm{s,t}$. In addition, $q_\mathrm{i,t}$ and $q_\mathrm{s,t}$ do not exhibit a substantial systematic influence of SST perturbations either and are therefore not shown.

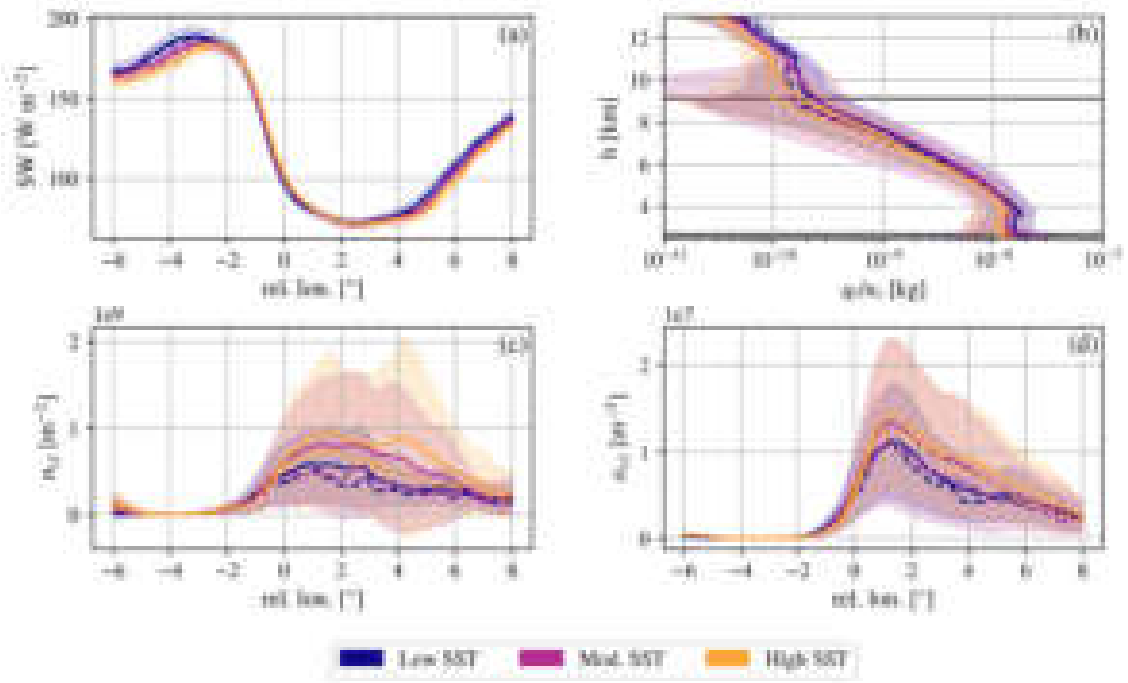

Figure 5.14: As Fig. 5.3 but for low (purple), moderate (magenta), and high (orange) sea surface temperature (SST) perturbations. **(a)** Net songwave radiation at TOA (SW, in $\mathrm{W\,m^{-2}}$), **(b)** mean ice particle mass ($q_\mathrm{i}/n_\mathrm{i}$, in kg), and vertically integrated number concentration of **(c)** ice ($n_\mathrm{i,t}$, in $\mathrm{m^{-2}}$) and **(d)** snow ($n_\mathrm{s,t}$)).

6 Quantification of Uncertainty Contributions

To determine the contribution of each parameter perturbation to the uncertainty of the WCB cloud structure, random forest regression models (Section 3.4.2) are built for hydrometeor mass concentrations, number concentrations, and diabatic heating rates. These RFR models are used to perform a variance decomposition (Section 3.5) of those variables with their respective RFR model predictions. Table A.2 shows the different mean altitudes, temperatures, and relative longitudes for which RFR models are trained using the training dataset averaged over specified ranges for the mean vertical profiles of the cross-section composites, the T-binned trajectory data, and the front relative cross-section composites, respectively. The purpose of the RFR models, based on height (Eulerian perspective) and temperature (Lagrangian perspective), is to capture the temperature regions where distinct ice nucleation processes occur, i.e., freezing of rain ($T < 273\,\mathrm{K}$), immersion freezing ($T < 261\,\mathrm{K}$), deposition nucleation ($T < 253\,\mathrm{K}$), freezing of cloud droplets ($T < 243\,\mathrm{K}$) and homogeneous ice nucleation of water vapor ($T < 235\,\mathrm{K}$). Those regions are chosen not only because they allow for analysis of ice nucleation processes but also because they primarily cover the mixed phase. In the mixed-phase region, most hydrometeors reach their maximum in terms of mass and number concentration, and are overall most influenced by parameter perturbations. Generally, there are two dominant parameters, CCN and CAP, that are highly relevant for the variance in the cloud properties. In the following, the parameter contributions to the uncertainty of liquid hydrometeors (Section 6.1), frozen hydrometeors (Section 6.2), and net radiation (Section 6.3) are analyzed in detail.

6.1 Liquid Hydrometeors

The sensitivity index S_i (3.2) shown in Fig. 6.1 describes the contributions of the perturbed parameter i to the variance in liquid hydrometeor mass concentrations q_x in the Eulerian perspective (first column) and in the Lagrangian perspective (second column), as well as vertically integrated liquid hydrometeor mass concentrations $q_\mathrm{x,t}$ (third column). The sensitivity index is based on variance decomposition performed with RFR model predictions and is only shown if the altitude and temperature regions are suitable for the individual variables. In addition, the R^2 scores of the RFR models need to be ≥ 0.5. As expected from the analysis of the CCN impacts (Section 5.2), the (vertically integrated) cloud water and rain mass concentrations strongly depend on the CCN concentration, which is indicated by the high sensitivity index S_CCN (Fig. 6.1a-f). The same applies to n_c, $n_\mathrm{c,t}$, n_r, $n_\mathrm{r,t}$, and QCNUC (Fig. 6.2). Especially for the lowest level, which starts at 2.4 km and

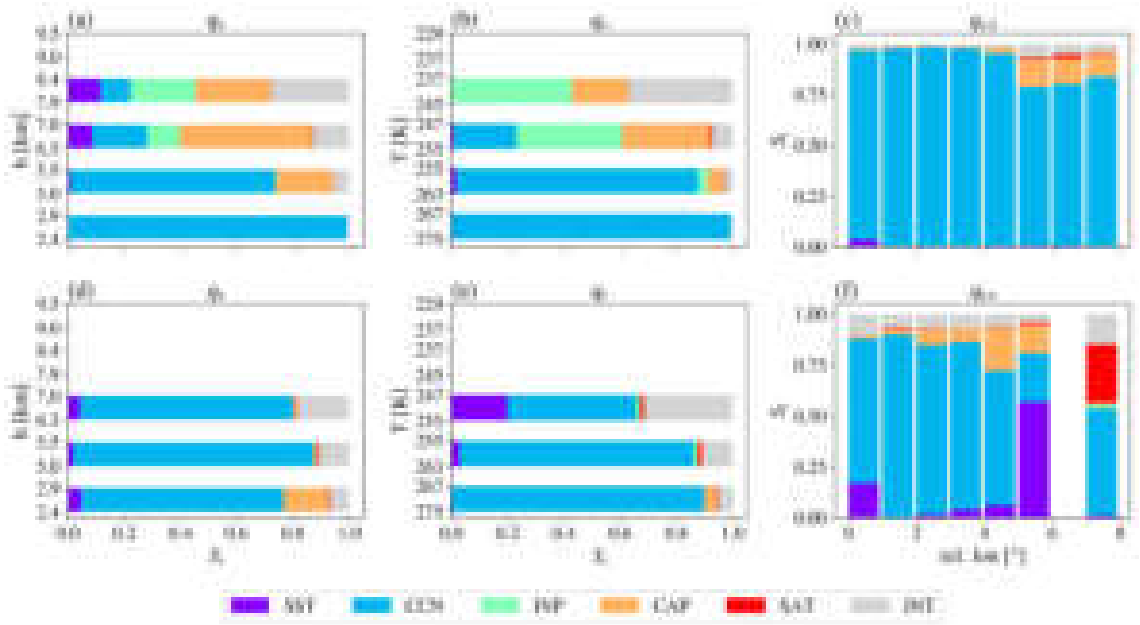

Figure 6.1: Sensitivity index S_i of sea surface temperature (SST; purple), cloud condensation nucleus concentration (CCN; blue), ice nucleating particle concentration (INP; green), capacitance (CAP; orange), and maximum supersaturation with respect to liquid (SAT; red) perturbations, and interactions between these perturbed parameters (INT; grey). The sensitivity index is based on variance decomposition for vertical profiles of liquid hydrometeor mass concentration (q_x; first and second column) as well as for vertically integrated liquid hydrometeor mass concentration ($q_{x,t}$) as function of distance to the cold front (at rel. lon. 0-8°; third column) for **(a-c)** cloud water and **(d-f)** rain. The variance decomposition is based on random forest regression (RFR) models and performed for averages over different altitude ranges (first column) in the Eulerian perspective, temperature ranges (second column) in the Lagrangian perspective, and relative longitudes (third column) in the Eulerian perspective, as listed in Table A.2. The respective RFR model hyperparameters and scores are listed in Table A.3-A.5. Note that the Lagrangian perspective covers mainly the mixed phase for better comparison between all hydrometeor types.

275 K, almost 100 % of the variance in QCNUC, n_c, and q_c is explained by CCN perturbations. The variance decomposition of QCNUC also shows minor influences of CAP at higher levels. Besides, CAP impacts are visible in the upper levels of q_c and n_c as well. This is an indication of the WBF process occurring in the mixed-phase region. It is driven by the ice phase, i.e., QSDEP (Fig. 6.3c,d), which is controlled by CAP and causes subsaturation w.r.t. liquid, which is then removed by the second saturation adjustment by removing cloud water. Throughout the warm sector, $q_{c,t}$ depends strongly on the CCN concentration, and $n_{c,t}$ exhibits almost exclusively a dependence on the CCN concentration. Similarly, CCN concentrations also contribute the most to the variance of $q_{r,t}$ (Fig. 6.1f) and $n_{r,t}$ (Fig. 6.2f), which Fig. 5.4d,e showed above. In contrast to $q_{c,t}$ and $n_{c,t}$, $q_{r,t}$ and $n_{r,t}$ are more influenced by interactions of the parameter perturbation. In particular, S_{INT} amounts on average to roughly 20 % throughout the warm sector.

6.2 Frozen Hydrometeors

Contrary to expectations arising from Fig. 5.8d,e, the impact of varying INP concentrations on n_i is only barely visible at the levels with the lowest temperatures (Fig. 6.5b) and is not discernible

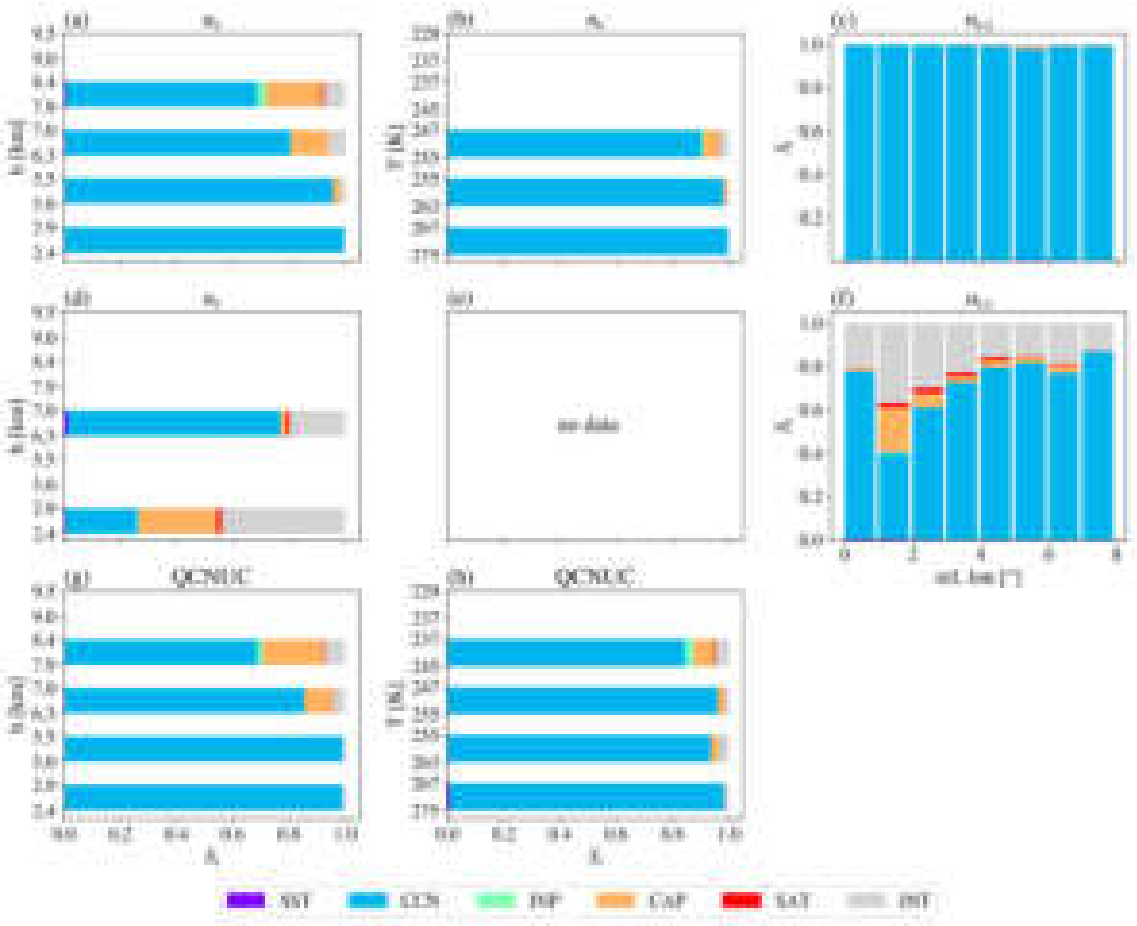

Figure 6.2: As Fig. 6.1 but for **(a)**, **(b)**, **(d)**, **(e)** liquid hydrometeor number concentration (n_x), **(c)**, **(f)** vertically integrated liquid hydrometeor number concentration ($n_{x,t}$), and **(g)**, **(h)** diabatic heating rate of cloud droplet activation (QCNUC).

in the Eulerian perspective of n_i and $n_{i,t}$ (Fig. 6.5a,c). In the temperature ranges where IMFRZ and DEPNUC set in, a slight dependence of q_i on the INP concentration is noticeable (Fig. 6.4b). Again, this is not reflected in the Eulerian perspective (Fig. 6.4a,c), which is consistent with the expected low impact of INP concentrations on q_i and $q_{i,t}$, based on Fig. 5.8a-c. Instead, CAP is the most dominant contributor to the variance of n_i and $n_{i,t}$ at all levels and to q_i and $q_{i,t}$ at most levels, whereby $q_{i,t}$ is also strongly influenced by SST (up to 80 %) and SAT (up to 20 %) perturbations. The SST influence appears to be mainly at the "edges" of the cloud, i.e., between 0° and 2° rel. lon. and between 5° and 8° rel. lon. Especially, the high SST influence of 80 % between 0° and 1° rel. lon. is unexpected, as no substantial impact of SST perturbations on $q_{i,t}$ is found in Section 5.5. In addition, $q_{i,t}$ is generally quite insensitive to all parameter perturbations, particularly SAT, thus the RFR models probably try to find any relation between the parameters and $q_{i,t}$, which is not necessarily the most reasonable. Other than that, the variance decomposition of QIHOMHET shows a large influence of INP concentrations, as expected, in the temperature ranges where IMFRZ and DEPNUC are active (Fig. 6.6b). In the Eulerian perspective, QIHOMHET is also influenced by INP concentrations between 6.3 km and 7 km, where IMFRZ and DEPNUC occur. For these levels, the variance of n_i should depend to some extent on the INP concentration, but, as already mentioned, the influence of CAP dominates.

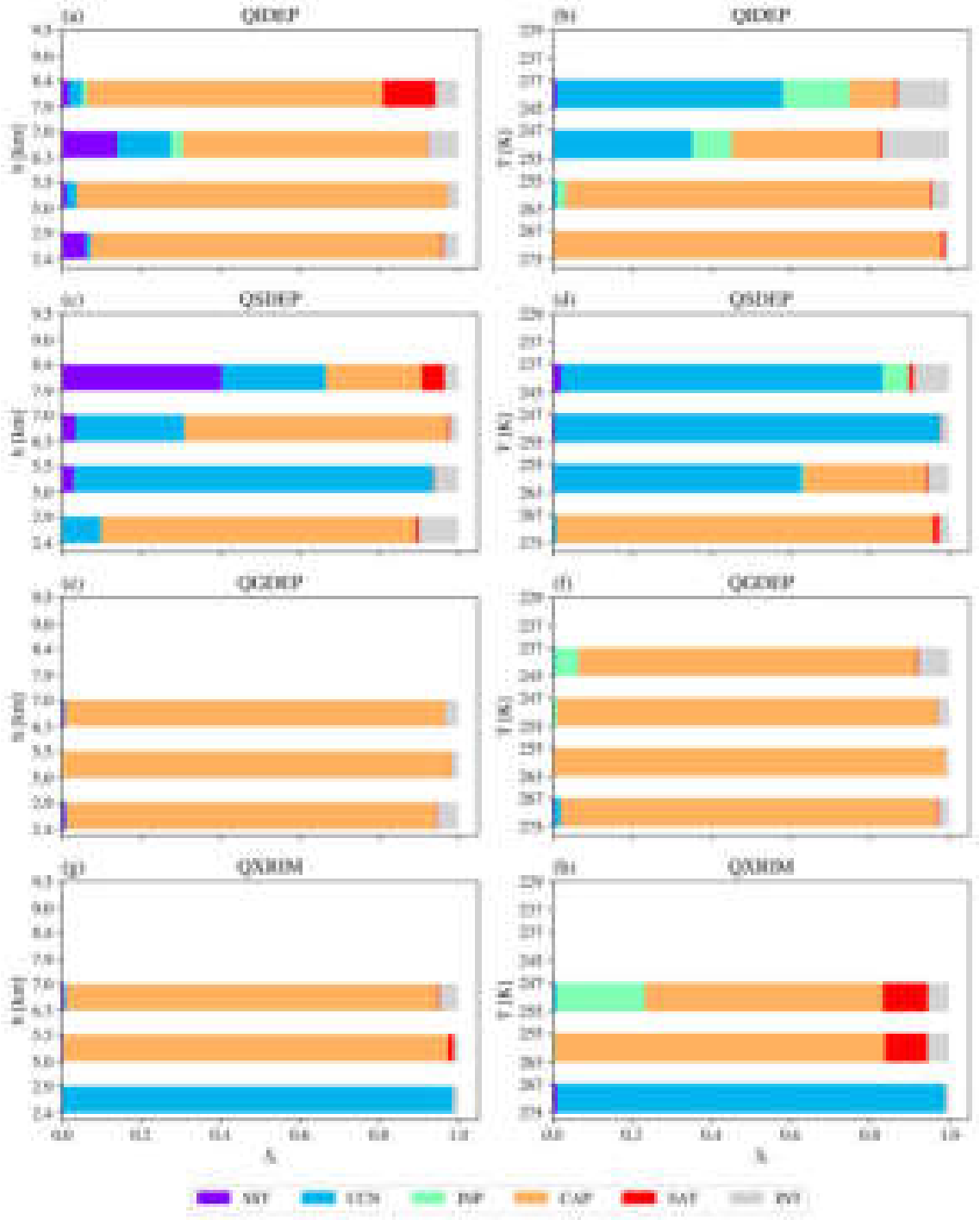

Figure 6.3: As Fig. 6.1 but for diabatic heating rate of depositional growth of **(a)**, **(b)** ice (QIDEP), **(c)**, **(d)** snow (QSDEP), and **(e)**, **(f)** graupel (QGDEP), as well as **(g)**, **(h)** diabatic heating rate of riming (QXRIM).

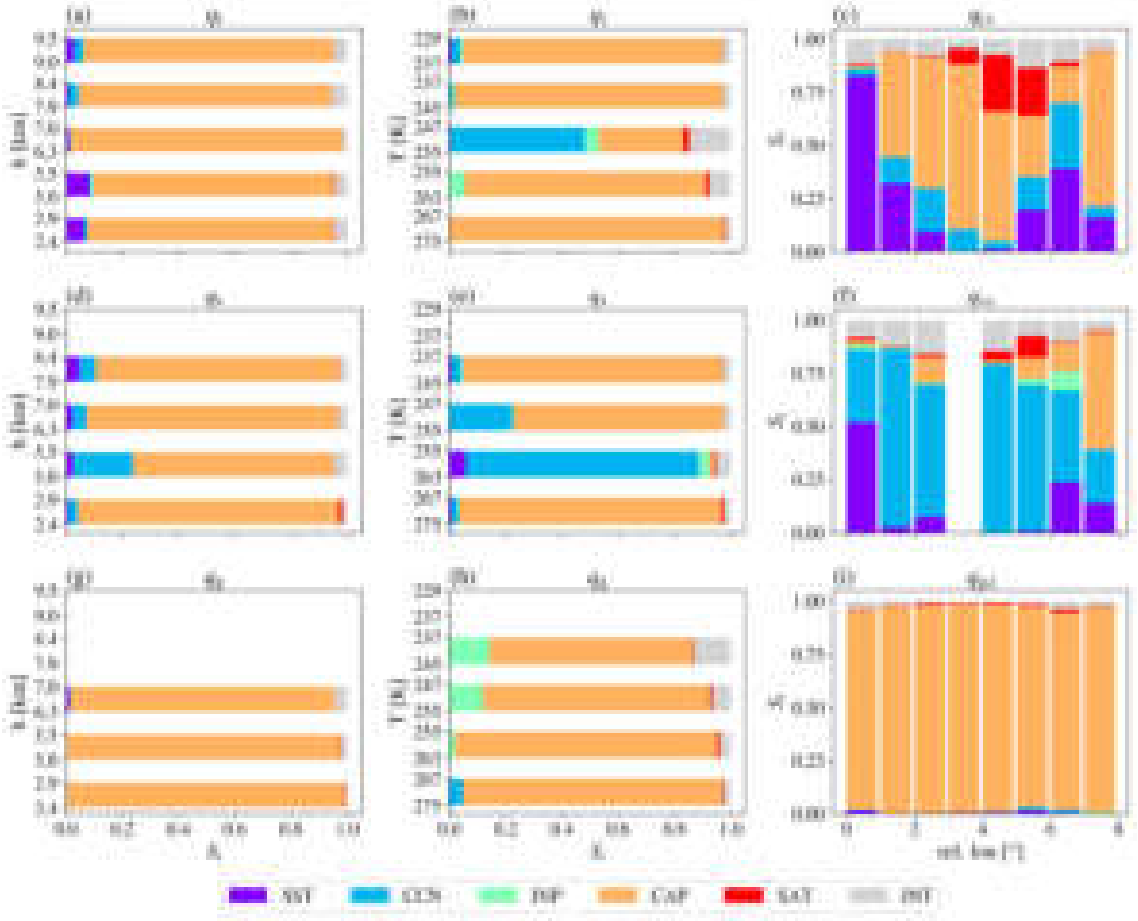

Figure 6.4: As Fig. 6.1 but for frozen hydrometeor mass concentrations: **(a-c)** ice, **(d-f)** snow, and **(g-i)** graupel.

Besides, variance decomposition identifies a dependence of QRFRZ on INP concentrations with $S_{\mathrm{inp}} = 0.2$ where freezing of rain is supposed to begin (Fig. 6.6f). In the Eulerian perspective, no sensitivity indices can be determined for the lowest level (Fig. 6.6e) because the R^2 score of the RFR model is zero. However, between 5 km and 5.5 km, a small influence of INP concentration is visible. In general, the variance of QRFRZ is mostly controlled by CCN concentrations, which may be related to the dependence of QRFRZ on the mean raindrop mass that is influenced by the CCN concentration as depicted in Fig. 5.4f. However, n_{i} seems not to be substantially influenced by CCN perturbations because, as already stated, CAP perturbations are identified as the dominant influence on n_{i}.

Ice nucleation through homogeneous freezing of cloud droplets is most strongly influenced by CAP (roughly 60 %) and CCN concentration contributes 20 % to the uncertainty of QCFRZ between 7.9 km and 8.4 km (Fig. 6.6c). In the altitude range above, the contribution of CCN is almost doubled, whereas the contribution of CAP is approximately reduced by 50 %. Generally, it is reasonable that the amount of CCN affects the freezing rate of cloud droplets, since CCN concentrations govern n_{c} and q_{c}. In contrast, the influence of CAP, which is even more pronounced in the Lagrangian perspective (Fig. 6.6d), is indirect because QCFRZ does not depend on CAP. It probably relates to the WBF process. When CAP of snow is reduced, QSDEP decreases as

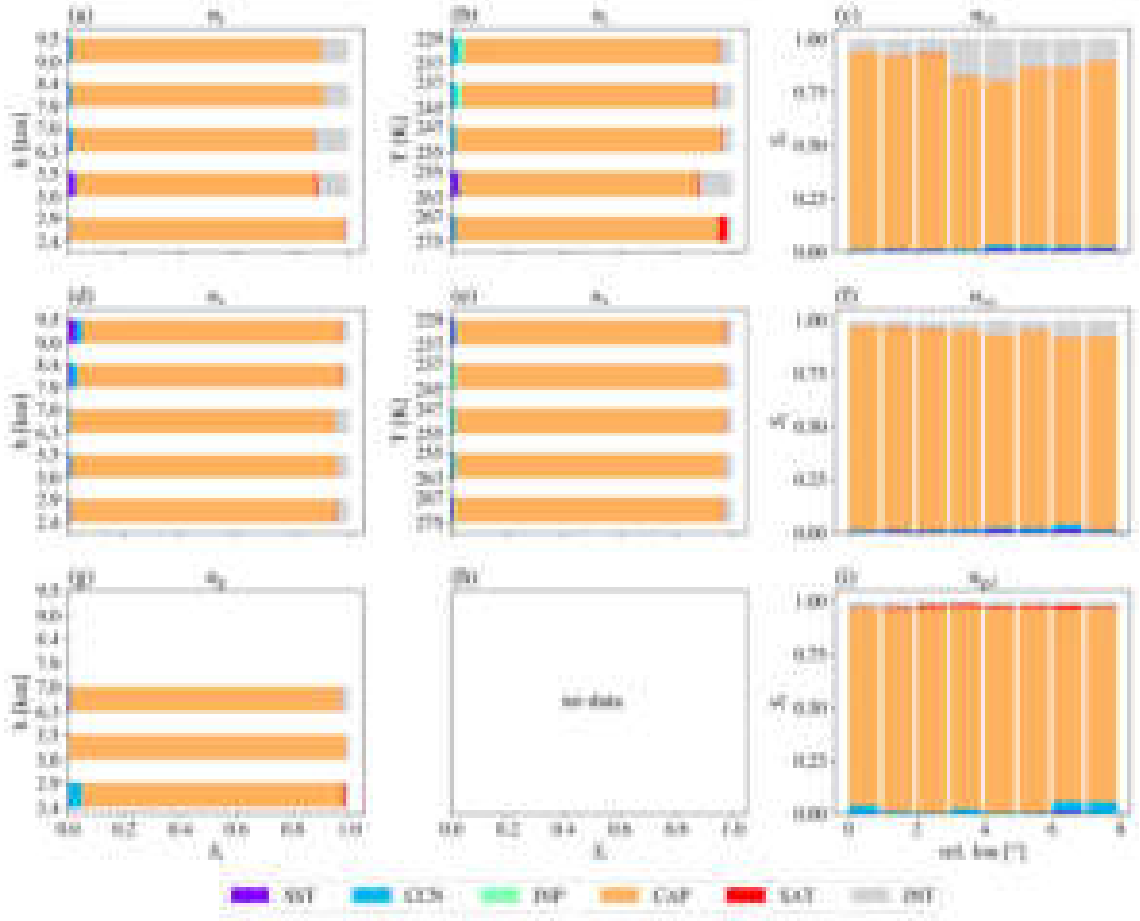

Figure 6.5: As Fig. 6.1 but for frozen hydrometeor number concentrations: **(a-c)** ice, **(d-f)** snow, and **(g-i)** graupel.

well (Fig. 5.9f,i). As a consequence, more cloud water can potentially remain in the liquid phase instead of evaporating and depositing onto snow. This additional cloud water can then rise to higher altitudes where it freezes, contributing to QCFRZ.

The variance of q_i is dominated by CAP perturbations (Fig. 6.4a,c), as previously mentioned. This is in accordance with the expected dependence of QIDEP on CAP (Fig. 6.3a,b). Interestingly, S_CCN is quite high for the upper levels of QIDEP in the Lagrangian perspective.

Since n_i and $n_\mathrm{i,t}$ depend primarily on CAP, the same applies to n_s and $n_\mathrm{s,t}$ (Fig. 6.5d-f) as snow forms from ice aggregation and water vapor deposition onto ice. In fact, the (vertically integrated) number concentration of snow depends even more strongly on CAP, with $S_\mathrm{CAP} > 0.9$ at all levels, than the (vertically integrated) number concentration of ice. This dependence is in agreement with Fig. 5.11j-l. In contrast, the variance decomposition of q_s reveals that it is not consistently influenced by CAP at all levels (Fig. 6.4d,e). In the Lagrangian perspective between 263 K and 255 K, a strong dependence on the CCN concentration is discernible, which is in agreement with the T-binned profile of q_s (Fig. 5.5d). To a lesser extent, the influence of CCN is also visible in the Eulerian perspective at the corresponding level between 5 km and 5.5 km, which again agrees with Fig. 5.5a. At this level in both perspectives, QSDEP depends the most on CCN concentrations (Fig. 6.3c,d), which may explain the contribution of CCN to the variance in q_s. Aside from that,

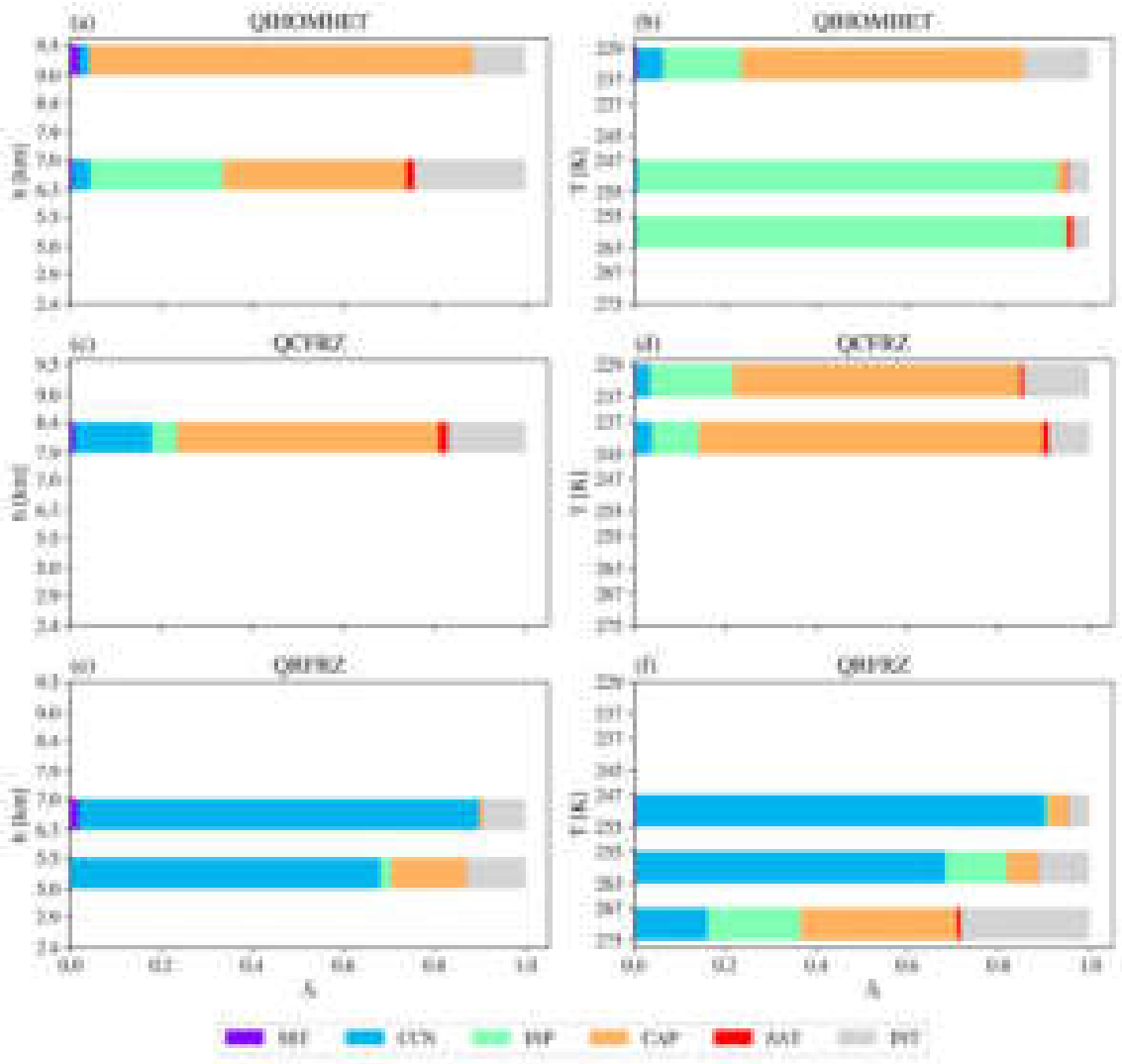

Figure 6.6: As Fig. 6.1 but for diabatic heating rate of **(a)**, **(b)** homogeneous and heterogeneous ice nucleation (QIHOMHET), **(c)**, **(d)** freezing of cloud droplets (QCFRZ), and **(e)**, **(f)** freezing of rain (QRFRZ).

S_{CAP} of QSDEP is only dominant at the lowest level in both perspectives and between 6.3 km and 7 km in the Eulerian perspective, which is unexpected since CAP perturbations directly influence the depositional growth of snow. Besides, S_{CCN} dominates the upper levels in the Lagrangian perspective. The considerable dominance of S_{CCN} in both perspectives is probably linked to the WBF process. Based solely on the variance decomposition of QSDEP, the variance of q_{s} should be more strongly influenced by CCN perturbations. Note that the large influence of the SST on QSDEP between 7.9 km and 8.4 km is not necessarily reasonable, since in that altitude range, QSDEP is rather insensitive to all parameter perturbations and varies minimally. In line with the small variability shown in Fig. 5.11i, the variance of $q_{\mathrm{s,t}}$ is barely determined by CAP (Fig. 6.4f). Instead, CCN concentrations are dominant throughout the warm sector, which agrees with Fig. 5.5g, hinting at a stronger WBF process. Between 0° and 1° rel. lon., SST perturbations make up 50 % of the variance. Only between 7° and 8° rel. lon. is the influence of CAP the largest. These unexpected contributions to the variance of $q_{\mathrm{s,t}}$ arise probably because $q_{\mathrm{s,t}}$ does not exhibit a large variance to begin with (Fig. 5.11i), as is the case for $q_{\mathrm{i,t}}$.

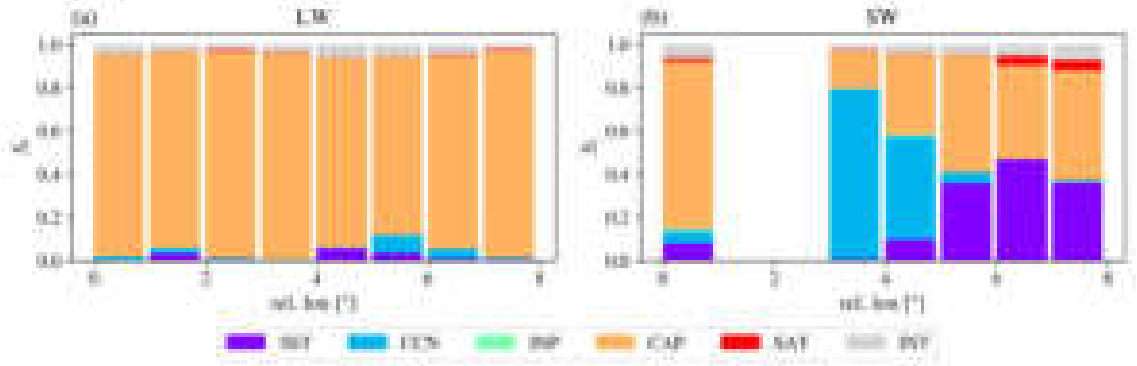

Figure 6.7: As Fig. 6.1 but for **(a)** net longwave radiation at TOA (LW) and **(b)** net shortwave radiation at TOA (SW).

Regarding graupel mass and number concentrations, strong influences of CAP and lesser ones of CCN concentrations are expected based on the analysis in Sections 5.4 and 5.2. Variance decomposition, however, reveals that q_g and $q_{g,t}$ (Fig. 6.4g-i), as well as n_g and $n_{g,t}$ (Fig. 6.5g-i), primarily depend on CAP at all levels. CCN concentrations appear to have only a minor impact on n_g at the lowest level and on q_g at the lowest level of the Lagrangian perspective whereas the impacts on $q_{c,t}$ and $n_{g,t}$ are spread across the warm sector. Aside from that, graupel is highly sensitive to CAP. Nevertheless, the variance of QXRIM almost depends completely on the CCN concentration at the lowest level (Fig. 6.3g,h). However, this seems to be overshadowed by the distinct dependence of QGDEP on CAP (Fig. 6.3e,f), leading to the high S_{CAP} of q_g and $q_{g,t}$.

6.3 Net Radiation

Figure 6.7a shows that the variance of the net longwave radiation at TOA depends almost everywhere in the warm sector for more than 90 % on CAP. This is in accordance with the expectations based on the CAP impact seen in Fig. 5.13a. In contrast, the net shortwave radiation at TOA (Fig. 6.7b) is mainly influenced by CAP directly at the cold front. Further east up to 5° rel. lon., CCN concentrations dominate and even further east between 5° and 8° rel. lon., SST perturbations seem to be of importance. The regions where the influences of CCN and SST perturbations are relevant coincide with the composites of SW, shown in Fig. 5.7c and 5.14a. Note that for $1-3°$ rel. lon., the R^2 scores of the RFR models are below 0.5 and therefore the sensitivity indices are not shown.

Short Summary

The liquid hydrometeors of the cloud are mainly influenced by the CCN perturbations, whereas the frozen hydrometeors are dominated by CAP perturbations. The net longwave radiation at TOA is also determined by CAP, and the net shortwave radiation at TOA is influenced by CAP, CCN concentration, and SST.

7 Discussion

The analysis of the PPE simulations of the WCB case study provides new insights on how parameter uncertainties influence the cloud structure of a WCB. In the following, the main results are compared with the existing literature and assessed with respect to their implications for NWP. For this, the main focus lies on the impacts of CCN and CAP perturbations as they are the most relevant. Note that this thesis focuses only on source terms regarding the cloud structure. However, sink terms are also relevant. Furthermore, limitations of this thesis are discussed.

There are few previous studies on how CCN concentrations influence the cloud structure of a WCB. However, several studies (Tao et al., 2012; Schneider et al., 2019; Barthlott et al., 2022; Marinescu et al., 2021) have examined the importance of CCNs in the context of convective clouds. The systematic increase in cloud water mass concentration with increasing CCN concentration observed in this study and the related decrease in rain mass concentration are in agreement with the findings of Barthlott et al. (2022). They attributed the decrease in rain mass concentration to a decrease in the autoconversion of cloud water to rain as the cloud droplets are smaller, as found in this study. In contrast, Schneider et al. (2019) pointed out that for convective clouds, the influence of CCN concentration on precipitation is complex and case dependent. They found that the precipitation response depends on updraft intensity and whether warm- or cold-rain processes dominate. This implies that for other WCB cases, an increase in the CCN concentration may not necessarily lead to a reduction in the rain mass concentration. Furthermore, Barthlott et al. (2022) found a decrease in graupel mass concentration with increasing CCN concentrations due to a reduction in riming, which is consistent with our findings. Moreover, they reported an increase in vapor deposition in general and related it to the WBF process consuming more water vapor. We also find an increase in the diabatic heating rate of vapor deposition onto snow with increasing CCN concentrations. Since this study shows that the uncertainty in the CCN concentration has a substantial impact on the liquid hydrometeors of the WCB cloud, incorrect model representation may be prone to errors in precipitation forecasts, and CCNs influence surface precipitation structure and intensity (Oertel et al., 2025b).

In addition to that, the variance decomposition highlights the importance of uncertainties in CCN concentrations for the net shortwave radiation at TOA at around 4° rel. lon. This could be due to a higher cloud optical depth (Barthlott et al., 2022) caused by the increase in the cloud droplet number concentration and the shift to smaller mean cloud droplet sizes when the CCN concentration is increased. The observed influence of SST on the net shortwave radiation at TOA east of 4° rel. lon. may be related to increased $n_{\mathrm{i,t}}$ and $n_{\mathrm{s,t}}$ and decreased mean ice particle sizes for higher SSTs. When there are more snow and ice particles and the mean ice particle sizes are also smaller near the

cloud top, the cloud becomes optically thicker, i.e., the cloud optical depth increases. Consequently, more shortwave radiation is reflected at the cloud top back to space, and the net shortwave radiation at TOA decreases. The increases in $n_{i,t}$ may be due to secondary ice production through the Hallett-Mossop process (Lamb and Verlinde, 2011). It is active between $-3\,°C$ and $-8\,°C$ and describes an increase in ice number concentration through ice splintering during riming. In this temperature range, an increase in the riming rate with increased SST is discernible (Fig. A.1a,b), as well as an increase in ice number concentration (Fig. A.1c,d). However, the variance decomposition of vertically integrated ice and snow number concentrations does not show a significant contribution of SST perturbations. Thus, SST perturbations are not as important for $n_{i,t}$ and $n_{s,t}$. Another possible explanation for the impact of SST on the net shortwave radiation at TOA may be a poleward extension of the WCB inflow region for higher SST (Oertel et al., 2025b). Closer to the pole, the incoming solar radiation is generally reduced, leading to a smaller net shortwave radiation, as the cloud band is potentially shifted further north for higher SST.

Furthermore, we find that increasing the INP concentration decreases the ice number concentration in the mixed and ice phase. This disagrees with Lee et al. (2024), who investigated the impact of INPs on stratiform mixed-phase clouds. Li et al. (2013) also analyzed mixed-phase clouds and found that increasing the INP concentration initially decreases the ice number concentration as heterogeneous and homogeneous freezing compete. However, when the number of INPs is increased further, the ice number concentration increases again, which is not observed in our study. They attributed this increase to heterogeneous freezing dominating homogeneous freezing. We also observe that the heterogeneous ice nucleation rates are higher for higher INP concentrations and that the homogeneous ice nucleation rate of water vapor is lower for higher INP concentrations. Despite that, HOMNUC is crucial in our study for the ice number concentration, as it is a few orders of magnitude larger than the other ice nucleation processes. However, variance decomposition shows that the INP perturbations are only relevant for the diabatic heating rates of immersion freezing and deposition nucleation. In this thesis, the influence of INP perturbations on the ice number concentration is negligible compared to CAP perturbations as they predominantly determine the ice number concentration through HOMNUC.

In line with expectations based on Eq. (2.7) and Westbrook and Heymsfield (2011), reducing CAP of ice and snow leads to a decrease in their depositional growth rates. However, despite the reduced deposition onto ice and a smaller mean ice particle mass below 12 km, the maxima of $q_{i,t}$ and q_i in the Eulerian perspective increase slightly at lower CAPs. This is likely due to significant increases in $n_{i,t}$ and n_i, driven by enhanced HOMNUC activity due to increased water vapor availability. In contrast, snow mass concentrations respond differently: the maximum q_s in the Lagrangian perspective decreases slightly with lower CAPs, while $q_{s,t}$ remains mostly unaffected. The relatively small overall decrease in snow mass is probably explained by the substantial increases in $n_{s,t}$ and n_s, possibly resulting from intensified ice aggregation linked to higher ice number concentrations. In general, the variance decomposition confirms that number concentrations of ice and snow are predominantly influenced by uncertainties in CAP. This aligns with the findings of Johnson et al. (2015), who studied the uncertainty in convective cloud microphysics. They also found that the shape of ice crystals, considered by the capacitance, determines the uncertainties in the number

and mass of ice crystals. In addition to that, they found that immersion freezing and deposition nucleation rates, as well as aerosol concentrations, also contribute to that. All of these contributors were independently perturbed as they do not influence each other in their study. In contrast, IMFRZ and DEPNUC are equally perturbed in our study by varying the INP concentration, but this influence is only minimally represented in the variance decomposition of the ice number and mass concentration, where instead CAP dominates. However, for $q_{s,t}$, and partly q_s, large influences of the CCN concentration are visible in the variance decomposition, which may be caused by the CCN contributions to the variance of QSDEP that, in turn, may relate to the WBF process (Barthlott et al., 2022). Mazoyer et al. (2021) demonstrated in their comparison of two microphysics schemes, each treating vapor deposition differently, that depending on the scheme, latent heating along WCB trajectories is either solely dominated by deposition on ice or by deposition on ice, snow, and graupel. In our study, depositional growth of all three hydrometeor types is relevant. Since the uncertainties in CAP of ice and snow have a considerable impact on the frozen hydrometeors of the WCB cloud and latent heating by vapor deposition, using an inadequate CAP in NWP models is likely to produce forecast errors of downstream Rossby waves due to errors in latent heating within the WCB (Berman and Torn, 2022; Grams et al., 2011). Moreover, the exact prediction of latent heating associated with WCBs will be more important in the future climate, as Binder et al. (2023) suggested that in a warmer climate, latent heating of WCBs will increase due to higher atmospheric moisture contents.

Since this thesis is based on a single WCB case, our findings are not necessarily transferable to other WCB cases in a one-to-one way. For example, the location and season in which a WCB occurs is relevant to the intensity of latent heating during the WCB ascent (Madonna et al., 2014). This has to do with the sea surface temperature that influences the specific humidity and temperature in the boundary layer and therefore WCB moisture uptake and WCB ascent (Christ et al., 2025; Oertel et al., 2025b). If, in general, the WCB ascent is weaker and less latent heating occurs, parameter perturbations may not lead to a substantial variance in the WCB cloud characteristics. In particular, if less water vapor is available during the ascent, some processes such as deposition nucleation may occur to a smaller extent. Thus, perturbing the parameters may have only a minor impact on these processes, if any at all. In contrast, other processes may become more relevant. Therefore, extending the analysis to include multiple WCB cases from different locations and seasons is required to better asses the robustness and generalizability of our results.

In addition, the presented contributions of the perturbed parameters to the variance of the WCB cloud structure are only valid for the predefined parameter ranges. For different ranges, the results may be different, as in parameters that are dominant in this study may be less dominant in another study with different parameter ranges, and vice versa. In particular, if the CAP range were smaller, the impact of INP perturbations on the ice number concentration would be greater, as mentioned above.

Furthermore, the conducted simulations assume that the graupel particles are spherical and, associated with this, that CAP of a graupel particle is equal to its radius. However, graupel particles can change their shape over time due to riming, making them not spherical and therefore having another

CAP. The different CAP, which directly influences the graupel mass by depositional growth, also has implications for the associated latent heating and radiative properties of the cloud.

Another limitation is that the ICON model does not differentiate between CCN emission sources, such as air pollution or sea spray, and the associated differences in the chemical composition of CCNs. This can have consequences for the correct model representation of CCN activation, as Panicker et al. (2021) found that the number of activated CCNs at a certain supersaturation depended on the combustion emission sources they tested. In addition, the ICON model also does not consider different types of INPs which can have, analogously to CCN activation, impacts on the representation of heterogeneous ice nucleation. Paramonov et al. (2018) investigated heterogeneous ice nucleation of mineral and soil dust between 233 K and 248 K and corroborated that the chemical composition of INPs is relevant.

Moreover, we found that SAT and SST perturbations are, in general, rather unimportant for the WCB cloud structure compared to the other parameter perturbations. Again, this could be because the ranges of the other parameter perturbations are relatively large and are therefore probably more influential.

Beyond this, the composites in the applied Eulerian perspective are based on averages over many time steps and cross-sections at different latitudes, which may result in certain processes being inadequately captured or even entirely missed. For example, the double peak of the number concentration of rain stems from a double peak in the diabatic heating rate of frozen hydrometeors melting to rain. The reason for this is that the melting level occurs at different heights depending on the latitude, i.e., it is located at lower altitudes further north. If there is a sufficiently high peak in n_r at different altitudes at different latitudes, then averaging over the cross-sections from multiple latitudes does not lead to a single peak, but in this case to two peaks. This implies that for processes relying on temperature thresholds, another approach, e.g., Lagrangian diagnostics, might be more suitable.

To better visualize the temperature thresholds of processes such as melting to rain and, more importantly, ice nucleation, and to be able to perform a process-based analysis, the T-binned trajectory data are considered in the Lagrangian perspective. With that, the diabatic heating rate of frozen hydrometeors melting to rain exhibits only one peak, as expected. However, the Lagrangian perspective is generally not comparable on a one-to-one basis to the Eulerian perspective, since the composites are averaged for each PPE member over October 4 and 5. The trajectory data, on the other hand, are averaged for each PPE member over its tens of thousands of trajectories, all of which have an ascent rate of at least 600 hPa within 48 h covering multiple time steps, but do not all start their ascent at the same time. In this way, differences in variables can occur depending on the perspective. In particular, variable values can be up to one order of magnitude larger in the Lagrangian perspective, but are overall rather similar. Besides, qualitative impacts of parameter perturbations do not change with perspective. An example of this is the graupel mass concentration, where the absolute values depend on the perspective, but the qualitative influence of CAP perturbations remains the same. In general, the use of T-binned trajectory data is appropriate if the focus is on a process-based analysis.

Lastly, it should be mentioned that regarding the random forest regression models, the sample size of the training and validation datasets is relatively small. This could negatively impact the quality of the RFR model fits, which form the basis of the quantitative sensitivity analysis carried out in this thesis. Furthermore, previous studies (Wellmann et al., 2018, 2020; Oertel et al., 2025b) used Gaussian process emulation instead of RFR for sensitivity analysis. However, this study shows that the performance of RFR models is similar to or even better than GPE models, depending on the target variable. That is why RFR offers a reliable alternative to GPE.

8 Conclusion

This thesis investigated the relative importance of five uncertain model parameters, i.e., cloud condensation nucleus concentration, ice nucleating particle concentration, capacitance of ice and snow, sea surface temperature, and maximum supersaturation with respect to liquid, for the cloud structure of a WCB case in the North Atlantic simulated with the ICON model. For this sensitivity analysis, the five parameters were simultaneously and systematically perturbed in a perturbed parameter ensemble comprising 70 members. The PPE was qualitatively evaluated using Eulerian and Lagrangian diagnostics. Furthermore, variance decomposition was applied to hydrometeor mass and number concentrations, as well as microphysical process rates, based on predictions of RFR surrogate models to quantify the relative uncertainty contributions of the perturbed parameters. The most relevant impacts of the parameter perturbations are summarized in Fig. 8.1.

We find that the combined parameter perturbations generally influence the WCB cloud structure. They lead to variabilities in the mass and number concentrations of all types of hydrometeors. In particular, the mass and number concentrations of snow, ice, and cloud water increase compared to the unperturbed reference simulation. In contrast, the number and mass concentrations of rain decrease mainly. On the other hand, the mass and number concentrations of graupel do not show such a clear increase or decrease. However, an increasing trend is discernible in graupel mass and number concentrations. In addition, the maximum mass concentrations of snow, ice, and cloud water are vertically displaced.

More specifically, we find that varying the CCN concentration influences the WCB cloud structure in several ways. The first research question in this thesis was how exactly different CCN concentrations influence the WCB cloud structure. In general, the vertically integrated total hydrometeor mass and number concentration increase with increasing CCN concentration due to a dominant systematic increase in cloud water mass concentration and cloud droplet number concentration. This is observed at all levels in the Eulerian and Lagrangian perspective. The reason for this is the consistently increased CCN activation, which was directly perturbed by the scaling factor f_{CCN} and provides part of the answer to the second research question, namely, which process rates account for the observed changes in the cloud structure. In contrast to cloud water, the rain mass concentration decreases with increasing CCN concentrations at all levels in both perspectives. This occurs because the mean size of cloud droplets is reduced, which decreases the conversion of q_{c} to q_{r}. In addition, a reduction of the graupel mass and number concentration occurs at all levels. We attribute this to a decrease in the riming rate caused by smaller mean cloud droplet sizes. Furthermore, the liquid fraction increases in the mixed-phase region below 6 km and below the melting level. Variance decomposition shows that the CCN concentration is indeed the dominant

contributor to most of the variance in the (vertically integrated) number and mass concentrations of rain and cloud water. However, only between 2.4 km and 5.5 km or between 275 K and 255 K is the cloud water mass concentration most sensitive to CCN perturbations. Higher up, CAP and INP perturbations become more relevant to cloud water mass concentrations. The riming rate is also only determined by CCNs between 2.4 km and 2.9 km or between 275 K and 267 K and the variance decomposition of the (vertically integrated) graupel mass concentration and (vertically integrated) number concentration reveal vanishingly small CCN influences.

The third research question addressed how the impacts of CCN perturbations compare to the other parameter perturbations. In fact, the influence of CCN perturbations on the WCB cloud structure is considerably larger compared to INP perturbations. However, there are two main INP impacts. First, increases in immersion freezing and deposition nucleation rates are observed, which occur with increasing INP concentrations. Second, an increasing ice number concentration with decreasing INP concentrations occurs at all levels as a result of the increased rate of homogeneous ice nucleation of water vapor at temperatures below 235 K. As immersion freezing and deposition nucleation rates are directly perturbed by the scaling factor f_{INP}, their variance decomposition shows, as expected, that the INP concentration is the dominant contributor. Although also perturbed by f_{INP}, the freezing rate exhibits only minor INP influences and is instead dominated by CCNs, as CCNs influence the raindrop size distribution. The influence of INPs on the variance of ice number concentrations is overshadowed by the influence of CAP, which is also reflected in the variance decomposition of the homogeneous ice nucleation rate of water vapor. Thus, impacts of INPs are relevant for ice nucleation through immersion freezing and deposition nucleation, but in the end, ice number concentrations are determined primarily by CAP and only to a small extent by INPs.

In general, the importance of CAP perturbations for the WCB cloud structure is comparable in magnitude to that of CCNs. The most pronounced effect of CAP perturbations is the systematic increase in graupel mass and number concentration at all levels when CAP of ice and snow is reduced. This increase in mass concentration is primarily driven by enhanced depositional growth of graupel due to the greater availability of water vapor, as the depositional growth of ice and snow is reduced by the scaling factor f_{CAP}. Furthermore, increased riming further contributes to graupel formation and growth. In addition to ice, (vertically integrated) number concentrations of snow also increase with decreasing CAP, mainly due to enhanced homogeneous ice nucleation of water vapor. Variance decomposition confirms that the number and mass concentrations of graupel, ice, and snow, as well as their depositional growth rates, are predominantly influenced by CAP. An exception is the vertically integrated snow mass concentration, which is more strongly affected by CCN perturbations. Furthermore, the depositional growth rate of snow is markedly shaped by CCNs at higher levels, hinting at the influence of the Wegener-Bergeron-Findeisen process.

As the cloud structure near the cloud top influences radiative properties, we find a variance in the radiation balance at TOA. With regard to the fourth research question how the radiation balance at TOA is affected by parameter perturbations, the results show that the balance of longwave radiation is primarily governed by CAP perturbations. Reducing CAP of ice and snow decreases the net longwave radiation at TOA since less longwave radiation is emitted at the cloud top due to lower cloud top temperatures. This vertical displacement of ice to lower temperatures is caused

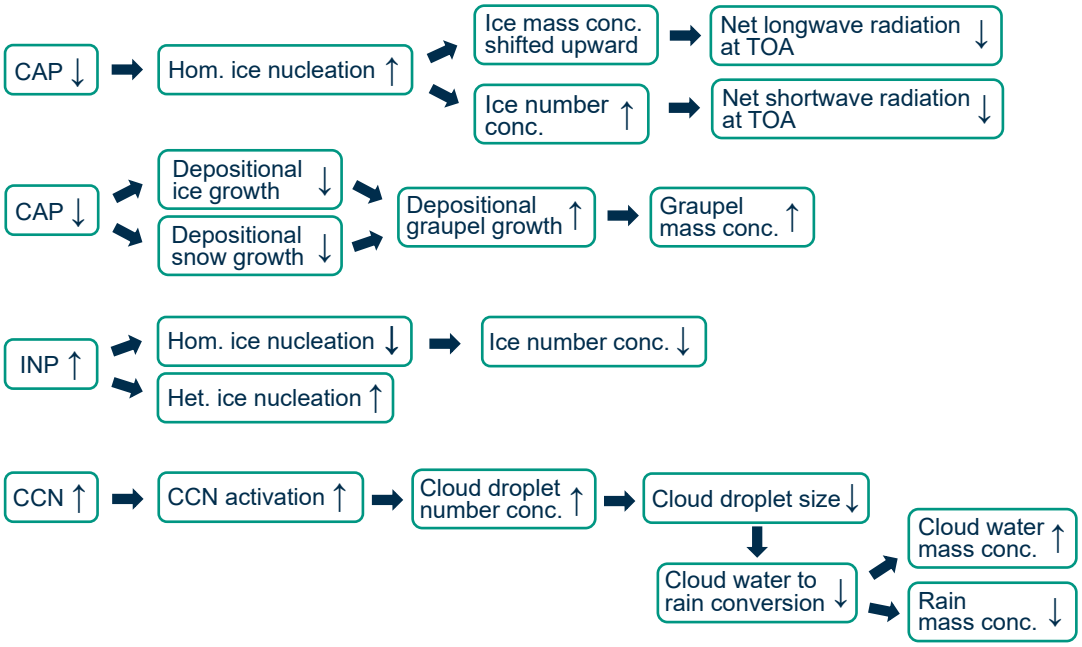

Figure 8.1: Summary of the most important impacts of the parameter perturbations on the WCB cloud structure. Arrows pointing upward indicate an increase, whereas arrows pointing downward indicate a decrease.

by increased homogeneous ice nucleation of water vapor. To a lesser extent, the net shortwave radiation at TOA is reduced as well for lower CAP, which is attributed to an increase in the number concentrations of all frozen hydrometeors, especially ice, leading to a higher cloud optical depth. The variance decomposition of the net longwave radiation verifies the dominant role of CAP throughout the warm sector, whereas for the net shortwave radiation, the impact of CAP is most dominant near the cold front. In addition, CCN and SST perturbations also play a role for the net shortwave radiation further east in the warm sector, which may also be related to a higher cloud optical depth.

In summary, CCN concentrations predominantly influence the number and mass concentration of liquid hydrometeors in the cloud, while CAP influences the number and mass concentration of the frozen hydrometeors plus the net longwave radiation at TOA. Specifically, CAP overshadows the impact of INPs on immersion freezing and deposition nucleation with its influence on the number and mass concentration of frozen hydrometeors. The net shortwave radiation at TOA is influenced by CCNs, SST and CAP. Aside from that, SST and SAT perturbations are in general negligible for the cloud structure compared to the other perturbations. In conclusion, CCN and CAP perturbations are most relevant to the WCB cloud properties.

Outlook

Based on the results and limitations of this thesis, future research could aim to consider different types of CCNs and INPs, which could be done with ICON-ART (Schröter et al., 2018). As the amount of CCNs strongly influences liquid hydrometeors and the amount of INPs influences the heterogeneous ice nucleation, the question arises whether this would still apply to the same degree if differences in the chemical composition of CCNs and INPs were introduced. Furthermore, the CAPs of all frozen hydrometeors need better constraints to improve the model representation and predictability of latent heating by vapor deposition, which has implications for the predictability of large-scale circulation. In addition, there is potential to improve the performance of the RFR surrogate models, e.g., by either expanding the Grid Search to cover a wider range of hyperparameters or by using larger sample sizes of training and validation datasets. Lastly, this thesis focuses on the influences of parameter perturbations on the cloud structure of one WCB case. It remains an open question whether these influences hold for other WCB cases. In particular, are other cases affected to a similar extent? If not, what are the reasons for the differences?

A Appendix

A.1 Metrics

The mean absolute error (MAE) is given by

$$\text{MAE} = \frac{1}{N}\sum_{i=0}^{N-1} y_i - \hat{y}_i\,, \tag{A.1}$$

with the total number of data points N, the true value y_i of the i-th sample and the predicted value $\hat{y}_i$ (Pedregosa et al., 2011). Accordingly, the mean squared error (MSE) is calculated with

$$\text{MSE} = \frac{1}{N}\sum_{i=0}^{N-1} (y_i - \hat{y}_i)^2\,, \tag{A.2}$$

and the root mean squared error (RMSE) with

$$\text{RMSE} = \sqrt{\frac{1}{N}\sum_{i=0}^{N-1} (y_i - \hat{y}_i)^2}\,. \tag{A.3}$$

Note that the root mean squared error has the same units as the target variable.

The R^2 score (coefficient of determination) is defined as

$$R^2 = 1 - \frac{\sum_{i=1}^{N}(y_i - \hat{y}_i)^2}{\sum_{i=1}^{N}(y_i - \bar{y})^2}\,, \tag{A.4}$$

with the average of the true values $\bar{y} = \frac{1}{N}\sum_{i=1}^{N} y_i$. This score is a measure of the goodness of a fit. The optimal value of R^2 is 1, which means that $y_i = \hat{y}_i$, that is, the predicted values fit perfectly the true values. If $R^2 = 0$, the model can only predict the average of the true values, which means that $\hat{y}_i = \bar{y}$. Thus, the model has no predictive power. In addition, R^2 can become infinitely negative, resulting in misleading predictions.

A.2 Figures

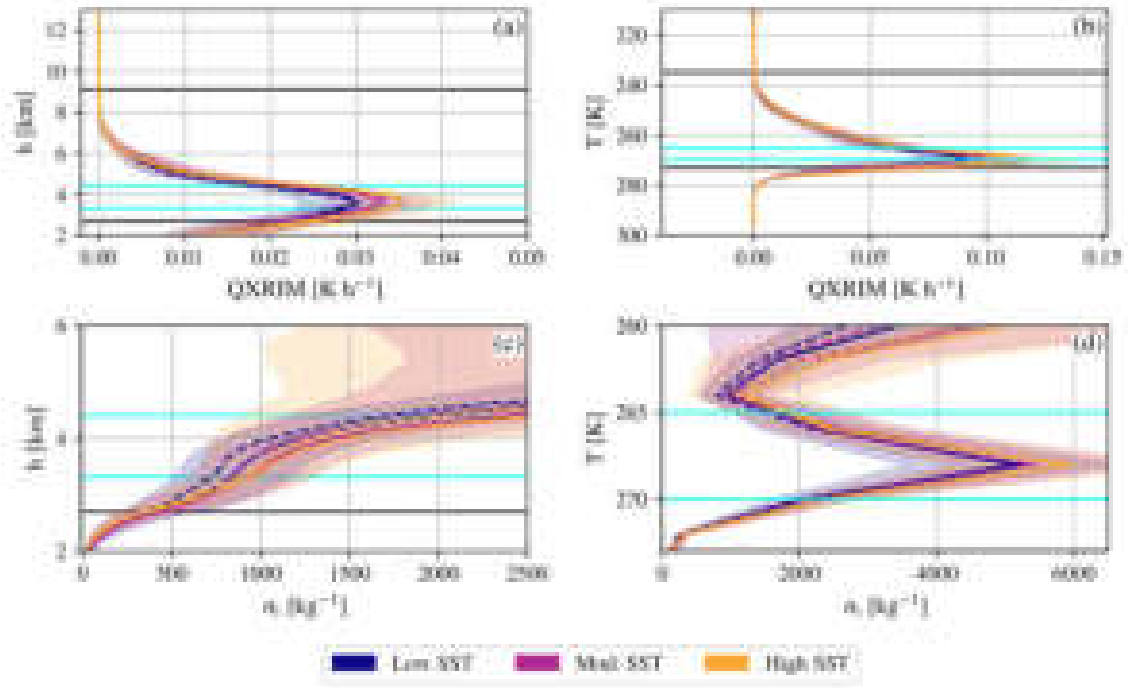

Figure A.1: As Fig. 5.3 but for low (purple), moderate (magenta), and high (orange) sea surface temperature (SST) perturbations. **(a)**, **(b)** Diabatic heating rate of riming (QXRIM, in $\mathrm{K\,h^{-1}}$) and **(c)**, **(d)** ice number concentration (n_i, in $\mathrm{kg^{-1}}$). Cyan horizontal lines mark the level of $-3\,^\circ\mathrm{C}$ and $-8\,^\circ\mathrm{C}$.

A.3 Tables

Table A.1: Mean scaling factors f of all parameter perturbations per subset. Subsets are sorted by each perturbed parameter in ascending order.

sorted by	subset	f_{CCN}	f_{INP}	f_{CAP}	f_{SST}	f_{SAT}
CCN	low	3.664	1.808	0.542	-0.024	0.040
CCN	moderate	10.208	2.403	0.584	0.406	0.056
CCN	high	16.661	3.470	0.654	-0.285	0.055
INP	low	9.778	0.048	0.611	-0.229	0.047
INP	moderate	10.007	0.648	0.542	0.336	0.047
INP	high	10.756	7.061	0.628	-0.007	0.057
CAP	low	8.573	2.464	0.327	-0.113	0.047
CAP	moderate	10.543	1.260	0.593	0.322	0.048
CAP	high	11.402	4.007	0.859	-0.109	0.055
SST	low	10.176	2.489	0.619	-1.328	0.054
SST	moderate	10.213	1.722	0.579	0.058	0.042
SST	high	10.143	3.500	0.581	1.382	0.055
SAT	low	8.907	2.576	0.559	0.022	0.017
SAT	moderate	10.288	1.346	0.584	0.000	0.051
SAT	high	11.335	3.804	0.635	0.092	0.084

Table A.2: Values of the mean altitudes $\overline{h}$, temperatures $\overline{T}$, and relative longitudes $\overline{\text{rel. lon}}$ used for random forest regression models. Models are trained with data averaged over a number of height levels N_{h}, T-bins N_{T}, and rel. lon steps N_{lon} that cover different height levels, temperature, and relative longitude ranges.

N_{h}	$\overline{h}$ [km]	h range [km]	N_{T}	$\overline{T}$ [K]	T range [K]	N_{lon}	$\overline{\text{rel. lon}}$ [°]	Rel. lon range [°]
3	9.3	9.0 - 9.5	4	233	237 - 229	10	0.45	0.0 - 0.9
3	8.2	7.9 - 8.4	4	241	245 - 237	10	1.45	1.0 - 1.9
4	6.6	6.3 - 7.0	4	251	255 - 247	10	2.45	2.0 - 2.9
3	5.2	4.0 - 5.0	4	259	263 - 255	10	3.45	3.0 - 3.9
5	2.6	2.4 - 2.9	4	271	275 - 267	10	4.45	4.0 - 4.9
						10	5.45	5.0 - 5.9
						10	6.45	6.0 - 6.9
						10	7.45	7.0 - 7.9

Table A.3: Hyperparameter values used for training the random forest regression models and respective root mean squared error (RMSE) and R^2 for various variables and mean altitudes $\overline{h}$ in the Eulerian perspective. Hyperparameter tuning is performed with the Grid Search algorithm.

Variable	$\overline{h}$ [km]	N_{tree}	N_{s}	N_{feat}	RMSE	R^2
q_{c}	8.2	200	2	4	7.62×10^{-4}	0.84
q_{c}	6.6	100	2	3	4.71×10^{-3}	0.79
q_{c}	5.2	500	4	3	1.86×10^{-2}	0.63
q_{c}	2.6	250	2	5	1.36×10^{-2}	0.97
q_{r}	6.6	200	3	5	5.62×10^{-5}	0.76
q_{r}	5.2	100	3	5	1.47×10^{-4}	0.87
q_{r}	2.6	250	2	3	1.29×10^{-3}	0.79
q_{i}	9.3	500	2	4	3.55×10^{-3}	0.78
q_{i}	8.2	150	2	5	3.36×10^{-3}	0.85

Continuation of Table A.3

Variable	$\overline{h}$ [km]	N_{tree}	N_{s}	N_{feat}	RMSE	R^2
q_{i}	6.6	500	2	3	1.31×10^{-3}	0.80
q_{i}	5.2	500	2	4	2.39×10^{-3}	0.80
q_{i}	2.6	150	3	5	3.40×10^{-4}	0.90
q_{s}	8.2	150	3	4	1.14×10^{-3}	0.73
q_{s}	6.6	200	2	4	4.31×10^{-3}	0.73
q_{s}	5.2	500	3	5	5.79×10^{-3}	0.69
q_{s}	2.6	150	2	4	3.17×10^{-3}	0.89
q_{g}	6.6	200	3	3	1.58×10^{-4}	0.85
q_{g}	5.2	500	2	5	7.69×10^{-4}	0.95
q_{g}	2.6	150	2	4	2.71×10^{-3}	0.95
n_{c}	8.2	100	2	5	1.63×10^{6}	0.69
n_{c}	6.6	500	4	3	1.34×10^{7}	0.54
n_{c}	5.2	200	2	4	3.27×10^{7}	0.88
n_{c}	2.6	150	3	5	2.32×10^{7}	0.99
n_{r}	6.6	100	3	5	7.51×10^{1}	0.80
n_{r}	2.6	500	2	5	2.34×10^{2}	0.83
n_{i}	9.3	150	2	4	2.42×10^{5}	0.73
n_{i}	8.2	150	2	4	1.47×10^{5}	0.75
n_{i}	6.6	150	2	4	3.40×10^{4}	0.59
n_{i}	5.2	500	2	2	3.54×10^{3}	0.60
n_{i}	2.6	100	2	3	5.37×10^{1}	0.93
n_{s}	9.3	100	2	5	1.76×10^{2}	0.76
n_{s}	8.2	100	2	4	8.79×10^{2}	0.74
n_{s}	6.6	100	2	5	1.38×10^{3}	0.77
n_{s}	5.2	150	2	5	7.35×10^{2}	0.80
n_{s}	2.6	150	3	4	4.39×10^{1}	0.82
n_{g}	6.6	500	2	3	4.49	0.89
n_{g}	5.2	250	2	5	1.05×10^{1}	0.96
n_{g}	2.6	100	3	4	2.83×10^{1}	0.94
QCNUC	9.3	100	3	5	1.48×10^{-4}	0.64
QCNUC	8.2	100	2	4	9.14×10^{-4}	0.68
QCNUC	6.6	100	4	3	2.98×10^{-3}	0.70
QCNUC	5.2	100	2	5	1.42×10^{-3}	0.99
QCNUC	2.6	150	3	5	5.09×10^{-4}	0.99
QIHOMHET	9.3	100	2	3	1.61×10^{-3}	0.73
QIHOMHET	6.6	500	2	2	5.60×10^{-7}	0.81
QCFRZ	8.2	100	2	5	3.86×10^{-6}	0.79
QRFRZ	6.6	100	4	5	1.61×10^{-6}	0.88
QRFRZ	5.2	200	2	5	3.41×10^{-6}	0.78
QSDEP	8.2	500	3	5	3.13×10^{-3}	0.73
QSDEP	6.6	500	2	5	1.97×10^{-2}	0.62
QSDEP	5.2	150	4	5	2.63×10^{-2}	0.88
QSDEP	2.6	100	4	5	7.31×10^{-3}	0.92
QIDEP	8.2	150	2	5	4.93×10^{-3}	0.60
QIDEP	6.6	500	5	5	1.33×10^{-2}	0.81

Continuation of Table A.3						
Variable	$\overline{h}$ [km]	N_{tree}	N_{s}	N_{feat}	RMSE	R^2
QIDEP	5.2	250	3	5	1.96×10^{-2}	0.91
QIDEP	2.6	500	2	5	3.13×10^{-3}	0.85
QGDEP	6.6	100	2	3	2.44×10^{-3}	0.87
QGDEP	5.2	500	2	5	5.08×10^{-3}	0.97
QGDEP	2.6	150	3	5	4.82×10^{-3}	0.80
QXRIM	6.6	200	4	4	2.77×10^{-4}	0.80
QXRIM	5.2	200	2	4	1.22×10^{-3}	0.91
QXRIM	2.6	250	4	5	1.73×10^{-3}	0.94
RADSW	9.3	500	2	5	1.95×10^{-3}	0.73
RADSW	8.2	250	3	5	1.50×10^{-3}	0.80
RADSW	6.6	100	3	5	1.40×10^{-3}	0.74
RADSW	5.2	100	3	4	7.99×10^{-4}	0.88
RADSW	2.6	100	3	5	2.93×10^{-4}	0.79
RADLW	9.3	500	3	4	3.52×10^{-3}	0.88
RADLW	8.2	100	4	5	4.50×10^{-3}	0.86
RADLW	6.6	500	4	5	5.23×10^{-3}	0.71
RADLW	5.2	500	2	4	4.18×10^{-3}	0.83
RADLW	2.6	100	3	5	1.16×10^{-3}	0.87
End of Table						

Table A.4: Hyperparameter values used for training the random forest regression models and respective root mean squared error (RMSE) and R^2 for various variables and mean temperatures $\overline{T}$ in the Lagrangian perspective. Hyperparameter tuning is performed with the Grid Search algorithm.

Variable	$\overline{T}$ [K]	N_{tree}	N_{s}	N_{feat}	RMSE	R^2
q_{c}	241	200	2	5	4.88×10^{-4}	0.93
q_{c}	251	150	3	5	9.36×10^{-3}	0.82
q_{c}	259	500	2	2	3.86×10^{-2}	0.71
q_{c}	271	200	4	5	2.97×10^{-2}	0.98
q_{r}	251	100	2	5	1.35×10^{-4}	0.74
q_{r}	259	200	3	4	6.84×10^{-4}	0.82
q_{r}	271	100	2	3	9.77×10^{-4}	0.90
q_{i}	233	150	2	4	1.63×10^{-3}	0.83
q_{i}	241	150	3	5	2.22×10^{-3}	0.89
q_{i}	251	500	3	2	1.38×10^{-3}	0.85
q_{i}	259	150	2	5	2.00×10^{-3}	0.96
q_{i}	271	100	2	5	5.92×10^{-4}	0.95
q_{s}	241	500	3	3	4.56×10^{-4}	0.79
q_{s}	251	100	2	4	3.00×10^{-3}	0.76
q_{s}	259	100	2	4	6.30×10^{-3}	0.71
q_{s}	271	150	3	3	7.82×10^{-3}	0.88
q_{g}	241	250	3	5	1.43×10^{-4}	0.74
q_{g}	251	250	3	5	9.49×10^{-4}	0.92
q_{g}	259	150	3	5	2.57×10^{-3}	0.91

Continuation of Table A.4

Variable	$\overline{T}$ [K]	N_{tree}	N_{s}	N_{feat}	RMSE	R^2
q_{g}	271	100	4	5	7.83×10^{-3}	0.93
n_{c}	233	150	3	5	5.00×10^{4}	0.71
n_{c}	241	100	2	4	2.16×10^{6}	0.70
n_{c}	251	150	5	3	2.25×10^{7}	0.65
n_{c}	259	250	2	4	3.84×10^{7}	0.96
n_{c}	271	100	3	5	2.75×10^{7}	1.00
n_{i}	233	200	2	4	3.10×10^{5}	0.78
n_{i}	241	100	2	4	1.58×10^{5}	0.85
n_{i}	251	150	3	4	2.08×10^{4}	0.82
n_{i}	259	500	2	2	2.51×10^{3}	0.61
n_{i}	271	100	2	4	1.60×10^{2}	0.92
n_{s}	233	150	3	4	2.09×10^{1}	0.90
n_{s}	241	150	2	5	2.37×10^{2}	0.91
n_{s}	251	250	2	5	7.06×10^{2}	0.90
n_{s}	259	250	2	5	5.33×10^{2}	0.87
n_{s}	271	100	2	4	2.98×10^{1}	0.87
QCNUC	241	100	3	2	1.62×10^{-3}	0.65
QCNUC	251	250	5	4	4.04×10^{-3}	0.91
QCNUC	259	150	2	5	1.05×10^{-2}	0.89
QCNUC	271	100	2	5	1.06×10^{-3}	0.97
QIHOMHET	233	250	2	4	2.91×10^{-4}	0.90
QIHOMHET	251	500	5	2	3.69×10^{-7}	0.89
QIHOMHET	259	500	5	2	1.10×10^{-8}	0.92
QCFRZ	233	100	3	5	3.38×10^{-6}	0.74
QCFRZ	241	100	2	5	8.24×10^{-7}	0.66
QRFRZ	251	150	2	5	7.12×10^{-6}	0.87
QRFRZ	259	100	2	5	6.94×10^{-6}	0.91
QRFRZ	271	100	2	3	7.22×10^{-8}	0.88
QSDEP	241	100	3	4	4.99×10^{-3}	0.81
QSDEP	251	150	4	5	1.56×10^{-2}	0.94
QSDEP	259	150	2	5	8.89×10^{-2}	0.83
QSDEP	271	150	2	5	2.67×10^{-2}	0.89
QIDEP	241	250	2	4	6.62×10^{-3}	0.68
QIDEP	251	500	3	4	2.76×10^{-2}	0.89
QIDEP	259	250	2	5	2.90×10^{-2}	0.95
QIDEP	271	100	2	4	7.30×10^{-3}	0.95
QGDEP	241	150	2	5	3.31×10^{-3}	0.89
QGDEP	251	100	4	5	9.43×10^{-3}	0.95
QGDEP	259	200	2	5	1.72×10^{-2}	0.95
QGDEP	271	150	2	4	1.28×10^{-2}	0.93
QXRIM	251	150	2	5	1.75×10^{-3}	0.76
QXRIM	259	100	3	3	2.86×10^{-3}	0.83
QXRIM	271	100	2	5	6.57×10^{-3}	0.90

End of Table

Table A.5: Hyperparameter values used for training the random forest regression models and respective root mean squared error (RMSE) and R^2 for various variables and mean relative longitudes $\overline{\text{rel. lon}}$ in the Eulerian perspective. Hyperparameter tuning is performed with the Grid Search algorithm.

Variable	$\overline{\text{rel. lon}}$ [°]	N_{tree}	N_{s}	N_{feat}	RMSE	R^2
$q_{\text{c,t}}$	0.45	250	2	3	5.78×10^{-2}	0.91
$q_{\text{c,t}}$	1.45	250	3	4	6.54×10^{-2}	0.93
$q_{\text{c,t}}$	2.45	200	4	5	7.85×10^{-2}	0.95
$q_{\text{c,t}}$	3.45	500	3	4	1.01×10^{-1}	0.90
$q_{\text{c,t}}$	4.45	200	2	3	1.11×10^{-1}	0.73
$q_{\text{c,t}}$	5.45	100	2	5	6.39×10^{-2}	0.58
$q_{\text{c,t}}$	6.45	200	2	5	1.76×10^{-2}	0.70
$q_{\text{c,t}}$	7.45	100	5	4	1.34×10^{-2}	0.65
$q_{\text{r,t}}$	0.45	500	4	5	6.86×10^{-3}	0.86
$q_{\text{r,t}}$	1.45	100	2	4	8.34×10^{-3}	0.89
$q_{\text{r,t}}$	2.45	250	3	4	1.16×10^{-2}	0.86
$q_{\text{r,t}}$	3.45	150	4	5	1.25×10^{-2}	0.80
$q_{\text{r,t}}$	4.45	250	3	3	7.80×10^{-3}	0.74
$q_{\text{r,t}}$	5.45	150	5	2	4.22×10^{-3}	0.68
$q_{\text{r,t}}$	7.45	150	5	5	1.31×10^{-3}	0.58
$q_{\text{i,t}}$	0.45	150	4	5	4.64×10^{-3}	0.77
$q_{\text{i,t}}$	1.45	500	3	2	4.84×10^{-3}	0.74
$q_{\text{i,t}}$	2.45	500	2	5	5.46×10^{-3}	0.65
$q_{\text{i,t}}$	3.45	100	5	5	4.70×10^{-3}	0.63
$q_{\text{i,t}}$	4.45	100	3	4	3.10×10^{-3}	0.77
$q_{\text{i,t}}$	5.45	150	3	1	3.90×10^{-3}	0.55
$q_{\text{i,t}}$	6.45	150	2	2	4.18×10^{-3}	0.67
$q_{\text{i,t}}$	7.45	500	2	3	3.67×10^{-3}	0.59
$q_{\text{s,t}}$	0.45	500	5	4	1.02×10^{-2}	0.68
$q_{\text{s,t}}$	1.45	200	2	5	2.47×10^{-2}	0.71
$q_{\text{s,t}}$	2.45	150	2	5	2.27×10^{-2}	0.64
$q_{\text{s,t}}$	4.45	500	2	5	1.51×10^{-2}	0.59
$q_{\text{s,t}}$	5.45	500	3	5	1.43×10^{-2}	0.59
$q_{\text{s,t}}$	6.45	150	5	4	9.36×10^{-3}	0.67
$q_{\text{s,t}}$	7.45	250	2	4	4.59×10^{-3}	0.62
$q_{\text{g,t}}$	0.45	100	3	3	1.09×10^{-2}	0.82
$q_{\text{g,t}}$	1.45	100	3	3	1.15×10^{-2}	0.93
$q_{\text{g,t}}$	2.45	100	2	3	1.22×10^{-2}	0.93
$q_{\text{g,t}}$	3.45	150	2	4	1.11×10^{-2}	0.92
$q_{\text{g,t}}$	4.45	200	3	4	1.10×10^{-2}	0.91
$q_{\text{g,t}}$	5.45	500	2	3	7.80×10^{-3}	0.86
$q_{\text{g,t}}$	6.45	500	2	4	2.45×10^{-3}	0.91
$q_{\text{g,t}}$	7.45	150	2	5	1.63×10^{-3}	0.83
$n_{\text{c,t}}$	0.45	200	2	4	1.19×10^{11}	0.97
$n_{\text{c,t}}$	1.45	200	3	5	1.21×10^{11}	0.99
$n_{\text{c,t}}$	2.45	100	2	5	1.62×10^{11}	0.99
$n_{\text{c,t}}$	3.45	150	3	4	2.05×10^{11}	0.97

Continuation of Table A.5

Variable	$\overline{\text{rel. lon}}$ [°]	N_{tree}	N_{s}	N_{feat}	RMSE	R^2
$n_{\text{c,t}}$	4.45	200	4	4	2.16×10^{11}	0.92
$n_{\text{c,t}}$	5.45	500	2	3	1.53×10^{11}	0.83
$n_{\text{c,t}}$	6.45	150	3	4	4.80×10^{10}	0.93
$n_{\text{c,t}}$	7.45	250	2	5	2.55×10^{10}	0.97
$n_{\text{r,t}}$	0.45	500	3	5	7.12×10^{5}	0.89
$n_{\text{r,t}}$	1.45	100	2	4	1.37×10^{6}	0.67
$n_{\text{r,t}}$	2.45	100	2	4	6.03×10^{5}	0.93
$n_{\text{r,t}}$	3.45	250	3	4	7.66×10^{5}	0.85
$n_{\text{r,t}}$	4.45	200	5	4	6.20×10^{5}	0.87
$n_{\text{r,t}}$	5.45	500	4	5	5.98×10^{5}	0.89
$n_{\text{r,t}}$	6.45	100	4	5	5.56×10^{5}	0.86
$n_{\text{r,t}}$	7.45	100	5	5	2.07×10^{5}	0.98
$n_{\text{i,t}}$	0.45	150	2	4	2.97×10^{8}	0.60
$n_{\text{i,t}}$	1.45	150	2	4	2.98×10^{8}	0.73
$n_{\text{i,t}}$	2.45	150	3	4	2.99×10^{8}	0.79
$n_{\text{i,t}}$	3.45	100	2	5	3.58×10^{8}	0.72
$n_{\text{i,t}}$	4.45	500	2	4	4.37×10^{8}	0.56
$n_{\text{i,t}}$	5.45	150	2	5	3.18×10^{8}	0.65
$n_{\text{i,t}}$	6.45	150	2	5	1.88×10^{8}	0.60
$n_{\text{i,t}}$	7.45	150	2	3	9.62×10^{7}	0.60
$n_{\text{s,t}}$	0.45	150	2	5	2.19×10^{6}	0.85
$n_{\text{s,t}}$	1.45	150	2	4	3.48×10^{6}	0.83
$n_{\text{s,t}}$	2.45	100	2	5	3.29×10^{6}	0.81
$n_{\text{s,t}}$	3.45	250	2	5	3.39×10^{6}	0.74
$n_{\text{s,t}}$	4.45	500	2	4	3.14×10^{6}	0.68
$n_{\text{s,t}}$	5.45	500	2	5	2.17×10^{6}	0.71
$n_{\text{s,t}}$	6.45	200	2	4	1.35×10^{6}	0.77
$n_{\text{s,t}}$	7.45	500	2	4	9.43×10^{5}	0.81
$n_{\text{g,t}}$	0.45	150	2	5	1.02×10^{5}	0.90
$n_{\text{g,t}}$	1.45	100	2	3	1.01×10^{5}	0.93
$n_{\text{g,t}}$	2.45	100	3	4	1.21×10^{5}	0.93
$n_{\text{g,t}}$	3.45	100	3	4	1.24×10^{5}	0.92
$n_{\text{g,t}}$	4.45	100	3	5	1.14×10^{5}	0.87
$n_{\text{g,t}}$	5.45	100	3	5	6.64×10^{4}	0.88
$n_{\text{g,t}}$	6.45	100	3	4	3.96×10^{4}	0.91
$n_{\text{g,t}}$	7.45	500	3	4	2.41×10^{4}	0.88
SW	0.45	150	2	2	1.70	0.69
SW	3.45	150	3	5	1.64	0.62
SW	4.45	250	3	3	2.68	0.59
SW	5.45	500	2	5	2.94	0.75
SW	6.45	200	2	4	2.35	0.75
SW	7.45	100	2	4	2.46	0.62
LW	0.45	100	2	3	8.42×10^{-1}	0.81
LW	1.45	150	3	4	1.00	0.77
LW	2.45	150	2	5	9.04×10^{-1}	0.82

Continuation of Table A.5

Variable	$\overline{\text{rel. lon}}$ [°]	N_{tree}	N_{s}	N_{feat}	RMSE	R^2
LW	3.45	500	3	5	9.46×10^{-1}	0.87
LW	4.45	500	2	5	8.53×10^{-1}	0.86
LW	5.45	500	5	4	1.08	0.71
LW	6.45	500	5	4	1.24	0.70
LW	7.45	500	3	3	1.29	0.81

End of Table

Abbreviations

CAP	capacitance
CCN	cloud condensation nucleus
COD	cloud optical depth
CRE	cloud radiative effect
DEPNUC	diabatic heating rate of deposition nucleation
ETC	extratropical cyclone
FAST	Fourier amplitude sensitivity test
GPE	Gaussian process emulation
HOMNUC	diabatic heating rate of homogeneous ice nucleation of water vapor
ICON	ICOsahedral Nonhydrostatic
IMFRZ	diabatic heating rate of immersion freezing
INP	ice nucleating particle
IOP	intensive observation period
IWC	ice water content
LW	Net longwave radiation at the top of atmosphere
LWC	liquid water content
LWP	liquid water path
LWCRE	longwave cloud radiative effect
MAE	mean absolute error
MLR	multiple linear regression
MSE	mean squared error

NAWDEX North Atlantic Waveguide and Downstream Impact Experiment

NWP numerical weather prediction

OLR outgoing longwave radiation

PPE perturbed parameter ensemble

PSD particle size distribution

PV potential vorticity

QCFRZ diabatic heating rate of freezing of cloud droplet

QCNUC diabatic heating rate of cloud droplet activation

QGDEP diabatic heating rate of depositional growth of graupel

QIDEP diabatic heating rate of depositional growth of ice

QIHOMHET diabatic heating rate of heterogeneous and homogeneous ice nucleation

QRFRZ diabatic heating rate of freezing of rain

QSDEP diabatic heating rate of depositional growth of snow

QXRIM diabatic heating rate of riming

RADLW longwave cooling rate

RADSW shortwave heating rate

REF unperturbed reference simulation

RFR random forest regression

RMSE root mean squared error

SAT maximum supersaturation with respect to liquid

SATAD2 second saturation adjustment

SIP secondary ice production

SST sea surface temperature

SW Net shortwave radiation at the top of atmosphere

SWCRE shortwave cloud radiative effect

TOA top of atmosphere

TWP total water path

WBF Wegener-Bergeron-Findeisen

WCB warm conveyor belt

Bibliography

Barthlott, C., A. Zarboo, T. Matsunobu, and C. Keil, 2022: Importance of aerosols and shape of the cloud droplet size distribution for convective clouds and precipitation. *Atmospheric Chemistry and Physics*, **22 (3)**, 2153–2172, https://doi.org/10.5194/acp-22-2153-2022.

Berman, J. D., and R. D. Torn, 2022: The Sensitivity of Downstream Ridge Building Forecasts to Upstream Warm Conveyor Belt Forecast Uncertainty Using MPAS. *Monthly Weather Review*, **150 (10)**, 2573–2592, https://doi.org/10.1175/MWR-D-21-0048.1.

Bigg, E. K., 1953: The formation of atmospheric ice crystals by the freezing of droplets. *Quarterly Journal of the Royal Meteorological Society*, **79 (342)**, 510–519, https://doi.org/10.1002/qj.49707934207.

Binder, H., M. Boettcher, H. Joos, and H. Wernli, 2016: The Role of Warm Conveyor Belts for the Intensification of Extratropical Cyclones in Northern Hemisphere Winter. *Journal of the Atmospheric Sciences*, **73 (10)**, 3997–4020, https://doi.org/10.1175/JAS-D-15-0302.1, publisher: American Meteorological Society Section: Journal of the Atmospheric Sciences.

Binder, H., H. Joos, M. Sprenger, and H. Wernli, 2023: Warm conveyor belts in present-day and future climate simulations – Part 2: Role of potential vorticity production for cyclone intensification. *Weather and Climate Dynamics*, **4 (1)**, 19–37, https://doi.org/10.5194/wcd-4-19-2023.

Boettcher, M., and H. Wernli, 2013: A 10-yr Climatology of Diabatic Rossby Waves in the Northern Hemisphere. *Monthly Weather Review*, **141 (3)**, 1139–1154, https://doi.org/10.1175/MWR-D-12-00012.1.

Breiman, L., 2001: Random Forests. *Machine Learning*, **45 (1)**, 5–32, https://doi.org/10.1023/A:1010933404324.

Christ, S., M. Wenta, C. M. Grams, and A. Oertel, 2025: From sea to sky: understanding the sea surface temperature impact on an atmospheric blocking event using sensitivity experiments with the ICOsahedral Nonhydrostatic (ICON) model. *Weather and Climate Dynamics*, **6 (1)**, 17–42, https://doi.org/10.5194/wcd-6-17-2025.

Durran, D. R., 2010: *Numerical Methods for Fluid Dynamics: With Applications to Geophysics*. 2nd ed., No. 32, Texts in Applied Mathematics, Springer New York, New York, NY, https://doi.org/10.1007/978-1-4419-6412-0.

Eckhardt, S., A. Stohl, H. Wernli, P. James, C. Forster, and N. Spichtinger, 2004: A 15-Year Climatology of Warm Conveyor Belts. *Journal of Climate*, **17 (1)**, 218–237, https://doi.org/10.1175/1520-0442(2004)017<0218:AYCOWC>2.0.CO;2.

Field, P. R., and Coauthors, 2017: Secondary Ice Production: Current State of the Science and Recommendations for the Future. *Meteorological Monographs*, **58 (1)**, 7.1–7.20, https://doi.org/10.1175/AMSMONOGRAPHS-D-16-0014.1.

Forbes, R. M., and P. A. Clark, 2003: Sensitivity of extratropical cyclone mesoscale structure to the parametrization of ice microphysical processes. *Quarterly Journal of the Royal Meteorological Society*, **129 (589)**, 1123–1148, https://doi.org/10.1256/qj.01.171.

Grams, C. M., and Coauthors, 2011: The key role of diabatic processes in modifying the upper-tropospheric wave guide: a North Atlantic case-study. *Quarterly Journal of the Royal Meteorological Society*, **137 (661)**, 2174–2193, https://doi.org/10.1002/qj.891.

Hande, L. B., C. Engler, C. Hoose, and I. Tegen, 2015: Seasonal variability of Saharan desert dust and ice nucleating particles over Europe. *Atmospheric Chemistry and Physics*, **15 (8)**, 4389–4397, https://doi.org/10.5194/acp-15-4389-2015.

Hande, L. B., C. Engler, C. Hoose, and I. Tegen, 2016: Parameterizing cloud condensation nuclei concentrations during HOPE. *Atmospheric Chemistry and Physics*, **16 (18)**, 12 059–12 079, https://doi.org/10.5194/acp-16-12059-2016.

Herman, J., and W. Usher, 2017: SALib: An open-source Python library for Sensitivity Analysis. *The Journal of Open Source Software*, **2 (9)**, 97, https://doi.org/10.21105/joss.00097.

Hoose, C., and O. Möhler, 2012: Heterogeneous ice nucleation on atmospheric aerosols: a review of results from laboratory experiments. *Atmospheric Chemistry and Physics*, **12 (20)**, 9817–9854, https://doi.org/10.5194/acp-12-9817-2012.

Iwanaga, T., W. Usher, and J. Herman, 2022: Toward SALib 2.0: Advancing the accessibility and interpretability of global sensitivity analyses. *Socio-Environmental Systems Modelling*, **4**, 18 155–18 155, https://doi.org/10.18174/sesmo.18155.

Johnson, J. S., Z. Cui, L. A. Lee, J. P. Gosling, A. M. Blyth, and K. S. Carslaw, 2015: Evaluating uncertainty in convective cloud microphysics using statistical emulation. *Journal of Advances in Modeling Earth Systems*, **7 (1)**, 162–187, https://doi.org/10.1002/2014MS000383.

Joos, H., 2019: Warm Conveyor Belts and Their Role for Cloud Radiative Forcing in the Extratropical Storm Tracks. *Journal of Climate*, **32 (16)**, 5325–5343, https://doi.org/10.1175/JCLI-D-18-0802.1.

Joos, H., E. Madonna, K. Witlox, S. Ferrachat, H. Wernli, and U. Lohmann, 2017: Effect of anthropogenic aerosol emissions on precipitation in warm conveyor belts in the western North Pacific in winter – a model study with ECHAM6-HAM. *Atmospheric Chemistry and Physics*, **17 (10)**, 6243–6255, https://doi.org/10.5194/acp-17-6243-2017.

Joos, H., and H. Wernli, 2012: Influence of microphysical processes on the potential vorticity development in a warm conveyor belt: a case-study with the limited-area model COSMO. *Quarterly Journal of the Royal Meteorological Society*, **138 (663)**, 407–418, https://doi.org/10.1002/qj.934.

Khain, A. P., and Coauthors, 2015: Representation of microphysical processes in cloud-resolving models: Spectral (bin) microphysics versus bulk parameterization. *Reviews of Geophysics*, **53 (2)**, 247–322, https://doi.org/10.1002/2014RG000468.

Korolev, A., and T. Leisner, 2020: Review of experimental studies of secondary ice production. *Atmospheric Chemistry and Physics*, **20 (20)**, 11 767–11 797, https://doi.org/10.5194/acp-20-11767-2020.

Lamb, D., and J. Verlinde, 2011: *Physics and Chemistry of Clouds*. Cambridge University Press, google-Books-ID: H97QKhe16aUC.

Lee, J., P. Seifert, T. Hashino, M. Maahn, F. Senf, and O. Knoth, 2024: Simulations of the impact of cloud condensation nuclei and ice-nucleating particles perturbations on the microphysics and radar reflectivity factor of stratiform mixed-phase clouds. *Atmospheric Chemistry and Physics*, **24 (10)**, 5737–5756, https://doi.org/10.5194/acp-24-5737-2024.

Li, Z., H. Xue, and F. Yang, 2013: A modeling study of ice formation affected by aerosols. *Journal of Geophysical Research: Atmospheres*, **118 (19)**, 11,213–11,227, https://doi.org/10.1002/jgrd.50861.

Madonna, E., H. Wernli, H. Joos, and O. Martius, 2014: Warm Conveyor Belts in the ERA-Interim Dataset (1979–2010). Part I: Climatology and Potential Vorticity Evolution. *Journal of Climate*, **27 (1)**, 3–26, https://doi.org/10.1175/JCLI-D-12-00720.1.

Marinescu, P. J., and Coauthors, 2021: Impacts of Varying Concentrations of Cloud Condensation Nuclei on Deep Convective Cloud Updrafts—A Multimodel Assessment. *Journal of the Atmospheric Sciences*, **78 (4)**, 1147–1172, https://doi.org/10.1175/JAS-D-20-0200.1.

Mazoyer, M., D. Ricard, G. Rivière, J. Delanoë, S. Riette, C. Augros, M. Borderies, and B. Vié, 2023: Impact of Mixed-Phase Cloud Parameterization on Warm Conveyor Belts and Upper-Tropospheric Dynamics. *Monthly Weather Review*, **151 (5)**, 1073–1091, https://doi.org/10.1175/MWR-D-22-0045.1.

Mazoyer, M., and Coauthors, 2021: Microphysics Impacts on the Warm Conveyor Belt and Ridge Building of the NAWDEX IOP6 Cyclone. *Monthly Weather Review*, **149 (12)**, 3961–3980, https://doi.org/10.1175/MWR-D-21-0061.1.

McCoy, D. T., and Coauthors, 2018: Aerosol midlatitude cyclone indirect effects in observations and high-resolution simulations. *Atmospheric Chemistry and Physics*, **18 (8)**, 5821–5846, https://doi.org/10.5194/acp-18-5821-2018.

Morris, M. D., and T. J. Mitchell, 1995: Exploratory designs for computational experiments. *Journal of Statistical Planning and Inference*, **43 (3)**, 381–402, https://doi.org/10.1016/0378-3758(94)00035-T.

Morrison, H., and Coauthors, 2020: Confronting the Challenge of Modeling Cloud and Precipitation Microphysics. *Journal of Advances in Modeling Earth Systems*, **12 (8)**, e2019MS001 689, https://doi.org/10.1029/2019MS001689.

Oakley, J. E., and A. O'Hagan, 2004: Probabilistic Sensitivity Analysis of Complex Models: A Bayesian Approach. *Journal of the Royal Statistical Society Series B: Statistical Methodology*, **66 (3)**, 751–769, https://doi.org/10.1111/j.1467-9868.2004.05304.x.

Oertel, A., M. Boettcher, H. Joos, M. Sprenger, and H. Wernli, 2020: Potential vorticity structure of embedded convection in a warm conveyor belt and its relevance for large-scale dynamics. *Weather and Climate Dynamics*, **1 (1)**, 127–153, https://doi.org/10.5194/wcd-1-127-2020.

Oertel, A., A. Miltenberger, C. Grams, and C. Hoose, 2025a: Research data for "Sensitivities of warm conveyor belt ascent, associated precipitation characteristics and large-scale flow pattern - insights from a perturbed parameter ensemble". URL https://radar.kit.edu/radar/en/dataset/ecgs4f56mp3ymjmt, https://doi.org/10.35097/ECGS4F56MP3YMJMT.

Oertel, A., A. K. Miltenberger, C. M. Grams, and C. Hoose, 2023: Interaction of microphysics and dynamics in a warm conveyor belt simulated with the ICOsahedral Nonhydrostatic (ICON) model. *Atmospheric Chemistry and Physics*, **23 (15)**, 8553–8581, https://doi.org/10.5194/acp-23-8553-2023.

Oertel, A., A. K. Miltenberger, C. M. Grams, and C. Hoose, 2025b: Sensitivities of warm conveyor belt ascent, associated precipitation characteristics and large-scale flow pattern: Insights from a perturbed parameter ensemble. *Quarterly Journal of the Royal Meteorological Society*, e4986, https://doi.org/10.1002/qj.4986.

Oertel, A., M. Sprenger, H. Joos, M. Boettcher, H. Konow, M. Hagen, and H. Wernli, 2021: Observations and simulation of intense convection embedded in a warm conveyor belt – how ambient vertical wind shear determines the dynamical impact. *Weather and Climate Dynamics*, **2 (1)**, 89–110, https://doi.org/10.5194/wcd-2-89-2021.

Panicker, A. S., V. Anil Kumar, M. P. Raju, G. Pandithurai, P. D. Safai, G. Beig, and S. Das, 2021: CCN activation of carbonaceous aerosols from different combustion emissions sources: A laboratory study. *Atmospheric Research*, **248**, 105 252, https://doi.org/10.1016/j.atmosres.2020.105252.

Paramonov, M., R. O. David, R. Kretzschmar, and Z. A. Kanji, 2018: A laboratory investigation of the ice nucleation efficiency of three types of mineral and soil dust. *Atmospheric Chemistry and Physics*, **18 (22)**, 16 515–16 536, https://doi.org/10.5194/acp-18-16515-2018.

Pedregosa, F., and Coauthors, 2011: Scikit-learn: Machine Learning in Python. *Journal of Machine Learning Research*, **12 (85)**, 2825–2830, URL http://jmlr.org/papers/v12/pedregosa11a.html.

Pfahl, S., E. Madonna, M. Boettcher, H. Joos, and H. Wernli, 2014: Warm Conveyor Belts in the ERA-Interim Dataset (1979–2010). Part II: Moisture Origin and Relevance for Precipitation. *Journal of Climate*, **27 (1)**, 27–40, https://doi.org/10.1175/JCLI-D-13-00223.1.

Rasmussen, C. E., 2004: Gaussian Processes in Machine Learning. Springer, Berlin, Heidelberg, 63–71, https://doi.org/10.1007/978-3-540-28650-9_4.

Saltelli, A., S. Tarantola, and K. P.-S. Chan, 1999: A Quantitative Model-Independent Method for Global Sensitivity Analysis of Model Output. *Technometrics*, **41 (1)**, 39–56, https://doi.org/10.1080/00401706.1999.10485594.

Schneider, L., C. Barthlott, C. Hoose, and A. I. Barrett, 2019: Relative impact of aerosol, soil moisture, and orography perturbations on deep convection. *Atmospheric Chemistry and Physics*, **19 (19)**, 12 343–12 359, https://doi.org/10.5194/acp-19-12343-2019.

Schröter, J., and Coauthors, 2018: ICON-ART 2.1: a flexible tracer framework and its application for composition studies in numerical weather forecasting and climate simulations. *Geoscientific Model Development*, **11 (10)**, 4043–4068, https://doi.org/10.5194/gmd-11-4043-2018.

Schäfler, A., and F. Harnisch, 2015: Impact of the inflow moisture on the evolution of a warm conveyor belt. *Quarterly Journal of the Royal Meteorological Society*, **141 (686)**, 299–310, https://doi.org/10.1002/qj.2360.

Schäfler, A., and Coauthors, 2018: The North Atlantic Waveguide and Downstream Impact Experiment. *Bulletin of the American Meteorological Society*, **99 (8)**, 1607–1637, https://doi.org/10.1175/BAMS-D-17-0003.1.

Seifert, A., and K. D. Beheng, 2006: A two-moment cloud microphysics parameterization for mixed-phase clouds. Part 1: Model description. *Meteorology and Atmospheric Physics*, **92 (1)**, 45–66, https://doi.org/10.1007/s00703-005-0112-4.

Stohl, A., 2001: A 1-year Lagrangian "climatology" of airstreams in the northern hemisphere troposphere and lowermost stratosphere. *Journal of Geophysical Research: Atmospheres*, **106 (D7)**, 7263–7279, https://doi.org/10.1029/2000JD900570.

Straka, J. M., 2009: *Cloud and Precipitation Microphysics: Principles and Parameterizations*. Cambridge University Press, google-Books-ID: VFuJQd9pbQ0C.

Tao, W.-K., J.-P. Chen, Z. Li, C. Wang, and C. Zhang, 2012: Impact of aerosols on convective clouds and precipitation. *Reviews of Geophysics*, **50 (2)**, https://doi.org/10.1029/2011RG000369.

Vali, G., P. J. DeMott, O. Möhler, and T. F. Whale, 2015: Technical Note: A proposal for ice nucleation terminology. *Atmospheric Chemistry and Physics*, **15 (18)**, 10 263–10 270, https://doi.org/10.5194/acp-15-10263-2015.

Warner, T. T., 2010: *Numerical Weather and Climate Prediction*. Cambridge University Press, Cambridge, UNITED KINGDOM, URL http://ebookcentral.proquest.com/lib/karlsruhetech/detail.action?docID=605113.

Wellmann, C., A. I. Barrett, J. S. Johnson, M. Kunz, B. Vogel, K. S. Carslaw, and C. Hoose, 2018: Using Emulators to Understand the Sensitivity of Deep Convective Clouds and Hail to Environmental Conditions. *Journal of Advances in Modeling Earth Systems*, **10 (12)**, 3103–3122, https://doi.org/10.1029/2018MS001465.

Wellmann, C., A. I. Barrett, J. S. Johnson, M. Kunz, B. Vogel, K. S. Carslaw, and C. Hoose, 2020: Comparing the impact of environmental conditions and microphysics on the forecast uncertainty of deep convective clouds and hail. *Atmospheric Chemistry and Physics*, **20 (4)**, 2201–2219, https://doi.org/10.5194/acp-20-2201-2020.

Wernli, H., and H. C. Davies, 1997: A Lagrangian-based analysis of extratropical cyclones. I: The method and some applications. *Quarterly Journal of the Royal Meteorological Society*, **123 (538)**, 467–489, https://doi.org/10.1002/qj.49712353811.

Westbrook, C. D., and A. J. Heymsfield, 2011: Ice Crystals Growing from Vapor in Supercooled Clouds between 2.5° and 22°C: Testing Current Parameterization Methods Using Laboratory Data. *Journal of the Atmospheric Sciences*, **68 (10)**, 2416–2429, https://doi.org/10.1175/JAS-D-11-017.1.

Zängl, G., D. Reinert, P. Rípodas, and M. Baldauf, 2015: The ICON (ICOsahedral Non-hydrostatic) modelling framework of DWD and MPI-M: Description of the non-hydrostatic dynamical core. *Quarterly Journal of the Royal Meteorological Society*, **141 (687)**, 563–579, https://doi.org/10.1002/qj.2378.

Acknowledgments

I would like to sincerely thank Annika Oertel for the outstanding supervision. Her guidance, quick responses, and constant availability for any questions I had made working on my thesis so much smoother.

I also wish to thank Miriam Simm for her technical and emotional support. Thanks for always being willing to help whenever needed.

I am grateful to Corinna Hoose for giving me the opportunity to write my thesis within her research group, for the valuable feedback, and for the warm welcome to meteorology when I decided to leave my physics studies behind.

To my parents: thank you for your unwavering financial support and, more importantly, for always encouraging me to choose my own path and believe in myself.

Special thanks to Opa Meinrad for supplying me and the whole office with Christmas cookies.

To my beloved Chrissibär: Your emotional support has been invaluable. Thank you for listening with great care to all my concerns, problems, ideas, and successes. Thanks for taking such good care of me in the last days before the thesis deadline. Knowing you are always there for me makes all the difference. I love you <3

A special thanks to Vicky for being the best study buddy and friend. Thank you, Vicky, for your constant encouragement and support throughout our studies. You got me carried away by a moonlight shadow and made me feel like a storm warrior of the partly cloudy. It was like a duck. Wish you the best for your Ph.D.!

Lastly, I would like to thank my fellow students and student fellows from the office for the supportive environment, the many helpful discussions, and the enjoyable times shared during lunch breaks. Special thanks go to Jasmin and Alec for crafting snowflakes with me. Thank you, Alec, for your constant support, cheerfulness, and humor. Can't wait for Jong et al. to become a thing! I also want to thank Nicole for our weekly lunch dates. Thank you so much for listening to my concerns and taking me to the Karrieremesse. Without you, I wouldn't have gotten a duck. Last but not least, I want to thank Lina for always making my day brighter with her positive energy. Thanks for making me laugh and feel better.

Erklärung

Ich versichere wahrheitsgemäß, die Arbeit selbstständig verfasst, alle benutzten Hilfsmittel vollständig und genau angegeben und alles kenntlich gemacht zu haben, was aus Arbeiten anderer unverändert oder mit Abänderungen entnommen wurde sowie die Satzung des KIT zur Sicherung guter wissenschaftlicher Praxis in der jeweils gültigen Fassung beachtet zu haben.

Karlsruhe, den 28.05.2025

(Vanessa Schneider)